TECHNISCHE UNIVERSITÄT WIEN
Vienna University of Technology

DISSERTATION

Phase transformation kinetics during continuous heating of α+β and metastable β titanium alloys

* * * * *

ausgeführt zum Zwecke der Erlangung des akademischen Grades eines
Doktors der technischen Wissenschaften unter der Leitung von

Univ. Prof. Dr. techn. Guillermo Carlos Requena

eingereicht an der Technischen Universität Wien
Fakultät Maschinenwesen und Betriebswissenschaften

von

Pere Barriobero Vila

Matr. Nr.: 0929167

Reindorfgasse 29
1150 Wien

Wien, am 24. Juli 2015

Pere Barriobero Vila

A l'Assumpta i en Pere,

que també han pujat el camí rost dels últims anys

Si el sofregit queda integrat i es converteix en un licor –o sigui en una confitura–, l'arròs es torna monumental, sigui el que sigui el que es posi a la cassola; és igual.

Josep Pla

Acknowledgements

Fortunately, the work compiled in this document received a wide variety of supports during the tortuous trajectory of the last four years. They all definitely deserve my acknowledgement:

- To Univ. Prof. Dr. techn. Guillermo Carlos Requena for a precious guidance. The big fascination and experience on his job strongly contributed to push this thesis forward throughout these valuable years. Also, this document is based in his persistent generosity, comprehension and trust, from where very challenging opportunities and scientific insight came out. For all, I want to express him my gratitude: Gracias Guille.
- I am deeply acknowledged to Prof. Damien Fabregue who acceded to take part in the defence as second examiner and took his valuable time to establish a detailed review with very interesting comments. Merci.
- It is a pleasure to count on Prof. Paul Mayrhofer representing the defence Chair. My sincere gratitude for his receptivity and time.
- My first steps in the institute are certainly influenced by the positive atmosphere associated with the presence of Em. O. Univ. Prof. Dipl.-Ing. Dr. techn. Hans-Peter Degischer in our group. Due to his continuous and amenable human support I feel indebted to him. Ein herzliches Dankeschön.
- Dr. F. Warchomicka and Prof. C. Poletti are acknowledged for shearing expertise.
- Since I landed in Vienna my stay in the institute elapsed as a member of a huge team of unique personalities. From them, I learned many points of view and plentiful friendship connections were established. With special emphasis to: M. Rodriguez, M. Dikovits, C. Poletti, C. Collet, P. Homporová, A. Zisser, A. Flourez, K. Bugelnig, J. Zhou, L. Fernandes, V. Biancardi, E. Asiemo, J. Jonke, J. David, G. Fiedler, G. Requena, D. Tolnai, R. Fernández, S. Großeiber, J. Crespo, F. Warchomicka, D. Canelo, C. Zaruba, P. Wiehoff, R. Koos, M. Schöbel, C. Montalba, M. Kumar, R. Hahn, E. Zehetner, A. Bekir, G. Stechauner, A. Gámez, D. Lorrain, L. Jacquemet, K. Dupont, Ali, E. Pereira, H. Pinto.
  Thanks for your personal input in the everyday life.
- I wish to thank the Institute of Materials Science and Technology (IMST) of the Vienna University of Technology (TU Wien) for providing its research facilities and warm hospitality.

- The University Service Centre for Transmission Electron Microscopy (USTEM) of the TU Wien is acknowledged for the provision of FEG-SEM and TEM microscopes.
- My honest gratitude to C. Zaruba, E. Asiemo, H. Kaminski, S. Zellhofer, T. Wojcik from IMST, and K. Whitemore and S. Schwarz from USTEM for their tremendous technical assistance in the TU Wien.
- Sincere thanks goes to S. Windisch, T. Grünwald and D. Fischer who with their distinctive adorable mood produced a very effective work in my institute' dossier.
- This work was carried out in the framework of the K-Project "Non-Destructive Testing and Tomography" COMET-Program Grant No. 820492 with partnership of Böhler Schmiedetechnik GmbH & Co KG. I am intensely beholden to them for financial support.
- My cordial acknowledgement to Dr. M. Stockinger and Dr. B. Oberwinkler from Böhler Schmiedetechnik for helpful discussions during project meetings.
- I would like to thank Prof. D. Raabe and Dr. S. Sandlöbes from Max-Planck-Institute für Eisenforschung GmbH for their collaboration with the investigations.
- The European Synchrotron Radiation Facility (ESRF) and the Deutsches Elektronen-Synchrotron (DESY) are acknowledged for the provision of synchrotron radiation facilities. Moreover, I would like to thank U. Bösenberg, T. Buslaps, M. Alfeld, G. Falkenberg, N. Schell and A. Stark for their professional assistance during beam time.
- To my beloved Nora. The driving force for this work is inseparable from her genuine character, and therefore, from the privilege to intimately learn from her persistent dynamic, charismatic and forceful support in any context.

  Danke Du: Moltes gràcies!
- At last, I would like to colourfully highlight the always-sporty support and warmth of my family from Catalonia:

  El sempre persistent i càlid magnetisme de la nostra arborada família ha contribuït a que aquest monogràfic passés d'un mer holograma a consumar-se en una plàcida realitat. Naturalment, sento un profund agraïment i admiració per tu Mare, Pare, Jordi, iaia Coloma i avi Pere, que sou tant propers i immediats. A més, dono gràcies per la magnanimitat de molts altres al·ludits familiars, que com el tiet Jaume, representen per a mi una clara referència humana.

Abstract

The progress of environmental as well as performance targets that must be guaranteed by the transportation sector is highly conditioned to the availability of materials that can offer structural weight savings and improve engine performance. Titanium alloys are key materials in this regard owing to their superior specific strength with respect to other structural alloys and excellent corrosion resistance up to ~ 500 °C. However, these alloys are still associated with high production costs, and therefore, advances in manufacturing optimization are necessary to further extent their implementation. Since the mechanical properties of titanium alloys are consequence of microstructural-based alloy design controlled by the phase transformation kinetics during heat treating, a correct understanding of these processes is required.

This dissertation focuses in the continuous and univocal study of the phase transformation kinetics during linear heating of α+β and metastable β titanium alloys from room temperature to the β field. An initial bi-modal microstructure is used to analyse the evolution of stable phases, namely α and β for the first group of alloys. On the other hand, decomposition of the β-quenched condition leading to formation of metastable products such as α″, ω and β′+β is studied for the second group of alloys. The investigations are carried out combining laboratory characterization methods with advanced synchrotron-based techniques including in situ high energy X-ray diffraction and micro X-ray fluorescence. Variations in the phase transformation sequences are presented as a function of heating rate. Furthermore, the continuous evolution of the crystal structure of phases is analysed in terms of the physical mechanisms involved during phase transformation.

Kurzfassung

Das Erreichen ökologischer und leistungsoptimierter Ziele im Transportsektor ist zum größten Teil abhängig von der Verfügbarkeit von Materialien, die für strukturelle Gewichtsersparnisse und verbesserte Motorenleistungen genutzt werden können. Titanlegierungen sind in dieser Hinsicht Schlüsselmaterialien aufgrund hoher spezifischer Festigkeiten im Vergleich zu anderen strukturellen Legierungen und ihrer hervorragenden Korrosionsresistenz bis zu ~ 500 °C. Diese Legierungen werden allerdings immer noch mit hohen Produktions- und Verarbeitungskosten assoziiert. Daher sind weitere Optimierung der Herstellungsverfahren notwendig, um das Einsatzgebiet dieser Legierungen ausweiten zu können. Die mechanischen Eigenschaften von Titanlegierungen werden von mikrostrukturellem Legierungsaufbau, welcher von der Kinetik der Phasenumwandlungen während angewandter Wärmebehandlungen abhängig ist, bestimmt. Dadurch ist das restlose Verständnis der zugrundliegenden Prozesse notwendig, um den optimierten und effizienten Einsatz dieser Schlüsselmaterialien zu gewährleisten.

Die vorliegende Dissertation beschäftigt sich mit der kontinuierlichen Analyse und der eindeutigen Bestimmung der Kinetik der Phasenumwandlung während linearer Aufheizung von $\alpha+\beta$ und metastabilen β Titanlegierungen, die von Raumtemperatur bis zum β Bereich aufgeheizt wurden. Für die erste Legierungsgruppe wird von einer bi-modalen Mikrostruktur ausgegangen, um die Entwicklung der stabilen Phasen α und β zu analysieren. In der zweiten Legierungsgruppe wird die Zersetzung eines β abgeschreckten Zustandes untersucht, welche zur Bildung von metastabilen Produkten wie α'', ω und $\beta'+\beta$ führt. Die Untersuchungen werden mit der Kombination von Labor- und fortgeschrittenen Synchrotrontechniken, wie der hochenergetischen in situ Röntenbeugung und Mikro-Röntgenfluoreszenz, durchgeführt. Variationen in der Sequenz von Phasenumwandlungen werden als eine Funktion der Aufheizrate dargestellt. Darüber hinaus wird die kontinuierliche Entwicklung der Kristallstruktur der Phasen während Umwandlungsprozessen im Hinblick auf die physikalischen Mechanismen analysiert.

Content

1. Motivation

The transportation sector moves towards more strict efficiency requisites to comply with performance and environmental targets such as the reduction of noise as well as CO_2 and NO_x emissions [1–3]. The viability and progress of these strategies is highly conditioned to the availability of engineering materials that can offer structural weight savings and improve engine performance.

Titanium alloys exhibit superior specific strength (yield strength / density) than other structural alloys within a broad range of service temperatures and present excellent corrosion resistance up to about 500 °C (see Fig. 1.1) [4–8]. These properties represent many performance advantages for the transportation sector as evidenced in the use of components made of α+β and metastable β titanium alloys for the aerospace and automotive industries [3,9–12].

Despite these benefits and the relatively large reserves of titanium (fourth most abundant metal in the earth's crust), titanium alloys still present high production costs which limits their extensive implementation in the industry.

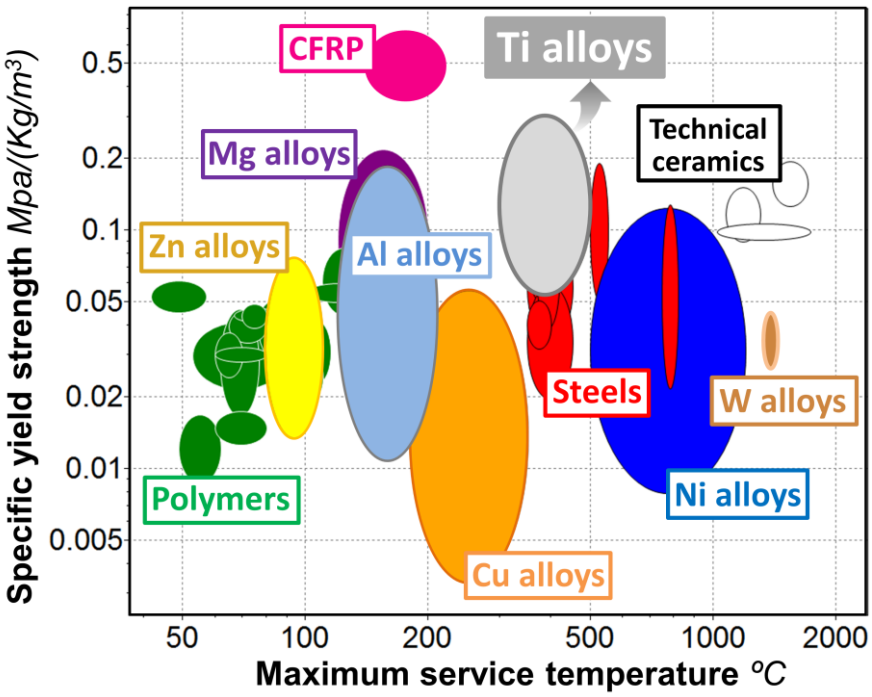

Fig. 1.1. Variation of specific yield strength as a function of the maximum service temperature for the main families of engineering materials [8].

1. Motivation

The initiatives to minimize the cost of titanium-based components have been addressed at most of the production stages. However, the process of ingot metallurgy (cast and wrought) presents special interest because provides alloys with high strength levels and offers large margins for expense reduction [13–15]. At this stage of manufacturing, thermal and thermo-mechanical treatments determine the microstructural characteristics, i.e. the mechanical properties of titanium alloys taking advantage of their phase transformation kinetics [4–7].

Modelling tools for microstructure prediction in titanium alloys lead to improvements in functional alloy design, lead-time and cost savings [16–19]. Although some advances have been achieved (e.g. [20,21]), these models are still mostly confined to thermodynamic analyses (phase equilibria) where the role of kinetic variables (e.g. heating rate) is not considered.

Similarly, the study of phase transformations of α+β and especially metastable β titanium alloys has been mostly discussed in the basis of isothermal aging and ex-situ experiments (e.g. [22–26]). This fact constrains the advance of modelling tools since they require reliable experimental data for validation. Thus, a correct understanding of the phase transformation kinetics is required for the development of theoretical models as well as optimization of functional alloy design, intending to minimize the expenses during processing of titanium alloys.

In this dissertation, the phase transformation kinetics of α+β and metastable β titanium alloys are continuously and univocally evaluated as a function of heating rate during linear heat treatment throughout the entire processing window, i.e. from room temperature (RT) to the β field. The investigations are focused on critical aspects of thermal processing such as the role of metastable phases and element partitioning during phase transformation. The diagram of Fig. 1.2 provides a concise summary of the motivation described in the previous lines.

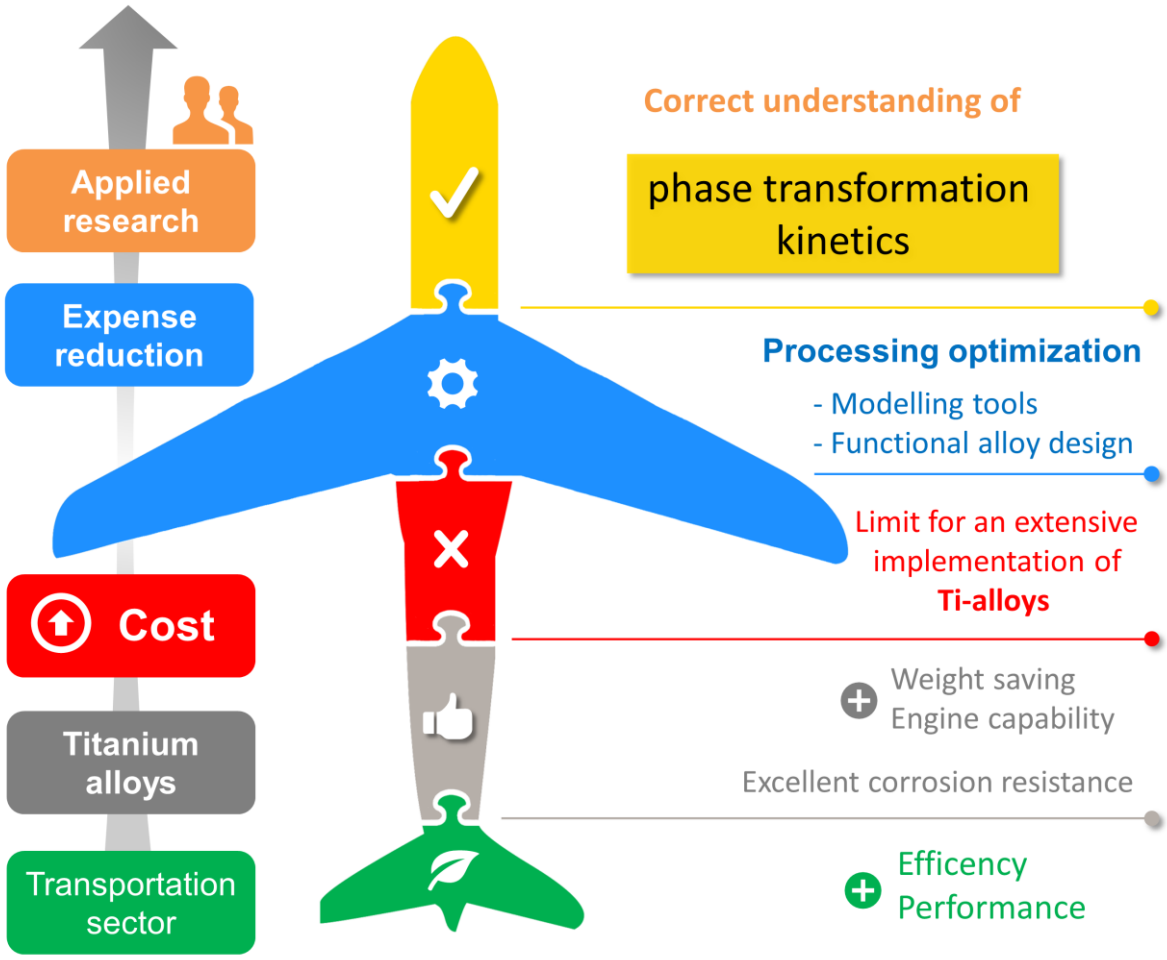

Fig. 1.2. Flow diagram reproducing the motivation of the present work.

2. Titanium alloys

Titanium presents basically two allotropic modifications like most of its alloys: the slightly distorted hexagonal close packed (hcp) structure α phase (α titanium) crystallizes at low temperatures, while at temperatures over the β-transus (882 ± 2 ºC for pure Ti), T_β, α transforms completely into the high temperature body-centred cubic (bcc) β phase (β titanium) (see Fig. 2.1 a). During this process, the most densely packed planes {110} of β become the basal planes {0001} of α, resulting in 12 possible orientations (transformation variants) between both phases. This lattice correspondence is represented in Fig. 2.1 b). Although the unit cell of α presents a smaller *c*/*a* ratio (1.587) than ideal hcp structures (1.633), this value can slightly increase with the insertion of interstitial (e.g. C, N, O) and substitutional (e.g. Al) atoms of smaller atomic radius than titanium [4–7].

α and β phases are present simultaneously in most of the titanium alloys since their combination can provide a wide variety of properties. The microstructures are controlled by thermal and thermomechanical treatments where also crystallographic textures may develop during deformation. This is especially relevant for the hcp α phase due to its anisotropic mechanical behaviour [4,5].

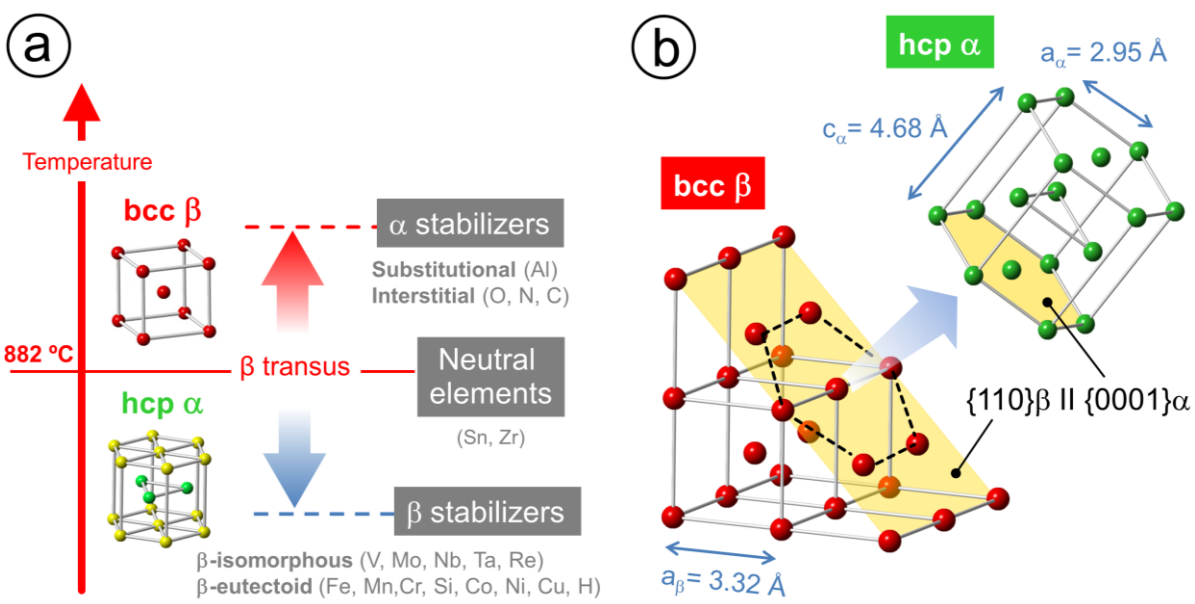

Fig. 2.1. a) Classification of the alloying elements of titanium according to their influence on the β-transus temperature, T_β. **b)** Lattice correspondence between the hcp α and bcc β structures. The lattice parameters correspond to the values of pure titanium at RT and 900 ºC for α and β, respectively.

2.1. Alloying elements

The alloying elements of titanium are classified according to their effect in the solubility of α and β phases as α-stabilizers, β-stabilizers and neutral elements (see Fig. 2.1 a) [4,5]:

α stabilizers: Extend the β phase field to higher temperatures, i.e. increase T_β. Al, which has a substitutional role, is the most used alloying element in titanium alloys due to its large solubility in α and β phases and its capacity as regular metal to increase T_β. O, N and C are the most usual interstitial elements of this group. Non-common elements are B, Ga, Ge and rare earth elements because of their low solubility.

β stabilizers: Shift the β phase field to lower temperatures, i.e. decrease T_β. They are divided into β-isomorphous and β-eutectoid elements. The β-isomorphous, namely V, Mo, Nb, Ta and Re (the last two are rarely used due to their high density) are the most important because of their higher solubility in Ti. The β-eutectoids (Fe, Mn, Cr, Co, Ni, Cu, Si and H) can lead to the formation of intermetallic compounds. Furthermore, H is normally restricted to ~ 125 – 150 ppm to avoid embrittlement.

Neutral elements: Have minor influence on T_β, i.e. on the α / β phase boundary. However, they increase the strength of α. Sn and Zr are the most common.

The effect of alloying elements in the overall stability of α and β phases can be evaluated in terms of equivalent Al ($[Al]_{eq}$) and Mo ($[Mo]_{eq}$) contents, respectively. The individual contribution of elements for each rule is reflected in the following equations:

$$[Al]_{eq.} = [Al] + 0.33\,[Sn] + 0.17\,[Zr] + 10\,[O + C + 2N] \quad (1)$$

$$[Mo]_{eq.} = [Mo] + 0.2\,[Ta] + 0.28\,[Nb] + 0.4\,[W] + 0.67\,[V] + 1.25\,[Cr] + 1.25\,[Ni] + 1.7\,[Mn] + 1.7\,[Co] + 2.5\,[Fe] \quad (2)$$

The $[Al]_{eq}$ content is usually limited to 9 wt.% (or to 6 wt.% of [Al]) in order to avoid embrittlement by precipitation of Ti_3Al. On the other hand, a $[Mo]_{eq}$ content of at least ~ 10 wt.% is required to stabilize β upon quenching of titanium alloys [4,5].

2.2. Alloy Classification

Titanium alloys are classified according to their position in the β isomorphous phase diagram as α, near α, α+β, metastable β and stable β alloys (see Fig. 2.2) [4,5]:

α alloys: Comprise four grades of commercially pure titanium (Ti-O alloys where O varies between 0.18 – 0.40 wt.% from grade 1 to 4) and alloys with exclusively α stabilizing and / or neutral elements. Due to their lack of heat treatment response, strengthening by solid solution and cold working are usually applied. Furthermore, they are especially suitable for the chemical industry (e.g. in pressure vessels or heat exchangers) owing to their excellent corrosion and creep resistance.

Near α alloys: Present minor fractions of β stabilizers (up to 2 wt.%) forming less than ~ 10 vol.% of β phase. These alloys combine high creep resistance with good strength levels and are mainly used for high temperature applications (~ 500 – 550 ºC) in the aerospace industry (e.g. compressors of turbine engines).

α+β alloys: Comprise additions of β stabilizers of 4 – 6 wt.% leading to 5 – 40 vol.% fractions of β phase at RT. Martensite transformation occurs upon fast cooling from the β phase field to RT (see martensite start line, M_s, in Fig. 2.2). These alloys can develop a wide variety of microstructures, i.e. different mechanical properties, by applying different thermal and thermomechanical treatments. This explains their broad range of applications (see section 2.7). Within this group, the Ti-6Al-4V alloy is one of the first made titanium alloys and the most commercialized nowadays (absorbs more than 50 % of the global market). This is because Ti-6Al-4V represents the most developed and tested titanium alloy that, at the same time, offers a well-balanced property profile.

Metastable β alloys: Due to their high content in β stabilizers (10 – 15 wt.%) these alloys do not transform martensitically (avoid M_s) upon fast cooling. Instead, β is retained in metastable condition (see Fig. 2.2). Amounts > 50 vol.% of α can be reached in equilibrium. The relevance of these alloys is increasing owing to their attractive properties: high strength levels of hardening (> 1400 MPa) combined with acceptable toughness, fatigue resistance and good formability (β presents more slip systems than α, i.e. 12 versus 3, respectively). They are divided into high strength and heavily stabilized alloys, with high and lower contents of α, respectively (Fig. 2.2). Similarly to α+β alloys, the

microstructure of metastable β alloys is highly susceptible to thermal and thermomechanical treatments.

Stable β alloys: Present very high additions of β stabilizers (about 30 wt.%) and are formed by single β phase. Commercial alloys are excluded from this group.

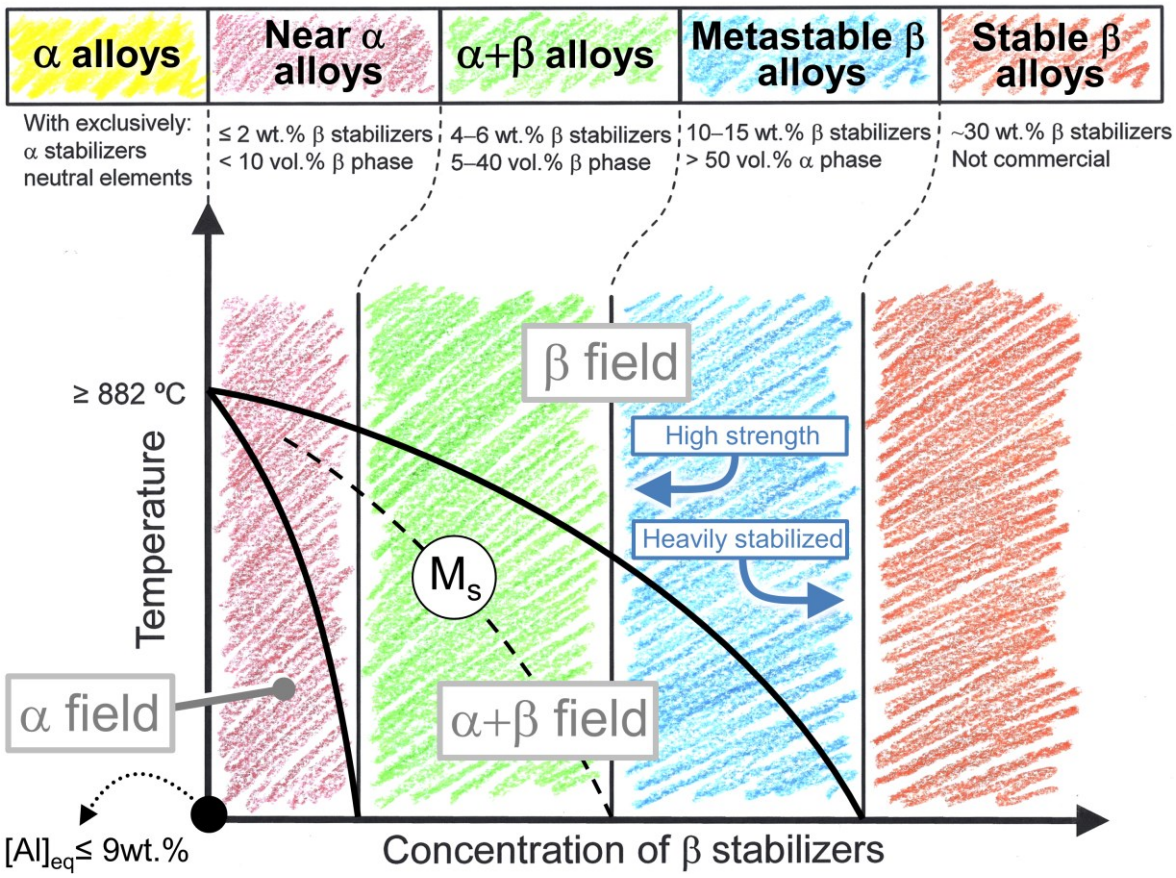

Fig. 2.2. Classification of titanium alloys in the β isomorphous phase diagram (pseudo-binary section).

2.3. Alloy design

The properties of titanium alloys are basically determined by their chemical composition and microstructure. The first factor regulates the volume fraction of phases and therefore, the balance of their individual properties, while the second defines the arrangement of phases (usually α and β) in the alloy. According to this, there exist two ways to improve the properties of titanium alloys: alloying and processing. On the one hand, alloying essentially determines the chemical and physical properties as well as the basis to increase the strength. On the other hand, processing establishes the balance of mechanical properties through microstructure control achieved by thermal and thermomechanical

treatments (see section 2.4) [4,5]. These aspects are summarized in Fig. 2.3 with relevant property variations for the different groups of titanium alloys.

The role of strength has a central importance in the optimization of functional alloy design for α+β and metastable β alloys since they compete as with steel as materials for structural components (~ 800 – 1400 MPa) (see Fig. 2.3) [4,5]. In the present work, the α+β Ti-6Al-6V-2Sn and the metastable β Ti-10V-2Fe-3Al and Ti-5Al-5Mo-5V-3Cr-1Zr alloys have been studied. Hence, the next sections will give especial emphasis on these groups of alloys.

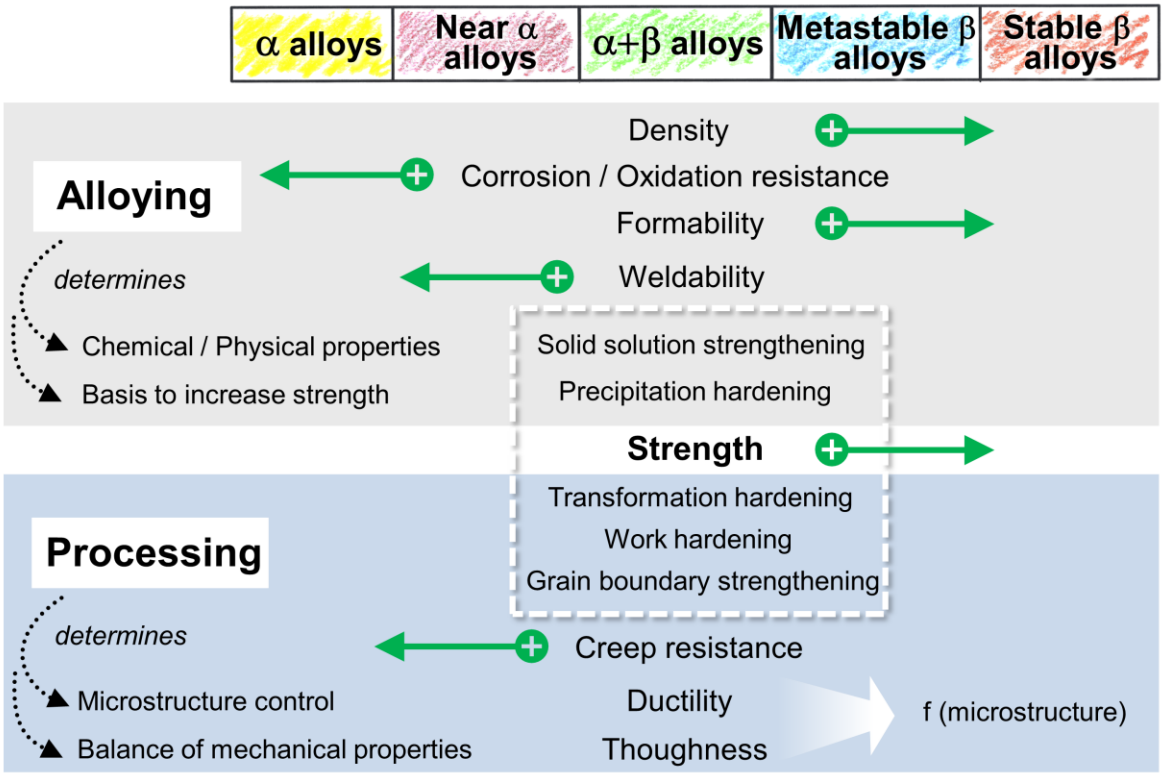

Fig. 2.3. Variations of physical, chemical, mechanical and technological properties for the different groups of titanium alloys and their association with alloying and processing methods.

2.4. Microstructure

The processing of titanium alloys comprises basically four thermal and thermomechanical treatments, namely homogenization, deformation, recrystallization and aging (Fig. 2.4), where variations in the processing parameters lead to the formation of very diverse microstructures [5,6]. The ones obtained for α+β and metastable β alloys are discussed in this section.

2.4.1. α+β alloys

Equiaxed and lamellar microstructures represent the most illustrative example of different phase arrangements in titanium alloys. The first one consists in primary α (α_p) grains embedded in a β matrix. It can be obtained after deformation through two different ways: upon slow cooling after homogenization from temperatures slightly below T_β, or via recrystallization of α at moderate temperatures (see Fig. 2.4). On the other hand, the lamellar microstructure is composed by packets of α lamellae that grow via β → α transformation within β grains during cooling from temperatures above T_β (see Fig. 2.4 and section 2.6.1). In this case, the deformation step can be carried out either in β or α+β field.

Bi-modal microstructures are a combination of equiaxed and lamellar grains: colonies of α lamellae distributed within β grains coexist with α primary grains located at the triple points of β grain boundaries. This microstructure is basically the result of a recrystallization process in α+β field, where the degree of deformation, the cooling rates during homogenization and recrystallization are important to control the size and width of α_p and α lamellae, respectively (see Fig. 2.4).

Precipitation of secondary α (α_s) plates in β grains is normally induced during the final aging treatment of α+β alloys due to its positive strengthening effect (Fig. 2.4) [4,5].

2.4.2. Metastable β alloys

Bi-modal microstructures can be obtained for metastable β alloys through a path analogous to that presented for α+β alloys (see section 2.4.1). In this case, the cooling rate from the β field (homogenization step) is a very critical parameter due to the eventual formation of grain boundary α (α_{GB}): continuous layers of α along β grain boundaries which are detrimental to the mechanical properties (see section 2.5.2).

β-annealed microstructures consist in homogeneous distributions of fine α_s plates within a matrix of β grains. They result from an annealing in the β field with subsequent quenching followed by an aging treatment (Fig. 2.4). Differently to the bi-modal microstructure, in this case the precipitation of α_{GB} can be suppressed by fast quenching, and the β matrix is

retained in metastable state instead. Additionally, the negative influence of α_{GB} can be minimized by thermomechanical processing in large cross sections.

Precipitation of fine α_s plates occurs during aging by the assistance of metastable particles associated with the ω phase as well as β′+β products resulting from the decomposition of the β matrix (see section 2.6.2). Slow heating rates are required to ensure a fine and homogeneous distribution of α_s since the growth of these metastable particles is driven by diffusion-driven processes. The processing of heavily stabilized alloys usually includes a double-step aging in order to improve homogeneity of α_s plates, and therefore, prevent premature fracture of non-hardened areas. The deformation of β-annealed microstructures can be performed either in β or α+β field [4,5].

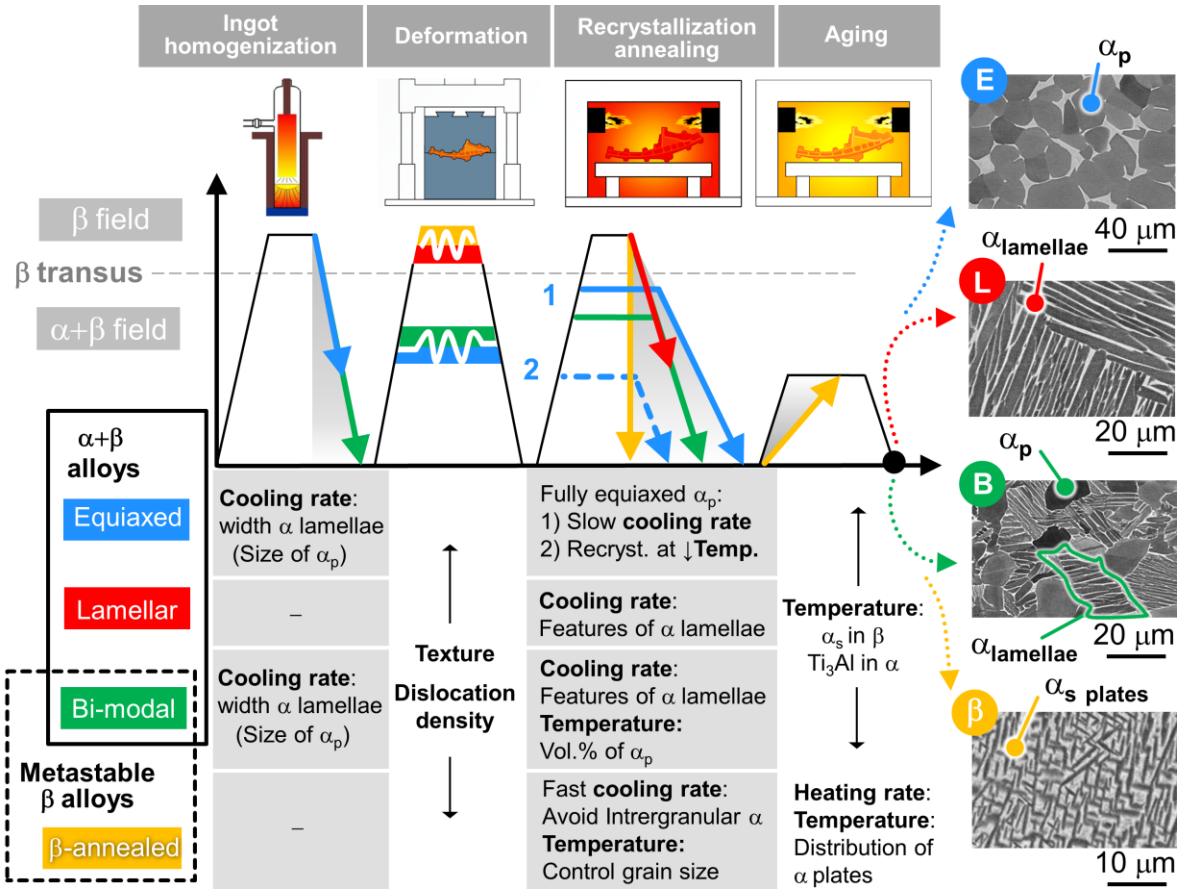

Fig. 2.4. Processing paths for conventional microstructures of α+β and metastable β titanium alloys, namely equiaxed, lamellar, bi-modal and β-annealed. The most relevant parameters for each step of the processing as well as characteristic resulting microstructures (SEM micrographs) are presented for each condition.

2.5. Mechanical properties

The mechanical properties of α+β and metastable β titanium alloys are linked to specific microstructural features such as α colony and β grain sizes, alloy element partitioning, or the presence of grain boundary α layers. The right configuration of these parameters should be established during processing according to the requirements for each application.

2.5.1. α+β alloys

The strength, toughness, ductility and fatigue resistance of α+β alloys are essentially determined by the effective slip length across the incoherent α / β interphase. For lamellar and bi-modal microstructures this effect can be reduced by decreasing the α colony size, i.e. by applying fast cooling rates during the recrystallization step (see Fig. 2.4). Consequently, a general improvement of the properties' profile (e.g. in the yield stress) can be achieved. On the other hand, equiaxed microstructures can reduce the slip length by decreasing the α grain size.

In contrast to lamellar microstructures, the bi-modal ones offer smaller β grain sizes which are restricted to the distance between α_p grains. Hence, smaller α colonies can be obtained by varying the volume fraction (vol.%) of α_p. This last factor determines also the alloy element partitioning presented by bi-modal microstructures: the lower enrichment in α stabilizers of α colonies with respect to α primary grains. Therefore, as the vol.% of α_p increases α lamellae become softer and the strength between lamellar regions decreases. This effect does not occur for fully lamellar microstructures.

Equiaxed microstructures are characterized by a high ductility (possible superplastic deformation) and resistance to fatigue crack nucleation. On the other hand, lamellar microstructures present high fracture toughness, creep strength and resistance to fatigue crack growth (macro-cracks) due to their rough crack propagation profile. An inverse property profile is expected for bi-modal microstructures due to the influence of finer α colonies. Also, lower resistance to fatigue crack nucleation and low cycle fatigue strength are obtained due to the negative effect of alloy element partitioning. This effect can be improved by regulation of the vol.% of α_p as well as by including a heat treatment between the recrystallization and aging steps to promote diffusion between α_p and lamellar regions

(see Fig. 2.4). Bi-modal microstructures combine the advantages of lamellar and equiaxed configurations and therefore, exhibit a well-balanced property profile. The aspects discussed in the previous lines are summarized in the property profiles presented in Fig. 2.5 a).

Crystallographic texture can introduce remarkable anisotropy in the mechanical properties of equiaxed and bi-modal microstructures due to the severe deformations reached during processing in α+β field (see Fig. 2.4). Thus, higher values of Young's modulus, yield strength and creep resistance can be reached along the transverse direction (direction parallel to the *c*-axis of the hcp α phase) than along the basal one (direction perpendicular to the *c*-axis of the hcp α phase) [4–6].

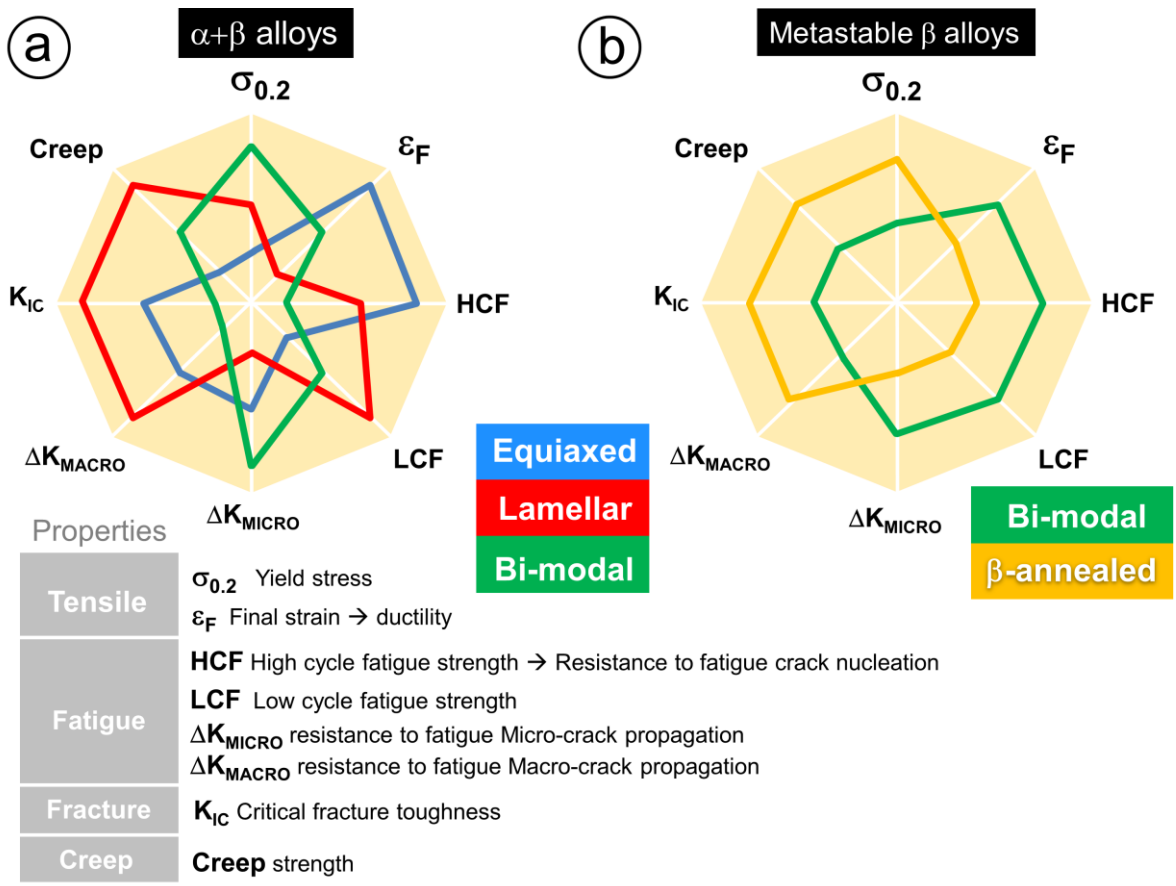

Fig. 2.5. Property profiles for microstructures of α+β and metastable β titanium alloys namely equiaxed, lamellar, bi-modal and β-annealed, based in the influence of the typical microstructural parameters on the mechanical properties (e.g. the α colony size, alloy element partitioning, β grain size and intergranular α layers).

2.5.2. Metastable β alloys

The homogeneous precipitation of fine α_s plates occurring during aging of metastable β alloys leads to increase in yield strength but also decreases their ductility: these particles slow down dislocations but do not deform plastically. Even more critical reduction of ductility occurs with the presence of continuous α_{GB} layers. They provoke strain concentrations leading to subsequent crack nucleation and intergranular fracture through β grain boundaries. This effect can be partially hindered by decreasing the β grain size, i.e. the slip length. Moreover, the presence of α_p enhances ductility for equal aging conditions.

Fig. 2.5 b) shows the property profile of bi-modal and β-annealed microstructures considering the presence of grain boundary α layers and the same level of aging. Bi-modal microstructures offer high ductility, resistance to fatigue crack nucleation, low cycle fatigue and resistance to micro crack propagation due to small β grain sizes restricted to the distance between α_p grains. On the other hand, the β-annealed condition offers high yield stress (absence of α_p), creep resistance, fracture toughness and resistance to macrocrack propagation because of the rough crack propagation profile through the boundaries of coarse β grains. For bi-modal microstructures this last aspect can be optimized by using elongated rather than globular α_p grains.

The correlation of properties discussed in this section is based in analysis performed at RT. However, most of the statements are valid for service temperatures up to ~ 400 ºC. At higher temperatures (~ 600 ºC) the effect of alloy element partitioning decreases improving HCF and creep strength [4–6].

2.6. Phase transformations

The microstructural features of α+β and metastable β alloys change continuously during processing due to the progression of phase transformations driven by thermodynamic variables such as temperature, pressure and deformation [7]. Thus, the understanding of the phase transformation kinetics is essential in order to adapt the optimal configuration of alloy design to each specific application.

2.6.1. α – β transformation

Titanium alloys undergo β → α transformation upon cooling from the β field at moderate rates (while diffusion is activated). At the beginning of this process, α nucleates and grows along β grain boundaries as continuous grain boundary α layers (α_{GB}). Thereafter, colonies of α lamellae nucleate at the α_{GB} / β interfaces and grow into the β grain. Lamellae within the same colony are separated by thin layers of β matrix and develop with equal crystallographic orientation until other colonies are reached. Since they are able to configure Widmanstätten structures (especially in metastable β alloys) they are often referred to as α_{WGB} lamellae.

Owing to these characteristics, the β → α transformation is considered as a sympathetic nucleation and growth process that leads to fully lamellar microstructures (see section 2.4) [5,27]. The steps of this transformation are schematically presented in the diagram of Fig. 2.6.

The α → β progression is controlled by the diffusion transfer of slow β-stabilizers (e.g. V or Mo atoms) from α to β . This process determines the degree of element partitioning between both phases, i.e. the enrichment of α and β with their respective element stabilizers [5,27]. As pointed out in section 2.4, this is a decisive microstructural factor to control the mechanical properties during processing, especially during the recrystallization step of bi-modal microstructures.

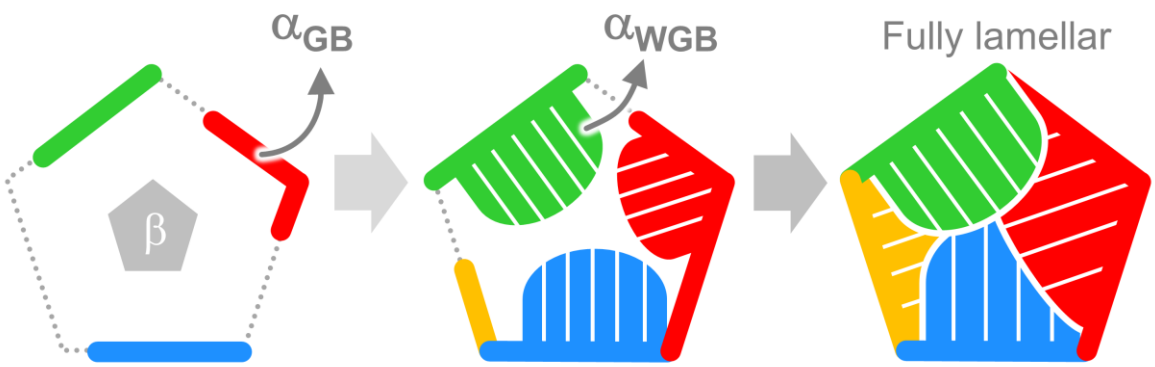

Fig. 2.6. Sequence of formation of α_{GB} and α_{WGB} morphologies during the α → β transformation upon continuous cooling of titanium alloys from the β field.

2.6.2. Metastable phases

Fig. 2.7 shows the β isomorphous phase diagram with the metastable phases forming in titanium alloys by varying their content of β-stabilizers. Formation of α′ and α″ martensites occurs upon β-quenching of alloys with low and high contents of β-stabilizers up to Ms, respectively. This, results in the formation of ω phase in metastable β alloys for concentrations slightly above M_s. Beyond this locus of the diagram, β may be retained either in metastable or stable state. In the first case, decomposition into β and β′ products may occur. Furthermore, formation of α″ and ω phases may take place simultaneously for metastable β alloys that lay close to M_s (e.g. Ti-10V-2Fe-3Al) [4–7].

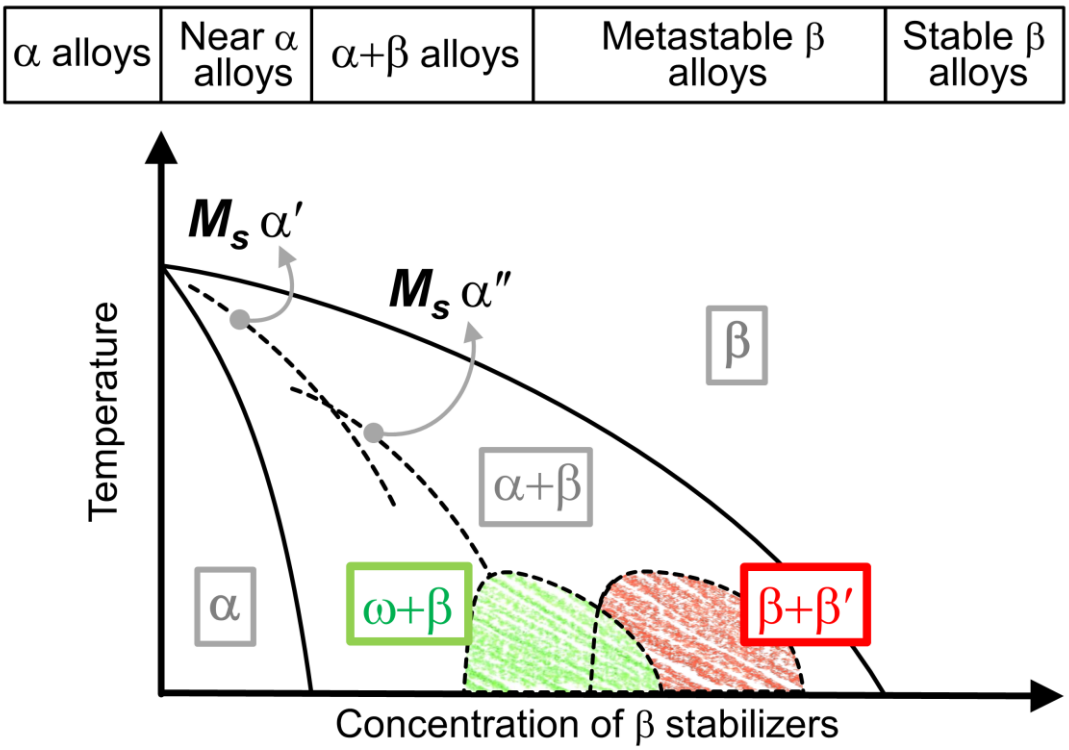

Fig. 2.7. β isomorphous phase diagram (pseudo-binary section) delimiting the areas where formation of metastable phases such as α′ / α″ martensites, ω and β / β′ products (phase separation of β) may occur [5].

2.6.2.1. Martensite

The transformation of martensite occurs through the athermal shear of {110} β planes during quenching or deformation of titanium alloys. This shear leads to the formation of the basal planes of the hcp α′ martensite in alloys presenting low quantities of β stabilizers (Fig. 2.7). On the other hand, if the alloys present higher additions of these elements that

lead to an incomplete shift of planes, the hexagonal symmetry is not reached and the orthorhombic α″ martensite forms instead.

Martensitic transformations can produce either massive or acicular morphologies of martensite in alloys with low and high levels of solute elements, respectively. The first type consists in dense colonies of fine martensite laths (< 1 μm) where no retention of β is observed. Differently, the second type presents arrays of wider individual martensite units (e.g. plates) dispersed in the β matrix. Since there is no defined compositional border between groups, both morphologies may coexist in several alloys [5–7].

In titanium alloys, martensites present supersaturation of substitutional solute elements that are rejected during thermal treatment in the α+β field (martensite tempering) according to the solubility limit reached at each temperature. For alloys containing α′ this process results in the formation of α and β phases ($\alpha' \rightarrow \alpha + \beta$) by precipitation of β in dislocations as well as in plate and twin boundaries. On the other hand, decomposition of α″ martensite is considered to occur by a continuous spinodal process where solute-lean and rich regions of α″ martensite form followed by transformation into α and β ($\alpha'' \rightarrow \alpha''_{lean} + \alpha''_{rich} \rightarrow \alpha + \beta$) [5–7].

2.6.2.2. ω phase

In titanium alloys, the ω phase forms from β basically through two different paths: a) upon quenching from the β field and b) during isothermal aging of the β metastable phase at low temperatures (< 500 ºC). Since these paths are associated with athermal and thermal processes, their corresponding products are usually termed athermal ω (ω_{ath}) and isothermal ω (ω_{iso}) [7,28].

The β → ω transformation consists of a collapse of two-thirds of the {111}β layers into double layers, whereas the other one-third remains as a single layer. During this process the z coordinate of the crystal structure of ω (z_ω) varies continuously between $0 \leq z_\omega \leq 1/6$, where $z_\omega = 0$ represents the bcc β phase and $z_\omega = 1/6$ the ideal ω phase with hexagonal symmetry. Intermediate structures with z_ω between 0 and 1/6 are considered trigonal and are associated with ω_{ath} particles formed in solute depleted regions of β under unstable conditions. This represents generally the initial stage of the ω transformation. Thereafter, diffusion-driven element partitioning where alloying elements are rejected from ω_{ath}

particles into β takes place during heating. This leads to the complete plane collapse of the lattice (ideal ω) and to the subsequent formation and growth of ω_{iso} [7,28,29].

The morphologies of ω_{iso} particles (10 – 100 nm) are either ellipsoidal or cuboidal by distinguishing if they are associated with alloys presenting low (e.g. Ti-V, Cr, Mn, Fe) and high (e.g. Ti-Mo, Nb) misfit strains of the lattice, respectively (critical strain values ~ 0.5 %). Fine ω_{ath} particles (2 – 10 nm) are usually difficult to catalogue but in some cases they tend to be ellipsoidal [7,29].

In Metastable β alloys, ω forms as a homogeneous distribution of fine particles dispersed throughout β grains. This configuration assists the formation of α during aging of these alloys providing a very fine and uniform distribution of α_s plates which can increase the strength of the alloys (see section 2.5). Since there is still no univocal explanation, several hypotheses generate controversy in the transformation mechanism occurring between ω and α phases during heating of metastable β alloys. On the one hand, investigations based in ex situ examinations after aging, suggested direct nucleation of α within ω and at ω / β interfaces [24,30–32]. On the other hand, time resolved bulk diffraction experiments showed the presence of an intermediate phase, α''_{iso} [33–35].

2.6.2.3. Phase separation of β

Decomposition of β may occur upon quenching and subsequent heat treatment of metastable β alloys considerably enriched in β stabilizers (Fig. 2.7). This leads to the formation of β′ and β phases (occasionally referred to as β_1 and β_2) of equal bcc structure but different compositions and lattice parameters: β′ and β are associated with poor and rich solute regions, respectively. The decomposition of β can occur either by nucleation and growth or by spinodal decomposition. The first path consists in the nucleation of second phase particles from localized concentration fluctuations of large amplitude (stable clusters rich in solute), while in the second case, unstable composition fluctuations of small amplitude develop and evolve with the temperature towards the equilibrium [5,7].

The formation of α in alloys undergoing phase separation of β has been suggested to occur either in β′ domains or at β′ / β interfaces during thermal treatment (β → β + β′ → α + β). This transformation path leads to a homogeneous distribution of fine α_s plates within the β matrix, and may vary due to the eventual formation of ω [7].

2.7. Applications

α+β and metastable β titanium alloys are used for diverse applications such as in automotive, energy, power generation, biomedical, sport or offshore industries. However, their largest market (about 80 % of the production) is focused in components for the aerospace sector [4,5,36]. Fig. 2.8 a) shows the fraction of titanium used in airframe (15 wt.%) and engine parts (25 wt.%) of novel commercial aircrafts. Since the material was first introduced in the aerospace industry during the 1950s, these values have gradually increased despite the high manufacturing costs conditioning a more extensive implementation of titanium [36–39]. The alloys studied in this work are used as structural components mainly located in the landing gear system as well as in connections between wing and fuselage (see Fig. 2.8 a) [9,10,40]. In contrast to the data presented in Fig. 2.8 a), the use of titanium in military aircrafts is even higher (up to ~ 20 – 40 wt.% in the airframe). The causes are higher structural loads produced under extreme aerial operations and a less critical role of cost reduction during materials selection [36].

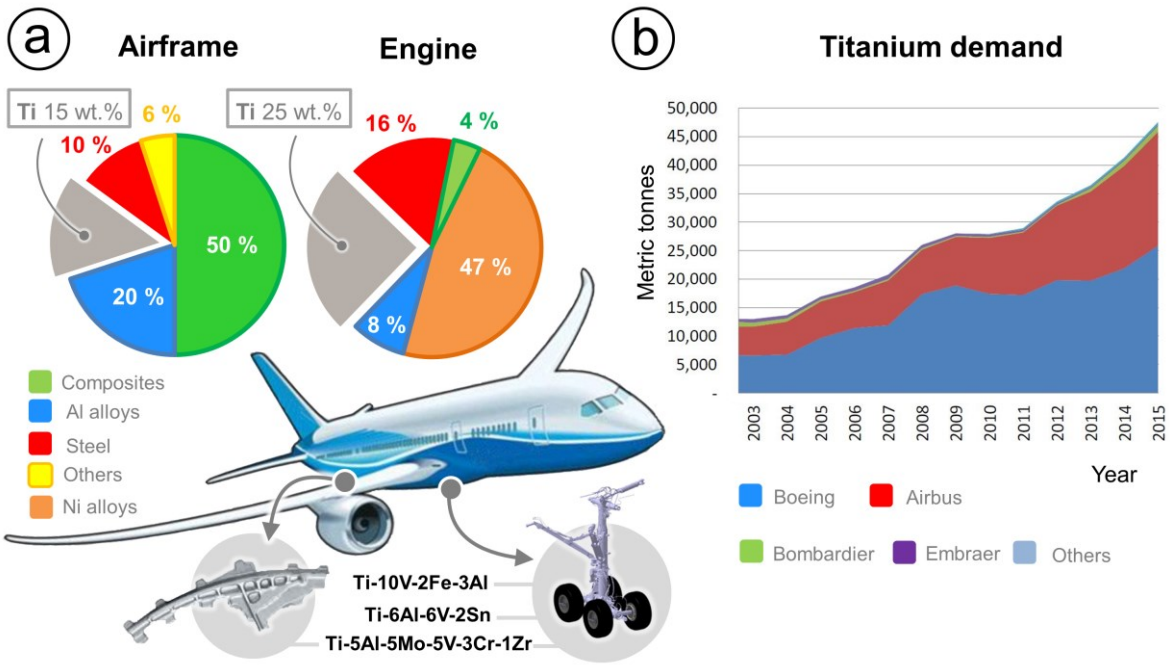

Fig. 2.8. a) Material selection for airframes and gas turbine engines of novel commercial aircrafts (percentage of structural weight) [36,37]. The applications of the studied alloys are mainly located in the landing gear and wing-fuselage connections. **b)** Evolution of the demand of titanium in the last decade for the largest producers of commercial aircrafts [44].

Recent forecasts of the principal commercial aircraft and gas turbine engine producers worldwide announced an acceleration of the build rates for the upcoming next generation products [41,42]. This, together with the associated increasing implementation of titanium in aircrafts explains the material demand outlook for the aerospace sector in the next decade: a compound annual growth rate (CAGR) of 5.9 and 4.4 % for composites and titanium is predicted, respectively, while aluminium remains stable (0.2 % CAGR) [43]. As reported by the largest producers of titanium (Fig. 2.8 b) [39,44], these factors indicate a continuous and positive trend in the demand of this material, and therefore, a buoyant future of titanium in the aerospace industry.

3. Methodology

The microstructural characterization of the studied alloys was carried out using light optical microscopy (LOM), scanning electron microscopy (SEM) and transmission electron microscopy (TEM). On the other hand, the studies of phase transformation kinetics and microstructural tracking of alloying elements were performed combining laboratory with synchrotron-based techniques. The first group of methods include energy-dispersive X-ray spectroscopy (EDX) and differential scanning calorimetry (DSC), while in the second one, in situ high energy synchrotron X-ray diffraction (HEXRD) and synchrotron micro X-ray fluorescence (μ-XRD) were applied. As shown in Fig. 3.1, synchrotron radiation (SR) offers unique advantages for scattering and spectroscopic experiments [45–47].

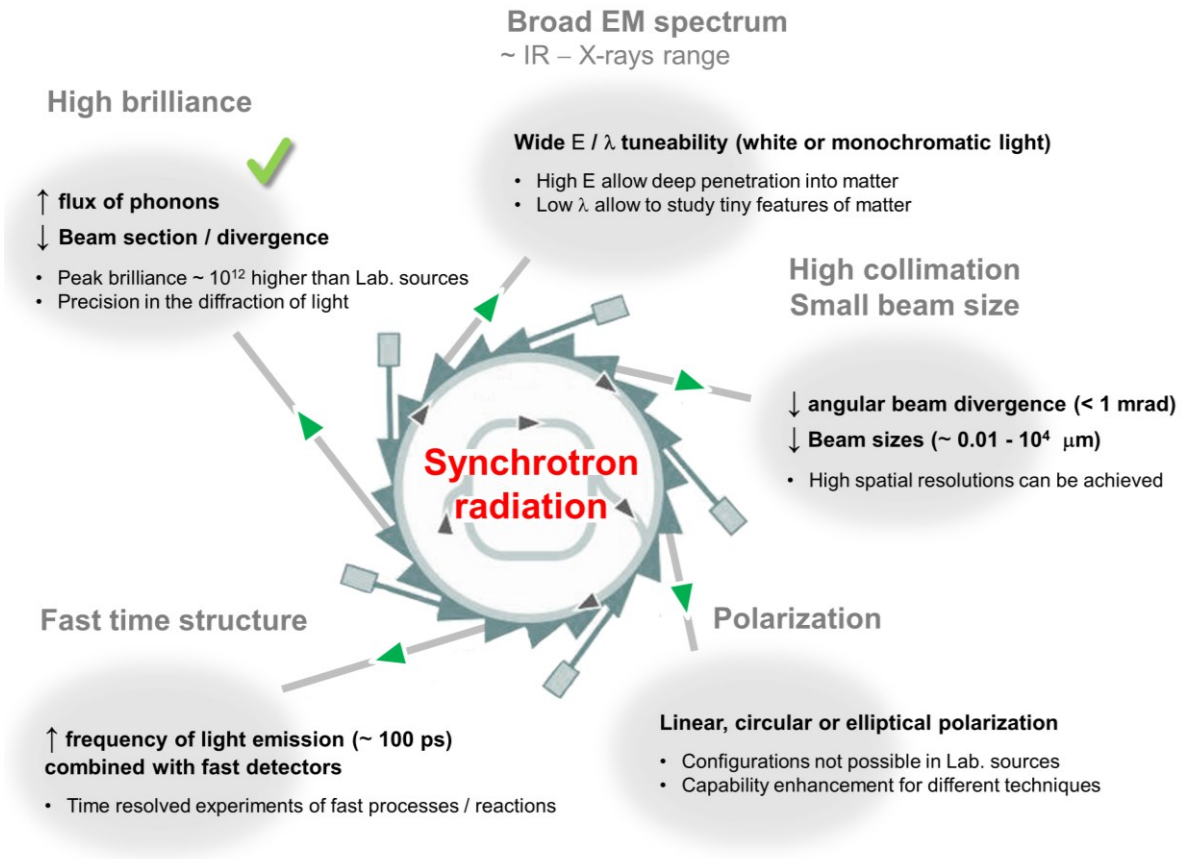

Fig. 3.1. Principal characteristics and advantages of synchrotron radiation.

3.1. In situ high energy synchrotron X-ray diffraction

High energy X-rays (30 – 1000 keV) such as provided by synchrotron radiation sources offer high penetration into matter allowing non-destructive bulk investigations of materials. Thus, this class of X-rays permit to analyse in transmission mode titanium samples of several millimetres (see Fig. 3.2). For diffraction experiments, this configuration is usually combined with 2D detectors placed along the scattering direction behind the sample. High energy X-rays are associated with small scattering angles that offer large mappings of reciprocal space. Thus, complete sets of the Debye-Scherrer rings can be recorded in a single beam shot for polycrystalline materials [48].

The advantages of high energy X-rays, together with the properties of modern image plate detectors, i.e. large active area, high spatial resolution and dynamic range as well as fast acquisition rate, extend the capability of HEXRD to perform time resolved bulk diffraction experiments. This permits evaluating continuously the changes in the crystallographic structure of phases to study in situ the kinetics of phase transformations during thermal treatment [48,49]. The experimental set up used for in situ HEXRD is schematically represented in Fig. 3.2.

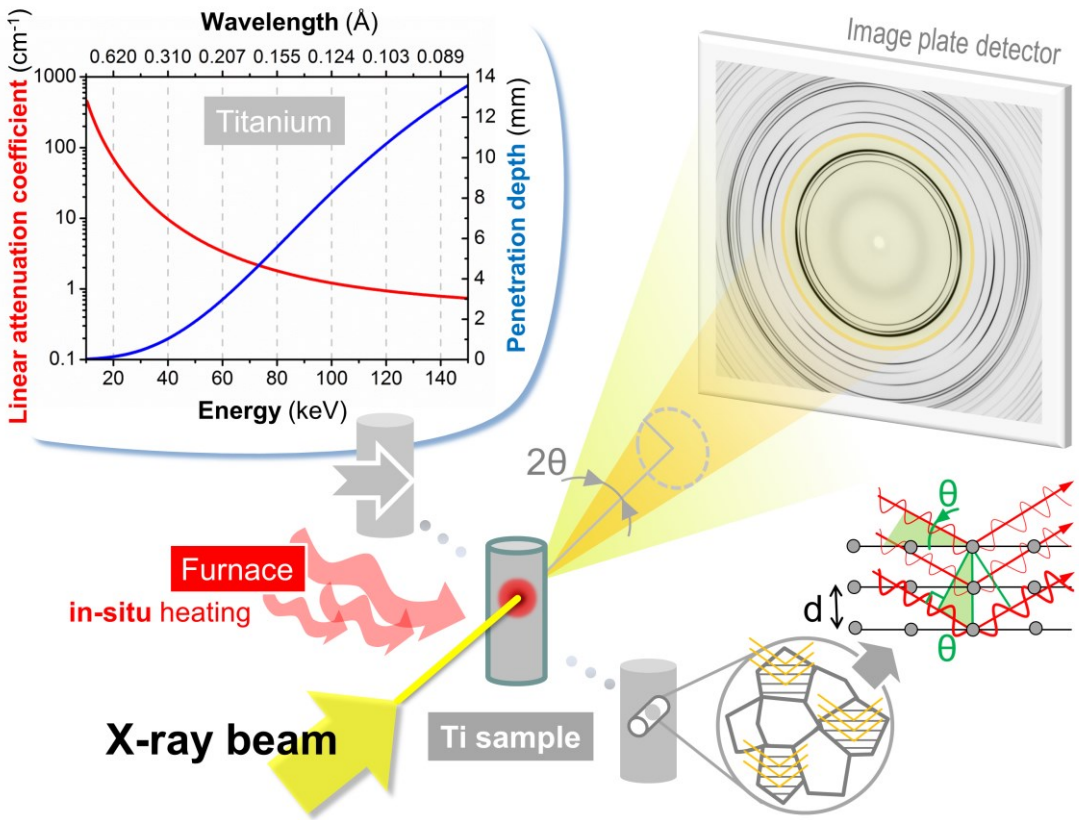

Fig. 3.2. Schematic view of the experimental setup used for in situ HEXRD.

3.2. Synchrotron micro X-ray fluorescence

Synchrotron radiation (see Fig. 3.1) offer great improvements for XRF especially in terms of spatial resolution and sensitivity. For the latter, advances are essentially based in increasing and decreasing signal intensity and background of fluorescence spectra, respectively. On the one hand, high signal intensities can be reached within the broad spectrum of SR, e.g. by employing high energy X-rays. This also offers wide ranges for selective XRF excitation of the sample. On the other hand, the spectral background is a consequence of the radiation scattered from the sample to the detector. This effect is strongly dependent on the polarization of primary radiation, while does not affect the photo absorption (photoelectric effect) responsible of fluorescence radiation. Thus, signal-to-noise ratios can be improved considerably (up to two orders of magnitude) by applying the intrinsic and high linear polarization of SR (> 99.5 %). Furthermore, μ-XRF permits obtaining high spatial resolution as well as micro trace analysis due to the high collimation and small beam sizes (down to ~ 10 – 100 nm) provided by SR [45,50–52].

Fig. 3.3 shows a schematic view of the typical experimental setup used for synchrotron μ-XRF. The vertical plane of the sample is usually positioned at 45 º to the incident beam, while the fluorescence detector is placed in the horizontal plane of the beam and at 90 º to its direction. This configuration tends to maximize the signal-to-noise ratio and avoid saturation of the detector. Micro positioning of the region of interest can be done using a light optical microscope (magnification ≥ 100 ×). In order to carry out high resolution scans, i.e. micro trace analysis, small beam sizes need to be combined with high accuracy positioning of the sample (usually better than ~ 100 nm) [50,53].

Specimens can be normally analysed in air or in a vacuum chamber. In the first case, the air absorption between the sample and detector may reduce or even exclude the detection of light elements with Z ≤ 18. Silicon drift (SD) detectors are widely used due to their excellent energy resolution at very high count rates (up to 1 million cps). In addition to this, they are more compact and lighter than traditional Si (Li) detectors and fast scans are possible (~ 0.1 s / spectrum) [50,53].

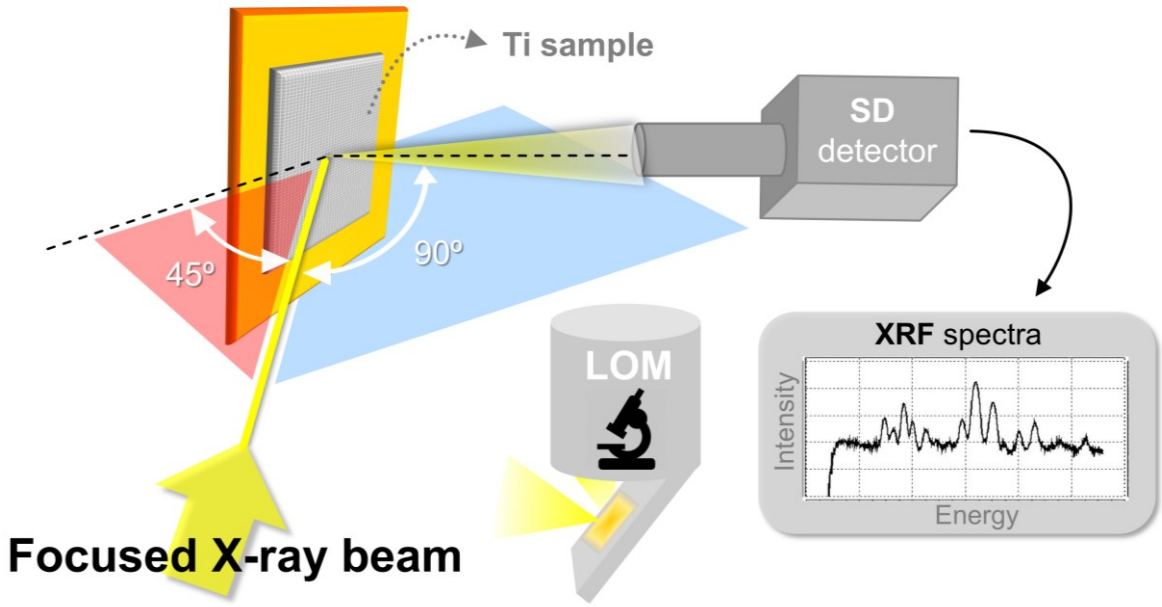

Fig. 3.3. Schematic view of a typical experimental setup used for synchrotron μ-XRF.

The results from quantitative XRF analysis are in many cases considered as semi-quantitative since they are still associated with relatively large errors. However, advances have been made in the development of calibration models based in the use of standards and empirical as well as theoretical schemes describing the interaction of X-rays with matter [54,55]. Particularly, the penetration depth of the XRF signal and the heterogeneity of the samples represent critical factors during quantification.

Table 3.1 compares micro analytical methods used in fluorescence spectroscopy. In addition to the remarked advantages of SR μ-XRF, this technique can usually be combined simultaneously with other techniques such as X-ray absorption spectroscopy (XAS), X-ray fluorescence computed tomography (XFCT) or X-ray diffraction (XRD) [50,55].

Method	Radiation		Resolution		Detection limit	Atmosphere
	Input	Output	Spatial	Depth		
SEM-EDX **EPMA**	e^-	X-rays	~ 0.5 µm	~ 0.5 µm	~ 1000 ppm (Be) ~ 50 ppm (Be)	Vacuum
✗ **The fluorescence signal contains high background and arises from a ~ 1 µm bulk sphere (spread of e^- beam)**						
SIMS	Ions	Secondary ions	~ 5 µm	~ 0.1 nm	~ 0.001 ppm (H)	Vacuum
✗ **Destructive technique where quantification is difficult in many cases**						
PIXE	p^+ (He^{++})	X-rays	~ 2 µm		~ 1 ppm (H)	Vacuum
✗ **Can induce damage to sensitive samples**						
LAMMA	UV	Ions	~ 2 µm		~ 1 ppm (H)	Vacuum
✗ **The non-reproductive laser-induced ionization may difficult the interpretation of mass spectra**						
SR µ-XRF	X-rays	X-rays	~ 10 nm	~ 1 nm	~ 5 ppm (N) Beamline ID18 - ESRF: ~ 0.1 ppm (Z > 25)	Vacuum Gas Liquid
✓ **Non-destructive, ↑ sensitivity (sub-ppm), ↑ spatial resolution (sub-µ), fast scanning in diverse atmospheres**						

Table 3.1. General characteristics of common micro-analytical methods used in fluorescence spectroscopy [52,53].

4. Publications and scientific contribution

4.1. Focus of research

α+β and metastable β alloys cover most of the structural applications of titanium-based components due to their flexible configuration of mechanical properties achievable through microstructural-based alloy design. For the first group of alloys, bi-modal α+β microstructures offer a well-balanced properties' profile, while the β-quenched condition of metastable β alloys provides high strength by formation of fine α_s plates within β grains (see section 2.4 and 2.5).

In the current work, the decomposition kinetics of these microstructures is studied from RT to the β field during continuous heating of the α+β Ti-662 and metastable β Ti-1023 and Ti-55531 alloys with $[Mo]_{eq.}$ = ~ 4, 11.7, 13 wt.%, respectively. The investigations reveal variations in the phase transformation sequences as a function of heating rate.

On the one hand, the bi-modal system permits to analyse the evolution of exclusively stable phases, namely α and β transformed by diffusion-driven mechanisms. On the other hand, the role of metastable products such as α″, ω and β′+β transformed via displacive / diffusive processes is studied during heating of the β-quenched condition.

The evolution of the crystal structure of phases is analysed in terms of their transformation mechanisms. The results and discussions obtained from these investigations are presented as a compendium of articles published in international peer reviewed journals (Fig. 4.1).

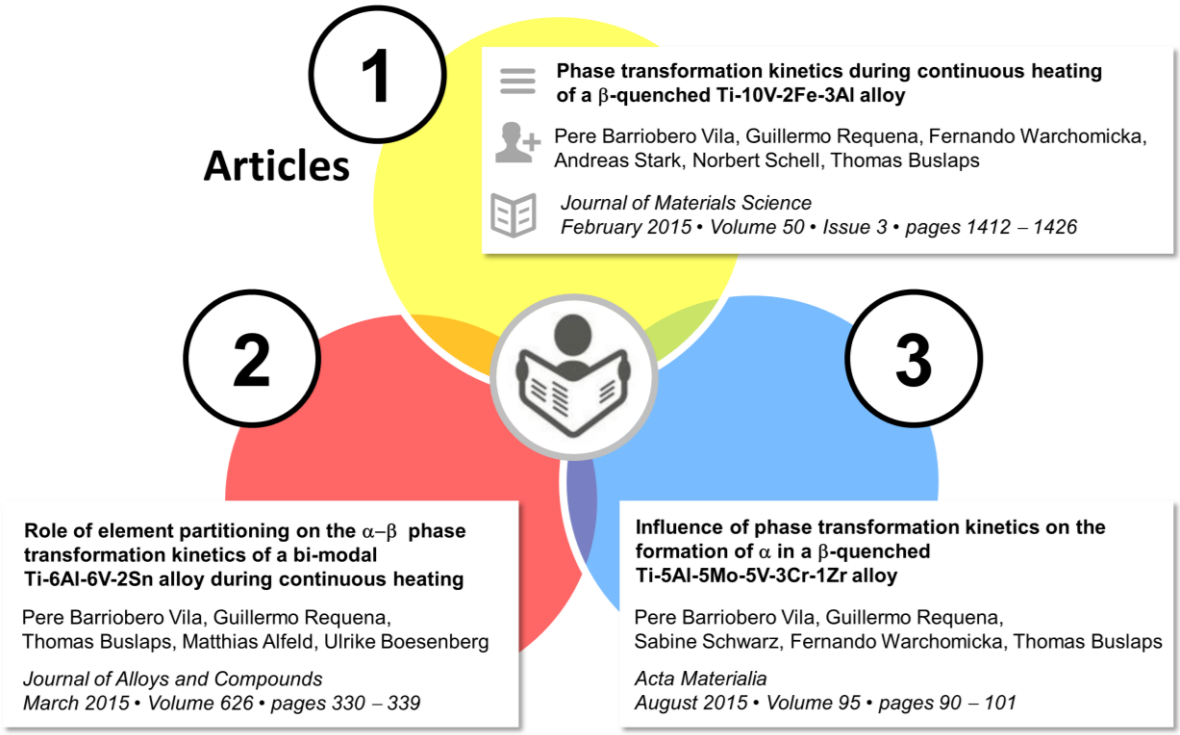

Fig. 4.1. Publications included in this dissertation.

4.2. Articles

Phase transformation kinetics during continuous heating of a β-quenched Ti-10V-2Fe-3Al alloy

The phase transformation kinetics of a metastable β Ti-10V-2Fe-3Al alloy quenched from the β field is investigated as a function of heating rate by fast in situ synchrotron HEXRD and DSC. The initial microstructure consists in α″ martensite and ω_{ath} particles dispersed within the retained β-phase matrix.

A fast athermal α″ → β reversion whose degree of transformation increases with heating rate takes place at low temperatures (~ 170 – 315 °C). A full reversion of α″ into β is observed for the 50 K/min heating rate.

Two origins for the formation of ω phase were identified during heating:

a) At 5 and 20 K/min ω grows from β by a diffusion-driven mechanism.
b) At 50 K/min ω forms from the orthorhombic α″ martensite by a complete and sudden reshearing of lattice strains during the last stages of the α″ → β reversion.

At moderate temperatures (~ 250 – 400 °C) stabilization and growth of solute depleted α″ (α''_{lean}) occurs at 5 and 20 K/min to stabilize the excess of β produced during the martensite reversion. Thereafter, reflections similar to those expected for α″ (α''_{iso}) suddenly grow from ω at ~ 450 °C.

During heating up to ~ 420 – 650 °C α forms through three different paths:

a) From the orthorhombic α″ martensite ($\alpha''_{lean} \rightarrow \alpha$).
b) As an evolution of the orthorhombic structure transformed from the ω phase ($\omega \rightarrow \alpha''_{iso} \rightarrow \alpha$).
c) From the β phase ($\beta \rightarrow \alpha$).

The evolution of stable and metastable phases was univocally analysed in terms of volume fraction and the crystallographic relationships between their lattice structures. This allowed a complete and unambiguous determination of the phase transformation sequences of the Ti-10V-2Fe-3Al alloy during linear heating from RT to the β field.

Role of element partitioning on the α – β phase transformation kinetics of a bi-modal Ti-6Al-6V-2Sn alloy during continuous heating

The role of element partitioning on the phase transformation kinetics of a α+β Ti-6Al-6V-2Sn alloy with initial bi-modal microstructure is studied experimentally as a function of heating rate. The investigations combine quantitative phase analysis with elemental analysis. Fast in situ synchrotron HEXRD and conventional metallographic analysis provide the evolution of phase volume fractions and lattice parameters, while synchrotron μ-XRF and EDX are applied to trace microstructural distribution of alloying elements during thermal treatment.

At the beginning of the heating, the lattice parameters of α and β phases undergo a linear increase up to ~ 400, 450 and 590 ºC for 5, 20 and 100 K/min, respectively. This effect is associated with thermal expansion of the lattice since similar coefficients of thermal expansion as well as no compositional and volume fraction variations of phases are observed at this stage of the heating.

A β → α transformation takes place for low heating rates during thermal treatment up to intermediate temperatures. This results in a simultaneous increase in the volume fraction of

α and decrease in the lattice parameter a_β between 430 – 530 ºC and 500 – 560 ºC during heating at 5 and 20 K/min, respectively. The diffusion-driven mechanisms controlling these processes are reflected in the element partitioning determined experimentally between phases: α and β are enriched by their respective stabilizing elements (Al for α, and V, Cu, Fe for β), while Ti atoms diffuse from β to α. This loss of Ti affects a low volume fraction of β phase susceptible to pronounced compositional changes. This, together with the fact that Ti presents the largest atomic radius among alloying elements explains the local minimum exhibited by the lattice parameter a_β.

During further heating up to T_β a steep increase of the a_β lattice parameter occurs in parallel with the α → β transformation. The kinetic effect of both processes, i.e. the shift of their onsets to higher temperatures with increasing heating rate, can be confirmed up to 750 and 800 ºC (33 vol.% of β) for 5 and 100 K/min, respectively, where a_β presents similar expansion in both cases. Thereafter, a_β is larger for 5 K/min indicating that other effects, such as compositional differences, may also play a role at this stage of the α → β transformation. Microstructural evidences of the role of V during phase transformation are provided owing to the high spatial resolution and elemental sensitivity achieved by μ-XRF.

The analysis of phase transformation kinetics combining laboratory and synchrotron-based techniques provided an advance in the current knowledge of the phase transformation kinetics of the Ti-6Al-6V-2Sn alloy during linear heating from RT to the β field. Such investigations provide substantial experimental data for the development of theoretical models still mostly confined to phase equilibria and, consequently, contribute to knowledge-based thermal treatment optimization.

Influence of phase transformation kinetics on the formation of α in a β-quenched Ti-5Al-5Mo-5V-3Cr-1Zr alloy

The effect of phase transformation kinetics on the formation of α in a metastable β Ti-5Al-5Mo-5V-3Cr-1Zr alloy quenched from the β field is studied as a function of heating rate. Fast in situ synchrotron HEXRD is applied to provide continuous evolution of phase volume fractions and lattice parameters, while metallographic analysis are performed to evaluate the mechanisms of phase transformation at different heating stages.

Initially, the microstructure is formed by a matrix of equiaxed metastable β grains with ω_{ath} particles located along dislocations and within domains associated with spinodal decomposition of β. This last effect is characterized by an irregular distribution of discontinuous β′ / β domains that represent composition fluctuations along [200] β. At the initial stage of slow heating (~ 350 – 500 ºC) the ω_{ath} → ω transformation occurs with further decomposition of β. This last effect leads to a symmetric arrangement of continuous domains that contribute to the formation of ω.

During slow heating up to ~ 400 – 550 ºC the orthorhombic α''_{iso} phase forms from ω through the sequence *dislocation* (ω_{ath}) → ω → α''_{iso}. These particles grow by the transfer of solute atoms from β to α''_{iso}. Thereafter, further heating up to moderate temperatures (~ 600 – 650 ºC) leads to the formation of α phase via two different paths:

a) Slow heating rates result in a homogeneous distribution of fine α plates formed through the evolution of ω (ω → α''_{iso} → α).

b) Fast heating rates supress this mechanism and promote the formation of α only from β grain boundaries (β → α).

Quantitative phase analysis performed continuously during linear heating provided a straight and unambiguous determination of the phase transformation sequences of the Ti-5Al-5Mo-5V-3Cr-1Zr alloy from RT to the β field. This permitted to identify and analyse mechanisms of phase transformation as well as to evaluate the microstructural response to variations in the transformation kinetics of phases.

Glossary

bcc	Body-centred cubic
CAGR	Compound annual growth rate
d	d-spacing: interplanar atomic distance
DSC	Differential scanning calorimetry
E	Energy
e^-	Electron
EDX	Energy dispersive X-ray spectroscopy
EM	Electromagnetic
EPMA	Electron probe microanalysis
HCF	High cycle fatigue
hcp	hexagonal close packed
HEXRD	High energy X-ray diffraction
IR	Infrared radiation
K_{IC}	Critical fracture toughness
Lab	Laboratory
LAMMA	Laser ablation microprobe mass analysis
LCF	Low cycle fatigue
LOM	Light optical microscopy
M_s	Martensite start temperature
p^+	Proton
PIXE	Proton induced X-ray emission
RT	Room temperature
SEM	Scanning electron microscopy
SIMS	Secondary ion mass spectroscopy
SR	Synchrotron radiation
TEM	Transmission electron microscopy
Ti-662	Ti-6Al-6V-2Sn alloy
Ti-1023	Ti-10V-2Fe-3Al alloy
Ti-55531	Ti-5Al-5Mo-5V-3Cr-1Zr alloy
T_β	β-transus temperature

UV	Ultraviolet radiation
XAS	X-ray absorption spectroscopy
XFCT	X-ray fluorescence computed tomography
XRD	X-ray diffraction
XRF	X-ray fluorescence
Z	Atomic number
z_ω	*z* coordinate of the crystal structure of ω
ΔK_{MACRO}	Fatigue Macro-crack propagation
ΔK_{MICRO}	Fatigue Micro-crack propagation
α	hcp phase in titanium alloys
α′	hcp martensite in titanium alloys
α″	Orthorhombic martensite in titanium alloys
α_{GB}	Grain boundary α phase
α''_{iso}	Metastable orthorhombic phase in titanium alloys
α_p	Primary α phase
α_s	Secondary α phase
α_{WGB}	Widmanstätten grain boundary α lamellae
β	bcc phase in titanium alloys
β′	Metastable solute-lean bcc phase in titanium alloys
ε_F	Final strain
λ	Wave length
μ-XRF	Micro X-ray fluorescence
$\sigma_{0.2}$	Yield stress
ω	Metastable hexagonal / trigonal phase in titanium alloys
ω_{ath}	Non-ideal ω phase forming under athermal conditions
ω_{iso}	Ideal ω phase forming under thermal conditions
$[Al]_{eq}$	Aluminium equivalent content
$[Mo]_{eq}$	Molybdenum equivalent content
2θ	Diffraction angle

References

[1] Advisory Council for Aviation Research and Innovation in Europe, ACARE: Strategic research and innovation agenda, September 2012, accessed 16 July 2015, <ftp://ftp.cordis.europa.eu/pub/technology-platforms/docs/sria-executive-summary.pdf>.

[2] F.H. Froes, Current and emerging opportunities in titanium's expanding market, JOM 59 (2007) 27.

[3] A.K. Sachdev, K. Kulkarni, Z.Z. Fang, R. Yang, V. Girshov, Titanium for automotive applications: challenges and opportunities in materials and processing, JOM 64 (2012) 553–565.

[4] C. Leyens, M. Peters, Titanium and titanium alloys, first ed., Wiley-VCH, Weinheim, 2003.

[5] G. Lütjering, J.C. Williams, Titanium, second ed., Springer, Berlin, 2007.

[6] D. Banerjee, J.C. Williams, Perspectives on titanium science and technology, Acta Mater. 61 (2013) 844–879.

[7] S. Banerjee, P. Mukhopadhyay, Phase transformations: examples from titanium and zirconium alloys, first ed., Elsevier, Oxford, 2007.

[8] CES Edupack software, Granta Design Limited, Cambridge, 2010.

[9] M. Wollmann, J. Kiese, L. Wagner, Properties and applications of titanium alloys in transport, in: L. Zhou, H. Chang, Y. Lu, D. Xu (Eds.), Ti-2011, Science Press Beijing, Beijing, 2012, pp. 837–844.

[10] R.R. Boyer, An overview on the use of titanium in the aerospace industry, Mat. Sci. Eng. A 213 (1996) 103–114.

[11] F.H. Froes, H. Friedrich, J. Kiese, D. Bergoint, Titanium in the family automobile: the cost challenge, JOM 56 (2004) 40–44.

[12] M. Jackson, Automotive applications for titanium, in: D. Crolla, D.E. Foster, T. Kobayashi, N. Vaughan (Eds.), Encyclopedia of automotive engineering, Wiley, 2015, pp 3126–3139.

[13] B.E. Hurless, F.H. Froes, Lowering the cost of titanium, Amptiac 6 (2002) 3–9.

[14] M. Jackson, K. Dring, A review of advances in processing and metallurgy of titanium alloys, Mater. Sci. Technol. 22 (2006) 881–887.

[15] M.A. Imam, F.H. Froes, R.G. Reddy, Cost effective developments for fabrication of titanium components, Key Eng. Mater. 551 (2013) 3–10.

[16] R.R. Boyer, D.U. Furrer, The potential advantages of microstructure modeling of titanium to the aerospace industry, in: S. Ghosh, J.M. Castro, J.K. Lee (Eds.), Numiform 2004, AIP Conference proceedings, New York, 2004, pp. 1694–1699.

[17] S. Malinov, W. Sha, Modeling thermodynamics, kinetics, and phase transformation morphology while heat treating titanium alloys, JOM 57 (2005) 42–45.

[18] S.L. Semiatin, S.L. Knisley, P.N. Fagin, F. Zhang, D.R. Barker, Microstructure evolution during alpha-beta heat treatment of Ti-6Al-4V, Metall. Mater. Trans. A 34 (2003) 2377–2386.

[19] A. Krumphals, C. Poletti, F. Warchomicka, M. Stockinger, C. Sommitsch, Modeling of two-phase grain structure in the titanium alloy Ti-6Al-4V using cellular automata, Int. J. Mult. Comp. Eng. 12 (2014) 23–31.

[20] S. Malinov, W. Sha, The neural network modeling of titanium alloy phase transformation and mechanical properties, JOM 57 (2005) 54–57.

[21] S.M.C. Van Bohemen, M. Van der Laars, J. Sietsma, S. Van der Zwaag, Modelling of the $\beta \rightarrow \alpha+\beta$ transformation in a metastable β Ti alloy based on the growth kinetics and the morphology of the α plates, Int. J. Mater. Res. 98 (2007) 476–484.

[22] Y. Ohmori, T. Ogo, K. Nakai, S. Kobayashi, Effects of ω-phase precipitation on $\beta \rightarrow \alpha, \alpha''$ transformations in a metastable β titanium alloy, Mater. Sci. Eng. A 312 (2001) 182–188.

[23] O.M. Ivasishin, P.E. Markovsky, S.L. Semiatin, C.H. Ward, Aging of coarse- and fine-grained β titanium alloys, Mater. Sci. Eng. A 405 (2005) 296–305.

[24] S. Nag, R. Banerjee, R. Srinivasan, J.Y. Hwang, M. Harper, H.L. Fraser, ω-assisted nucleation and growth of α precipitates in the Ti-5Al-5Mo-5V-3Cr-0.5Fe β titanium alloy, Acta Mater. 57 (2009) 2136–2147.

[25] S. Bein, J. Béchet, Phase transformation kinetics and mechanisms in titanium alloys Ti-6.2.4.6, β-CEZ and Ti-10.2.3, J. Phys. IV 6 (1996) 99–108.

[26] S. Malinov, W. Sha, P. Markovsky, Experimental study and computer modeling of the $\beta \rightarrow \alpha+\beta$ phase transformation in β21s alloy at isothermal conditions, J. Alloy. Compd. 348 (2003) 110–118.

[27] S. Malinov, W. Sha, Titanium alloys: modelling of microstructure, properties and applications, Woodhead Publishing, Cambridge, 2009, pp. 203–236.

[28] C.B. Basak, S. Neogy, D. Srivastava, G.K. Dey, S. Banerjee, Disordered bcc γ-phase to δ-phase transformation in Zr-rich U-Zr alloy, Philos. Mag. 91 (2011) 3290–3306.

[29] A. Devaraj, S. Nag, R. Srinivasan, R.E.A. Williams, S. Banerjee, R. Banerjee, H.L. Fraser, Experimental evidence of concurrent compositional and structural instabilities leading to ω precipitation in titanium-molybdenum alloys, Acta Mater. 60 (2012) 596–609.

[30] Y. Ohmori, T. Ogo, K. Nakai, S. Kobayashi, Effects of ω phase precipitation on β → α, α″ transformations in a metastable β titanium alloy. Mater. Sci. Eng. A 312 (2001) 182–188.

[31] M. Ahmed. T. Li, G. Casillas, J.M. Cairney, D. Wexler, E.V. Pereloma, The evolution of microstructure and mechanical properties of Ti-5Al-5Mo-5V-2Cr-1Fe during aging, J. alloy. Compd. 629 (2015) 260–273.

[32] N.G. Jones, R.J. Dashwood, M. Jackson, D. Dye, β phase decomposition in Ti-5Al-5Mo-5V-3Cr, Acta Mater. 57 (2009) 3830–3839.

[33] O.M. Ivasishin, P.E. Markovsky, S.L. Semiatin, C.H. Ward, Aging of coarse- and fine-grained β titanium alloys, Mater. Sci. Eng. A 405 (2005) 296–305.

[34] S. Malinov, W. Sha, Z. Guo, C.C. Tang, A.E. Long, Synchrotron X-ray diffraction study of the phase transformations in titanium alloys, Mater. Charact. 48 (2002) 279–295.

[35] E. Aeby-Gautier, A. Settefrati, F. Bruneseaux, B. Appolaire, B. Denand, M. Dehmas, G. Geandier, P. Boulet, Isothermal α″ formation in β metastable titanium alloys, J. alloy. Compd. 577 (2013) 439–443.

[36] A.P. Mouritz, Introduction to aerospace materials, first ed., Woodhead, Cambridge, 2012.

[37] Aeromagazine Boeing commercial, 2006, accessed 16 July 2015, <http://www.boeing.com/commercial/aeromagazine/articles/qtr_4_06/AERO_Q406_article4.pdf>.

[38] Fastener World magazine, May-June 2014, accessed 16 July 2015, <http://www.fastener-world.com.tw/0_magazine/ebook/pdf_download/FW_146_E_178.pdf>.

[39] Titanium Metals Corporation (TIMET), Commercial aerostructures market finally ready for take-off, September 2014, accessed 16 July 2015, <http://c.ymcdn.com/sites/www.titanium.org/resource/resmgr/TiUSA2104Papers/SeinerHenryTiUSA2014WorldDem.pdf>.

[40] R.R. Boyer, R.D. Briggs, The use of β titanium alloys in the aerospace industry, J. Mater. Eng. Perform. 14 (2005) 681–685.

[41] ATI Metals, Creating value thru relentless innovation, July 2014, accessed 16 July 2015, <https://www.atimetals.com/Documents/q2_2014_conference_call.pdf>.

[42] ATI Metals, Titanium demand and trends in the jet engine market, September 2014, accessed 16 July 2015, <http://c.ymcdn.com/sites/www.titanium.org/resource/resmgr/TiUSA2104Papers/LeachWadeTiUSA2014WorldDeman.pdf>.

[43] Aviation Consultancy Services and Solutions (ICF SH&E), Aerospace supply chain & raw material outlook, March 2014, accessed 16 July 2015, <https://www.singaporeairshow.com/downloads/market_info/Aerospace_Supply_Chain_&_Raw_Material_Outlook__March_2014.pdf>.

[44] VSMPO, Commercial aerospace demand, October 2011, accessed 16 July 2015, <http://c.ymcdn.com/sites/www.titanium.org/resource/resmgr/2010_2014_papers/MetzMichael_2011.mpdf>.

[45] S. Mobilio, F. Boscherini, C. Meneghini, Synchrotron radiation: basics, methods and applications, first ed., Springer, Berlin, 2015.

[46] H. Saisho, Y. Gohshi, Applications of synchrotron radiation to materials science, first. ed., Elsevier Science, Amsterdam, 1996.

[47] W. Reimers, A.R. Pyzalla, A. Schreyer, H. Clemens, Neutrons and synchrotron radiation in engineering materials science, first ed., Wiley-VCH, Weinheim, 2008.

[48] K.D. Liss, A. Bartels, A. Schreyer, H. Clemens, High-Energy X-rays: a tool for advanced bulk investigations in materials science and physics, Texture. Microstruct. 35 (2003) 219–252.

[49] B.B. He, Two-dimensional X-ray diffraction, first ed., Wiley, New Jersey, 2009.

[50] F. Adams, B. Vekemans, G. Silversmit, B.D. Samber, L. Vincze, Microscopic X-ray fluorescence analysis with synchrotron radiation, in: A. Vértes, S. Nagy, Z Klencsár, R.G.

Lovas, F. Rösch (Eds.), Handbook of Nuclear Chemistry, Springer, Dordrecht, 2011, pp. 1737–1760.

[51] J. Heckel, R.W. Ryon, Polarized beam X-ray fluorescence analysis, in: R.E. Van Grieken, A.A. Markowicz (Eds.), Handbook of X-ray spectroscopy, Marcel Dekker AG, New York, 2002, pp 10-I – 10-VII.

[52] M. Haschke, Relations to other analytical methods, in: M. Haschke (Ed.), Laboratory micro-X-ray fluorescence spectroscopy, first ed., Springer, Switzerland, 2014, pp 211–227.

[53] A. Simionovici, P. Chevallier, Micro-XRF with synchrotron radiation, in: B. Beckhoff, B. Kanngiesser, N. Langhoff, R. Wedell, H. Wolff (Eds.), Handbook of practical X-ray fluorescence analysis, Springer, Berlin, 2006, pp. 474–497.

[54] K. Janssens, W. De Nolf, G. Van Der Snickt, L. Vincze, B. Vekemans, R. Terzano, F.E. Brenker, Recent trends in quantitative aspects of microscopic X-ray fluorescence analysis, Trend. Anal. Chem. 29 (2010) 465–477.

[55] K. Janssens, M. Alfeld, Van Der Snickt, W. De Nolf, F. Vanmeert, M. Radepont, L. Monico, J. Dik, M. Cotte, G. Falkenberg, C. Miliani, B.G. Brunetti, Annu. Rev. Anal. Chem. (2013) 399–425.

J Mater Sci (2015) 50:1412–1426
DOI 10.1007/s10853-014-8701-6

Phase transformation kinetics during continuous heating of a β-quenched Ti–10V–2Fe–3Al alloy

Pere Barriobero-Vila · Guillermo Requena · Fernando Warchomicka · Andreas Stark · Norbert Schell · Thomas Buslaps

Received: 9 July 2014 / Accepted: 3 November 2014 / Published online: 14 November 2014

Abstract The effect of heating rate on the phase transformation kinetics of a Ti–10V–2Fe–3Al metastable β titanium alloy quenched from the β field is investigated by fast in situ high energy synchrotron X-ray diffraction and differential scanning calorimetry. The initial microstructure is formed by α″ martensite and fine ω_{ath} particles distributed in the retained β-phase matrix. The phase transformation sequence varies with the heating rate as revealed by analysis of the continuous evolution of crystallographic relationships between phases. At low temperatures an athermal reversion of α″ martensite into β takes place. This reversion occurs to a larger extent with increasing heating rate. On the other hand, diffusion–driven precipitation and growth of the ω phase is observed for lower heating rates accompanying the reverse martensitic transformation. Furthermore, the results show that the stable α phase can form through three different paths: (a) from the ω phase, (b) from α″ martensite, and (c) from the β phase.

Electronic supplementary material The online version of this article (doi:10.1007/s10853-014-8701-6) contains supplementary material, which is available to authorized users.

P. Barriobero-Vila (✉) · G. Requena · F. Warchomicka
Institute of Materials Science and Technology, Vienna University of Technology, Karlsplatz 13/308, 1040 Vienna, Austria
e-mail: pere.vila@tuwien.ac.at

G. Requena
e-mail: guillermo.requena@tuwien.ac.at

F. Warchomicka
e-mail: fernando.warchomicka@tugraz.at

F. Warchomicka
Institute for Materials Science and Welding, Graz University of Technology, Kopernikusgasse 24, 8010 Graz, Austria

Introduction

Metastable β titanium alloys are mostly used in a wide range of components for the aerospace industry and as alternative structural materials for the automotive sector due to their high specific strength and excellent fatigue resistance [1, 2]. Moreover, biomedical applications are also being considered due to biocompatibility of β-Ti alloys and partial or total superelasticity [3]. The mechanical properties of these alloys for structural applications are basically defined by a homogeneous distribution of α/β interfaces due to the presence of fine α precipitates embedded in a β matrix [4]. On the other hand, the superelastic behavior is associated to a reverse martensitic transformation that leads to shape memory effect [5]. The formation of the α phase, its morphology, volume fraction, size, distribution as well as the progression of eventual shape memory effect are influenced by the phase transformation kinetics during heat treatments [6]. Therefore, a correct understanding of these processes is required for the optimization of the heat treatment and chemical composition of the alloys. In most of the prior works the

A. Stark · N. Schell
Helmholtz-Zentrum Geesthacht, Centre for Materials and Coastal Research, Max-Planck-Str. 1, 21502 Geesthacht, Germany
e-mail: andreas.stark@hzg.de

N. Schell
e-mail: norbert.schell@hzg.de

T. Buslaps
ID15, European Synchrotron Radiation Facility, Rue J. Horowitz, 38042 Grenoble, France
e-mail: buslaps@esrf.fr

study of phase transformations in metastable β titanium alloys was discussed on the basis of isothermal aging and ex situ experiments [7–11]. Although important insights have been gained using these methods, the role played by kinetic variables (e.g., heating rate) on the phase transformation sequence has received less attention [12–14]. Nowadays, continuous and univocal studies of phase transformation kinetics during heat treatment can be carried out in situ by high energy synchrotron X-ray diffraction (HEXRD) [15–17].

The Ti–10V–2Fe–3Al metastable β titanium alloy is extensively used in aircraft components such as landing gear structures or helicopter rotors [2, 18]. Depending on the thermomechanical process, this alloy can develop bimodal, lamellar, or fine α plate microstructures that offer better combinations of tensile strength, fatigue resistance, and fracture toughness than α + β titanium alloys [18, 19].

In the present study, the phase transformations kinetics of a Ti–10V–2Fe–3Al alloy in β-quenched state are determined in situ as a function of the heating rate by means of HEXRD and complemented by differential scanning calorimetry (DSC). The evolution of stable and metastable phases is analyzed in terms of volume fraction and the crystallographic relationships between their lattice structures during linear heating from room temperature (RT) to the β-field.

Experimental

Material

The composition of the investigated metastable β titanium alloy Ti–10V–2Fe–3Al is given in Table 1. The β-transus temperature of the as-received primary ingot is 800 °C [20]. Samples of 20 × 20 × 30 mm^3 were cut from the as-received ingot and subjected to an isothermal heat treatment at 900 °C (β-field) for 20 min in a dynamic argon atmosphere and quenched in RT water. This water-quenched condition corresponds to the initial condition for the further investigations.

Microstructural characterization

Specimens were prepared for light optical microscopy (LOM) by electropolishing for 35 s at RT in a LectroPol-5 machine using a solution of 8 % $HClO_4$ + 12 % 2-butoxyethanol + 80 % ethanol and a voltage of 40 V. This procedure was effective in removing the presence of stress-induced α″ martensite formed during mechanical polishing [6]. Subsequently, the samples were immersed for 20 s in a Kroll's reagent solution (2 % HF + 4 % HNO_3 + 94 % H_2O) to reveal the microstructural constituents. LOM was carried out using a Zeiss Axioplan optical microscope. The grain size was determined using the ASTM standard E 1382-91 as implemented in the software Axio Vision 4.8.2.

Thin-foil specimens were prepared for transmission electron microscopy (TEM) by dimpling followed by ion milling using a Gatan precision ion polishing system (PIPS) device employed at 4 kV. The samples were examined with a Tecnai F20 microscope operated at 200 kV.

Study of phase transformation kinetics

DSC and in situ HEXRD were used to determine the phase transformation kinetics of the Ti–10V–2Fe–3Al alloy. The evolution of phases was studied during continuous heating at constant heating rates of 5, 20, and 50 °C min^{-1} from RT up to 900 °C.

Differential scanning calorimetry

DSC was carried out in a Netzsch DSC 404C Pegasus calorimeter using specimens of ~5 mm diameter and ~1.6 mm thickness (~145 mg) cut using a SiC disk. A pure Al_2O_3 sample was used as a reference. The investigated samples and the reference were inserted into Al_2O_3 pans. The DSC experiments were performed in argon 5.0 atmosphere with a flow rate of ~80 ml min^{-1} to avoid oxidation. The DSC curves show a continuous sequence of reaction peaks that make it difficult to determine a reference baseline. Therefore, the start and finish temperatures of individual reactions were determined by the inflection points between them as described in [21, 22].

In situ high energy synchrotron X-ray diffraction

In situ HEXRD was carried out at two different synchrotron radiation sources: ID15B beamline of the European Synchrotron Radiation Facility (ESRF, Grenoble) [23] and P07-HEMS beamline at PETRA III, Deutsches Elektronen-Synchrotron (DESY, Hamburg) [24]. The experimental parameters for each setup are summarized in Table 2. Samples of 4 × 4 × 20 mm^3 (ID15B) and 4 × 4 × 10 mm^3 (P07) were cut using a SiC disk. The ID15B samples were heated

Table 1 Composition of the Ti–10V–2Fe–3Al alloy [20]

Element	V	Al	Fe	O	C	N	H	Y	Ti	$[Mo]_{eq}$
Wt%	9.24	3.25	1.86	0.12	0.023	0.011	0.0008	<0.005	Balance	~11.7

Table 2 Experimental parameters used during the in situ HEXRD experiments (20 and 50 °C min^{-1} heating at ID15B-ESRF and 5 °C min^{-1} heating at P07-Petra III)

Beamline	Energy (keV)	Wavelength (Å)	Slit-aperture size (mm^2)	Sample-detector distance (mm)	Acquisition time (s)	Read-out time (s)	Detector
ID15B-ESRF	87	0.142	0.3 × 0.3	1252	2	1	Pixium
P07-PetraIII	100	0.124	1 × 1	1918	4	2	PerkinElmer XRD 1622

up in a dynamic argon 4.6 atmosphere by means of a radiant furnace [16]. A modified dilatometer Bähr 805A/D with an induction coil furnace [25] was used at the P07-HEMS beamline to heat up the samples in a helium 5.0 atm. In both cases, the samples were kept fixed during acquisition and the temperature was controlled by a spot-welded thermocouple located next to the position of the incoming beam. Image sequences of complete Debye–Scherrer rings from the bulk of the samples were recorded in transmission mode (*thickness* = 4 mm) using image-plate detectors (see Table 2).

Analysis of diffraction data

The instrumental parameters of each setup were obtained using a LaB_6 powder standard. Qualitative analysis of the evolution of the diffraction patterns during heating was carried out using two procedures:

(1) Azimuthal integration of the intensity along the Debye–Scherrer rings at each temperature using the software Fit2d [26].
(2) Unrolling the Debye–Scherrer rings and converting them into Cartesian coordinates (azimuthal angle, 2θ) and projection of the maximum intensity on the 2θ axis using the software ImageJ [27].

Quantitative phase analysis of the diffraction patterns, such as the evolution of volume fraction of phases and the cell parameters, was determined by the Rietveld method as implemented in the software Maud [28].

Results

Initial microstructure

Figure 1a shows a light optical micrograph of the initial microstructure of the Ti–10V–2Fe–3Al alloy. Large α″ martensite plates can be observed distributed at the grain boundaries of the retained β matrix. This is clearly shown in the inset of Fig. 1a where α″ martensite plates nucleated at the β grain boundaries can be observed. Moreover, the β grains present equiaxed morphology with a mean diameter of ~400 μm. Analogous microstructures have been reported for Ti–10V–2Fe–3Al quenched from the β-field [6, 7].

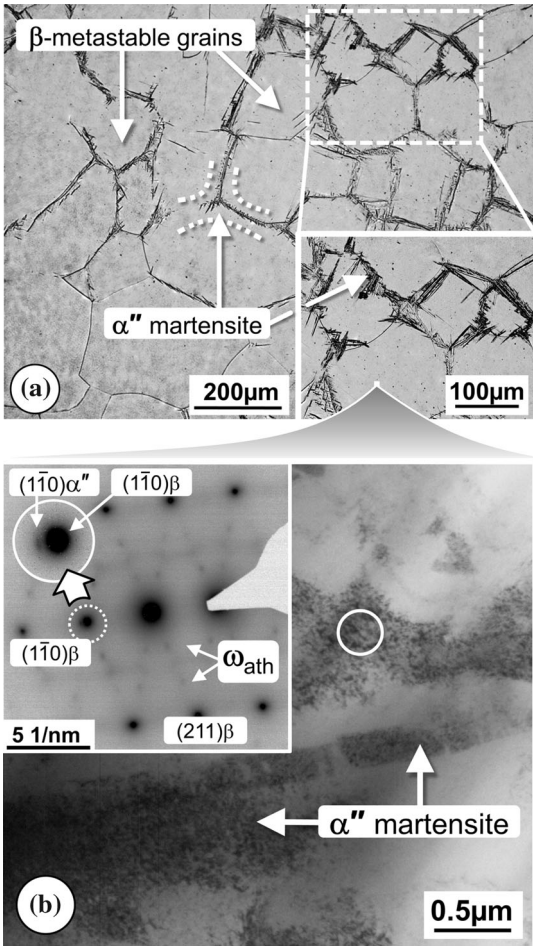

Fig. 1 **a** LOM image of the initial microstructure formed by a matrix of metastable β grains surrounded by α″ martensite plates. **b** TEM bright field image of the initial microstructure showing fine laths and larger plates of α″ martensite. The *inset* in **b** presents the electron diffraction pattern of the [$\bar{1}\bar{1}$3] β zone axis in the *circled region* and reveals the presence of ω_{ath}

TEM of the initial microstructure reveals that α″ martensite can also be found distributed in the β matrix as lath colonies and as plates (Fig. 1b). Figure 1b refers to a region located in the interior of β grains. In addition, irregularly shaped and very fine (1–10 nm) particles corresponding to the athermal ω phase (ω_{ath}) are also found within the β matrix and in between the α″ martensite. Particles of ω_{ath} with a mean size of ~3 nm have been reported for the current alloy after quenching from the β-

field [7]. The inset in Fig. 1b shows the ω_{ath} and α'' phases identified by electron diffraction in the encircled region. $(1\bar{1}0)$ spots of α'' appear next to those from $(1\bar{1}0)$ of β [29]. Furthermore, characteristic features of ω_{ath} such as sharp spots and diffuse intensity distribution (diffuse ω [30], diffuse streaking [31]) can be observed. Similar electron diffraction patterns denoting the presence of ω_{ath} were reported in previous works [30–33]. The nature of diffuse scattering in ω_{ath} has been interpreted in terms of incoherent precipitates [34]. Moreover, it has been suggested that the ω_{ath} precipitates are formed to relax the strain caused by the volume expansion from the β phase to the α'' martensite during quenching [35, 36]. Therefore, it can be expected that the ω_{ath} precipitates are located at the α''–β interface, but this cannot be revealed with the spatial resolution obtained by TEM in this work.

Influence of heating rate on phase transformations during continuous heating

Differential scanning calorimetry

Figure 2 presents the DSC results obtained during continuous heating of the initial microstructure. The DSC curves show that the heat flow during the thermal treatment increases with the heating rate. The three curves present similar peak (transformation) sequences with a shift to higher temperatures with increasing heating rate. The endothermic transformations are indicated by numbers enclosed in circles, while the exothermic ones are shown by numbers in squares. Corresponding peaks at each heating rate are connected by grey lines. The 20 and 50 °C min^{-1} conditions present the same number of peaks (7). A shift of 15–50 °C is observed for the reactions taking place at 50 °C min^{-1} with respect to 20 °C min^{-1} heating rate. On the other hand, the 5 °C min^{-1} curve shows two exothermic transformations in the range between 380 and 435 °C (peak 4), and the transformation sequence is shifted 15–40 °C to lower temperatures with respect to the 20 °C min^{-1} condition. The endothermic peak 7 shows an asymmetric shape that may be due to an overlapping of two or more endothermic transformations. Except for this peak and the two peaks 4 at 5 °C min^{-1}, each exothermic peak is followed by an endothermic transformation and vice versa, indicating formation and transformation of phases, respectively [13, 14, 37].

In situ high energy synchrotron X-ray diffraction

Portions of characteristic Debye–Scherrer rings obtained by HEXRD during heating at 5 and 50 °C min^{-1} can be observed in Fig. 3. They correspond to diffraction patterns

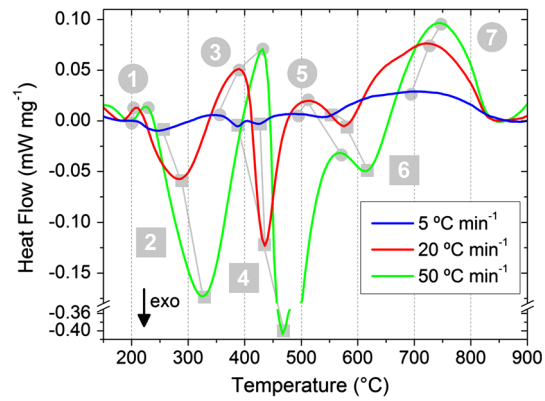

Fig. 2 DSC heat flow curves obtained during continuous heating of the initial microstructure at 5, 20, and 50 °C min^{-1} up to 900 °C. The equivalent peaks between conditions are connected by *grey lines*. The peaks are *numbered* in ascending order during continuous heating. Peaks related to endothermic and exothermic reactions are indicated by *circles* and *squares*, respectively (Color figure online)

at four different temperatures in order to illustrate the rings' evolution. The images shown in Fig. 3a, b were obtained during experiments carried out at the beamlines P07-PetraIII and ID15B-ESRF, respectively. The diffuse ring observed near the center of Fig. 3b corresponds to the scattering of a quartz glass capsule used to keep the sample in inert gas atmosphere. The relatively large grain size of the initial microstructure is reflected by the spotty structure of the diffraction patterns at 25 °C. The diffraction rings of the 5 °C min^{-1} experiment appear more continuous than those of the 50 °C min^{-1} experiment due to the larger gauge volume investigated using the setup at P07 (see Table 2). At 370 °C, some Debye–Scherrer rings observed at 25 °C for 50 °C min^{-1} disappear while new reflections appear. On the other hand, all the rings observed at 25 °C for the 5 °C min^{-1} condition remain and some coarse spots as well as new weak reflections appear. The next two temperatures (450 and 600 °C) show basically the same diffraction rings with similar scattering angles. Furthermore, the diffraction pattern at 450 °C for the 50 °C min^{-1} condition shows streaks that link coarse grains to one or more low intensity spots with a straight line forming a cross-like shape (two of these regions are highlighted by circles in Fig. 3). These streaks indicate orientation relationships in the transforming region of the grain [38].

The evolution with temperature of the integrated diffraction patterns is shown in Fig. 4a, b for a small 2θ range that represents qualitatively the complete HEXRD experiments for the 5 and 50 °C min^{-1} heating rates, respectively. It must be pointed out that the ratio between peak intensities is not representative of the volume fraction of the respective phases due to the small 2θ range depicted. The results for the 20 °C min^{-1} heating rate are between those for 5 and 50 °C min^{-1} conditions and have been

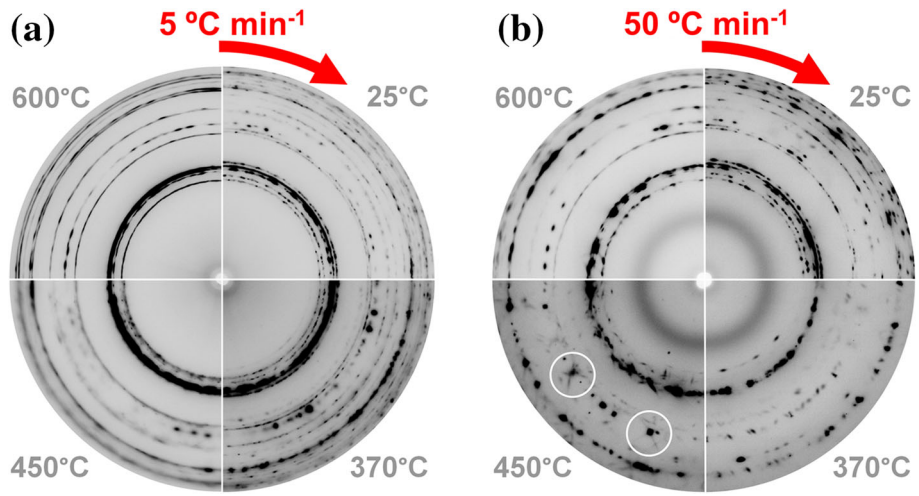

Fig. 3 Quarters of representative Debye–Scherrer rings obtained at 25, 370, 450, and 600 °C during continuous heating: **a** 5 °C min^{-1} (P07-PetraIII) and **b** 50 °C min^{-1} (ID15B-ESRF)

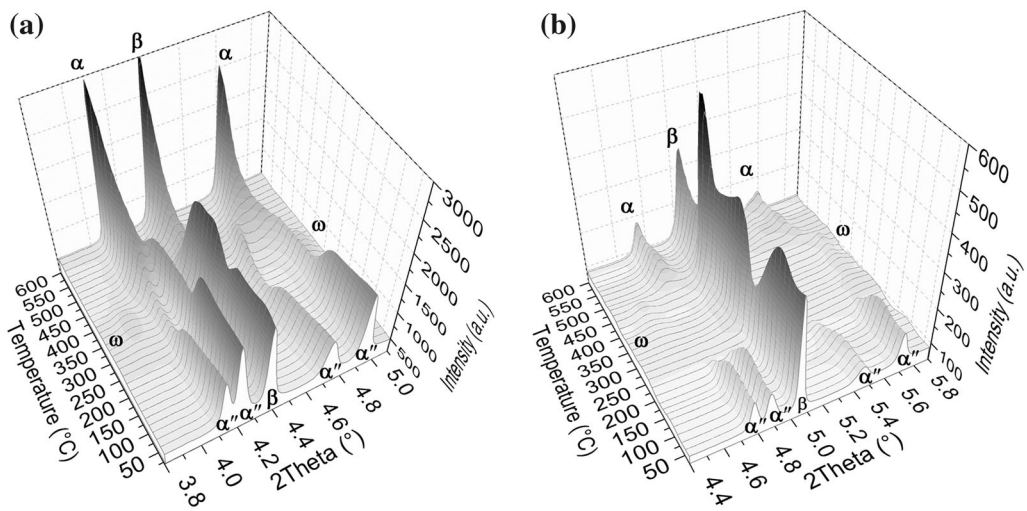

Fig. 4 Evolution of the diffraction patterns (limited to a small 2θ range) as a function of temperature during continuous heating up to 600 °C: **a** 5 °C min^{-1} (P07-PetraIII) and **b** 50 °C min^{-1} (ID15B-ESRF)

excluded to improve legibility. The β and α″ phases are revealed by the diffraction patterns at 25 °C in all studied samples. No evidence of the ω_{ath} phase identified by electron diffraction in the transmission electron microscope could be obtained by HEXRD in the initial condition of the alloy. This may be due to an overlapping of the highest intensity ω_{ath} reflections with the more extensive β-peaks, and the weak and broad ω_{ath} reflections resulting from the diffuse scattering of this phase associated to lattice distortions [39]. The difficulty in identifying ω_{ath} in metastable β titanium alloys by X-ray diffraction has been reported by several authors [16, 35, 40].

A sudden intensity decrease of the α″ reflections, followed by an increase in the intensity of the β-reflection can be observed between 200 and 260 °C. The α″ intensity drop is more pronounced for the 50 °C min^{-1} heating rate, where the α″ reflections practically vanish. This is a diffusionless reverse α″ → β transformation which is responsible for the one-way shape memory effect that is observed in the Ti–10V–2Fe–3Al alloy [6]. This can be seen more clearly in Fig. 5a, b where the Debye–Scherrer rings are presented in Cartesian coordinates for the 50 °C min^{-1} heating rate at 25 and 265 °C, respectively. The {*hkl*} indices of the reflections of the various phases are indicated. At 265 °C (Fig. 5b) the α″ reflections have vanished, while a pronounced and localized intensity increase of some β spots takes place. On the other hand, Fig. 6 shows the changes that take place in an equivalent temperature range for the 5 °C min^{-1} condition. Here, only a partial extinction of α″ is observed at 250 °C (Fig. 6b) as evidenced by an intensity reduction of the reflections of this phase. Also, the β reflections remain less coarse than for the 50 °C min^{-1} heating rate (Fig. 5b). This indicates that the reverse α″ → β transformation is more pronounced

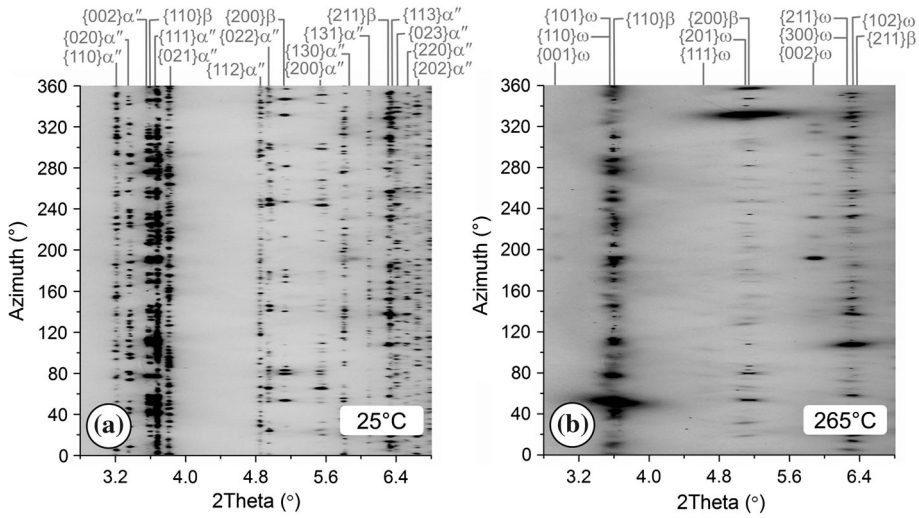

Fig. 5 Complete Debye–Scherrer rings converted into Cartesian coordinates for the 50 °C min^{-1} heating experiment: **a** RT and **b** 265 °C, after reverse martensitic transformation

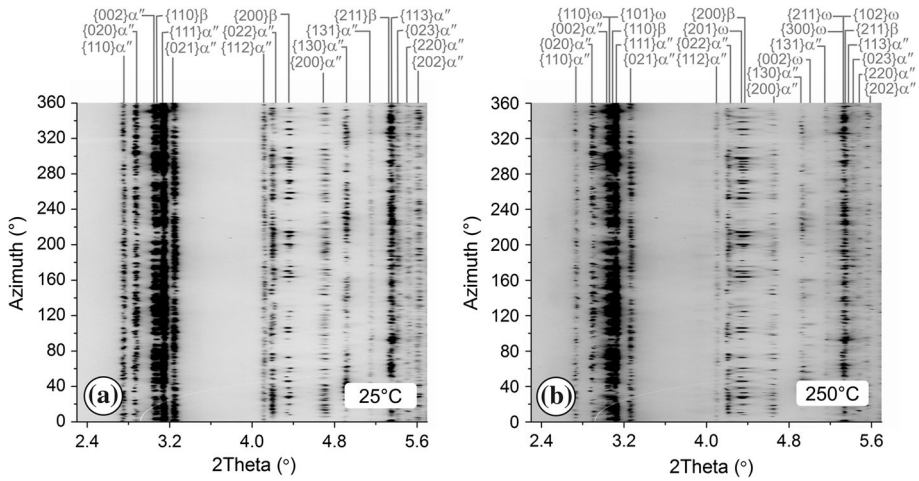

Fig. 6 Complete Debye–Scherrer rings converted into Cartesian coordinates for the 5 °C min^{-1} heating experiment: **a** RT and **b** 250 °C

with increasing heating rate [6] and results in a full transformation of α″ into β at 50 °C min^{-1}.

Another characteristic of the diffraction patterns shown in Figs. 5b and 6b is the emergence of low intensity spots that correspond to the ω phase. This is a thermally activated phase known as isothermal ω (referred to as ω in this work) (see [41]). Families of spots associated to {110}, {101}, {201}, {300}, {211}, and {102} reflections of ω lay next to the 2θ positions where the {110}, {200}, and {211} reflections of β are located. This overlapping causes the apparent fluctuations in the intensity of β observed in Fig. 4 at ~250 °C.

Figure 7a, b shows color-coded 2D plots corresponding to the evolution of several {*hkl*} reflections during continuous heating at 5 °C min^{-1} up to 600 °C for characteristic 2θ ranges. The reflections of the α″ phase are attenuated at ~250 °C owing to the partial reverse α″ → β transformation. In addition, the interplanar distance of the {020}α″, {021}α″, and {130}α″ decreases reaching a minimum at ~275 °C and then increases up to ~450 °C until approximately the same values as for RT are reached. On the contrary, the {110}α″, {111}α″, and {200}α″ reflections follow the opposite behavior. Additionally, at ~250 °C the intensity of the {201} reflection of ω increases. The {110}, {101}, {111}, and {002} of ω become distinguishable at ~325 °C. All ω reflections vanish at ~400 °C. At this temperature the α″ reflections start to shift towards the position of α while their intensity decreases. New reflections indicated by arrows slightly above ~400 °C appear next to {200}α″ and {130}α″. The α″ reflections disappear between 425 and 450 °C. Reflections corresponding to the stable α phase can be appreciated at $T >$ ~525 °C.

The sudden vanishing of α″ reflections at ~200 °C due to the full reverse martensitic transformation into β can be clearly observed in Fig. 8 for 50 °C min^{-1} heating rate. Similar to 5 °C min^{-1}, the reflections associated to ω become visible at ~350 °C and disappear slightly

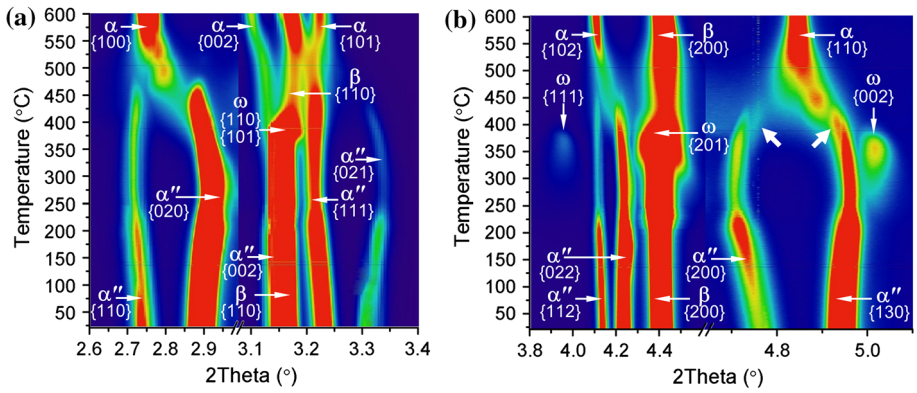

Fig. 7 *Color-coded* 2D plots corresponding to the evolution of several {*hkl*} reflections during continuous heating at 5 °C min^{-1} up to 600 °C for characteristic 2θ ranges: **a** 2.6–3.4° and **b** 3.8–5.1° (Color figure online)

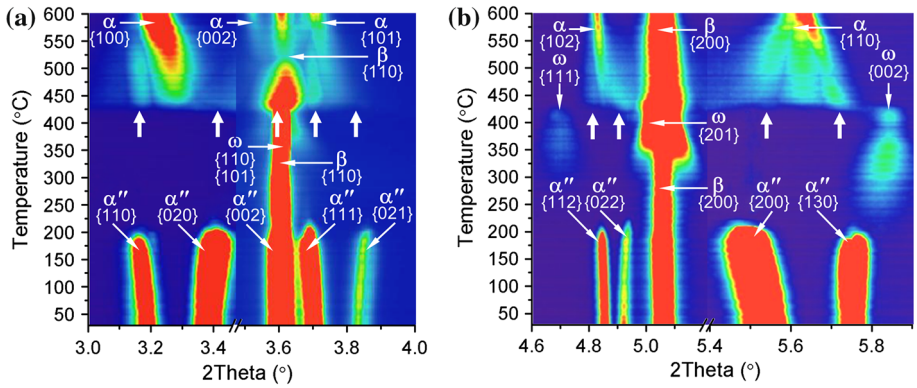

Fig. 8 *Color-coded* 2D plots corresponding to the evolution of several {*hkl*} reflections during continuous heating at 50 °C min^{-1} up to 600 °C for characteristic 2θ ranges: **a** 3.0–4.0° and **b** 4.6–5.9° (Color figure online)

below ~450 °C. Also, new reflections (indicated by arrows) that do not correspond to α″ martensite, β, ω or α but are similar to those expected for α″ martensite start to form at this temperature. These reflections move towards the position of the α phase up to ~550 °C, where clear stable α phase reflections can be observed. A relationship between ω and the new reflections can be observed in Fig. 8b at 425 °C, where the {002}ω reflection shifts to a position close to that of {130}α″. Figure 9 shows a detail of the same {*hkl*} reflections as in Figs. 7b and 8b over a small azimuth range at three characteristic temperatures for the 5, 20, and 50 °C min^{-1} heating rates. At 25 °C, the reflections corresponding to α″ and β are present. At 400, 415, and 450 °C (ascending with the heating rate) the ω reflections start to disappear for each heating rate, showing that the reflection {002}ω shifts towards the position of {130}α″. This corresponds to the period at which the reflections indicated by arrows close to α″ become visible in Figs. 7b and 8b. Furthermore, streaking can be observed between the overlapping {201}ω and {200}β reflections, and the reflections {200}α″ and {022}α″. For the 20 and 50 °C min^{-1} conditions, extra spots between {200}α″ and {130}α″ (indicated by arrows) are visible. At 450, 455, and 490 °C (bottom figures) the streaking effect still remains for each heating rate and the {112}α″ with {022}α″ and {200}α″ with {130}α″ reflections tend to join. These evolutions can be visualized more clearly in the following video sequences: Online Resources 1, 2, and 3, respectively.

Discussion

The phase transformations observed by in situ HEXRD were described qualitatively in the last section. Hereafter, these processes are studied by quantitative phase analysis using the Rietveld method as implemented in the software Maud [28]. This requires the knowledge of the crystallographic structure of the phases involved during the transformations, namely α, α″, ω, and β, which are summarized in Table 3. The structures of the metastable α″ and ω phases are described by the respective y and z_ω parameters, which are directly related to the transformation mechanisms of these phases. The α″ phase is believed to be the result of an incomplete shear of the {110}β planes as they tend to transform into the basal planes of hexagonal α′ martensite during quenching or deformation of metastable β titanium alloys [42]. Due to its lower symmetry, the α″ phase is considered to be a disordered phase in which shuffle displacements from the transformation can be reflected in the atomic y-coordinate [30] (Table 3). An α hcp structure is obtained for $y = 1/6$, $b/a = \sqrt{3}$, while for

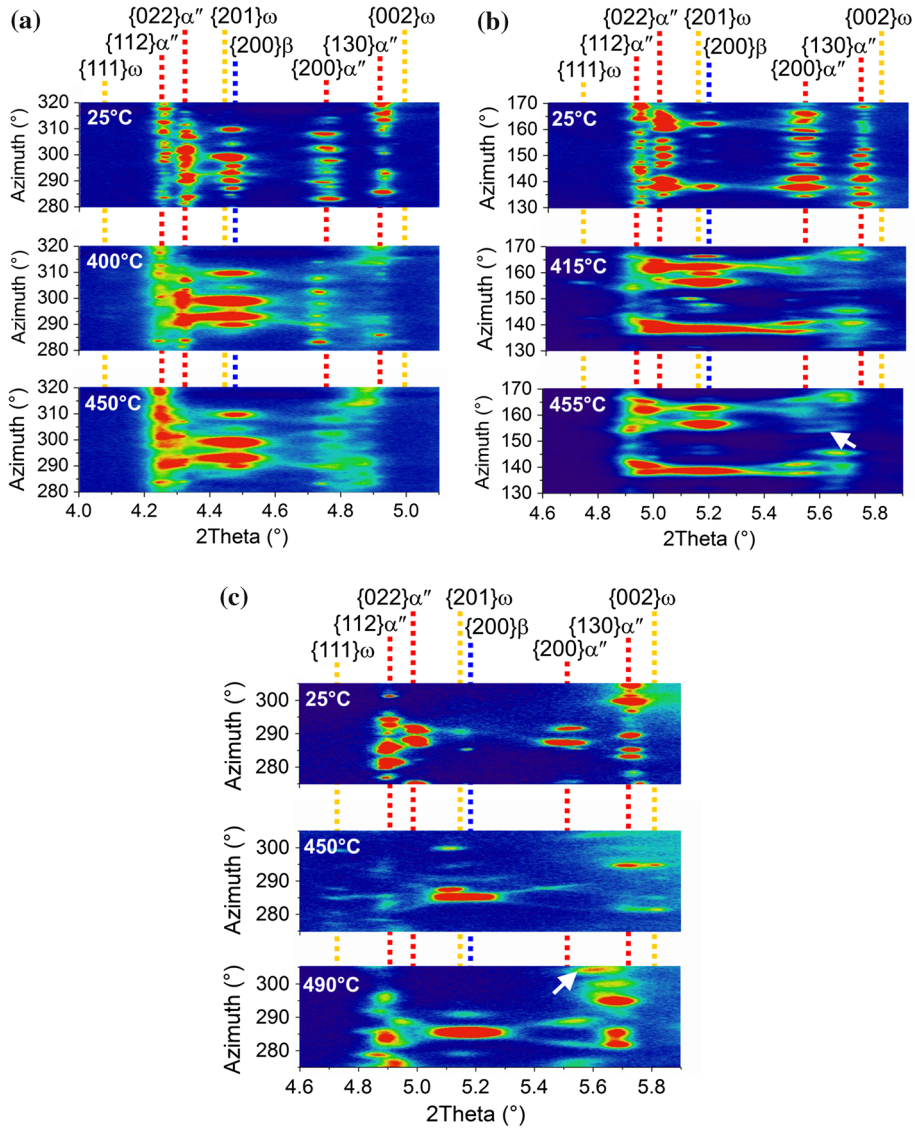

Fig. 9 *Color-coded* 2D plots of selected portions of complete Debye–Scherrer rings converted into Cartesian coordinates. The evolution of the Bragg reflections is shown for three different temperatures: **a** 5 °C min^{-1}, **b** 20 °C min^{-1}, and **c** 50 °C min^{-1} (Color figure online)

a β bcc structure $y = 1/4$, $b/a = \sqrt{2}$ [43]. Possible α″ martensite structures lie between these values. In the current work, $y \sim 0.186$ was determined by Rietveld refinement for the initial microstructure of Ti–10V–2Fe–3Al. Prior studies showed that for Ti–Nb alloys the y-coordinate increases with the solute content [43–45]. This value lies between those found for the binary metastable β Ti–14Nb ($y = 0.1810$) and Ti–20Nb ($y = 0.1877$) alloys [44]. Higher values for the y-coordinate ($\sim$0.222) were reported for higher contents of Nb ($\sim$24 wt%) [43].

The formation of the ω phase consists of a collapse of two-thirds of the {111}β layers into double layers, whereas the other one-third remains as a single layer [30]. During the transformation, z_ω varies continuously between $0 \leq z_\omega \leq 1/6$. In this way, $z_\omega = 0$ corresponds to the bcc β phase, while $z_\omega = 1/6$ is the ideal ω phase with hexagonal symmetry. Structures with z_ω between 0 and 1/6 are considered trigonal [41]. The relationship between the cell parameters of the β and the hexagonal ω phase can be expressed as $a_\omega = \sqrt{2}a_\beta$ and $c_\omega = \sqrt{3}/2a_\beta$ [46]. In the current work no intermediate states of the ω phase are considered in the Rietveld analysis since this assumption resulted in the best refinement of the diffraction patterns. However, it is important to remember that certain volume fraction of ω_{ath} was observed by diffraction analysis of a selected area in TEM (Fig. 1b).

Kinetics of the athermal α″ → β reversion

The phase transformations observed in the temperature range between 170 and 315 °C (see Figs. 5, 6, 7, 8) involve the α″, ω, and β phases. Figure 10 shows the evolution of the phase volume fractions as a function of temperature for the three different heating rates. At the beginning of the

Table 3 Crystallographic data from characteristic phases of Ti-based alloys identified in the HEXRD patterns and used for quantitative phase analysis

Phase	Lattice system	Space group	Atomic positions	Reference
α″	Orthorhombic	*Cmcm*	(0, *y*, 1/4) (0, 1 − *y*, 3/4) (1/2, 1/2 + *y*, 1/4) (1/2, 1/2 − *y*, 3/4); in this work *y* ∼ 0.186 for the initial microstructure	[45]
β	Cubic	$Im\bar{3}m$	(0, 0, 0) (1/2, 1/2, 1/2)	[43]
ω	Hexagonal	*P6/mmm*	(0, 0, 0) (1/3, 2/3, 1/3 + z_ω) (2/3, 1/3, 2/3 − z_ω); in this work z_ω = 1/6*	[41]
α	Hexagonal	$P6_3/mmc$	(1/3, 2/3, 1/4) (2/3, 1/3, 3/4)	[43]

* A trigonal ω structure is obtained for $0 \leq Z_\omega \leq 1/6$

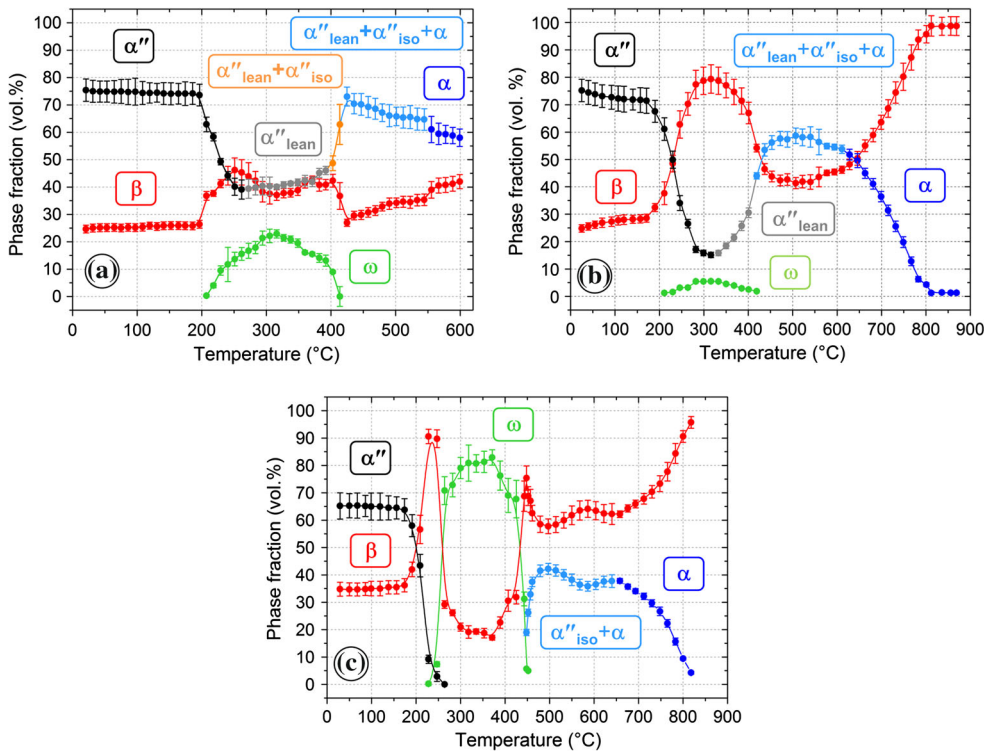

Fig. 10 Evolution of the phase volume fractions as a function of the temperature during continuous heating: **a** 5 °C min^{-1}, **b** 20 °C min^{-1}, and **c** 50 °C min^{-1}

heating the 5 and 20 °C min^{-1} conditions present an α″ content of ∼70–80 vol% while the 50 °C min^{-1} condition shows an initial content of ∼60–70 vol%. As it will be pointed out later these differences may be due to slight differences in the distribution of quenching strains in the samples. The apparent difference in volume fraction of martensite with respect to the light optical micrograph in Fig. 1a can be understood taking into account that the martensite is also present embedded in the β-matrix as it is shown in Fig. 1b. At ∼200 °C all heating rates present a fast α″ → β reversion whose magnitude increases with heating rate. Thus, the volume fraction of α″ martensite after reversion in the 5 and 20 °C min^{-1} conditions reaches a minimum of ∼40 and ∼15 vol%, respectively. On the other hand, the 50 °C min^{-1} condition shows a full transformation of α″ into β. Moreover, Fig. 11 presents the evolution of the cell parameters as a function of temperature for the three different heating rates. During heating from RT to the end of the α″ → β reversion (dashed grey lines in Fig. 11), $b_{\alpha''}$ and $a_{\alpha''}$ decrease and increase, respectively, while $c_{\alpha''}$ remains practically constant. These changes are more accentuated for the 20 °C min^{-1} condition between 250 and 300 °C (Fig. 11b). Furthermore, the temperature at which the minimum α″ volume fraction is reached for the 5 and 20 °C min^{-1} conditions at the end of the α″ → β reversion coincides with that of the minimum and maximum reached for the $b_{\alpha''}$ and $a_{\alpha''}$ cell parameters, respectively.

The athermal α″ → β reversion is a diffusionless transformation caused by thermal mismatch stresses generated during heating from RT at the interface between α″

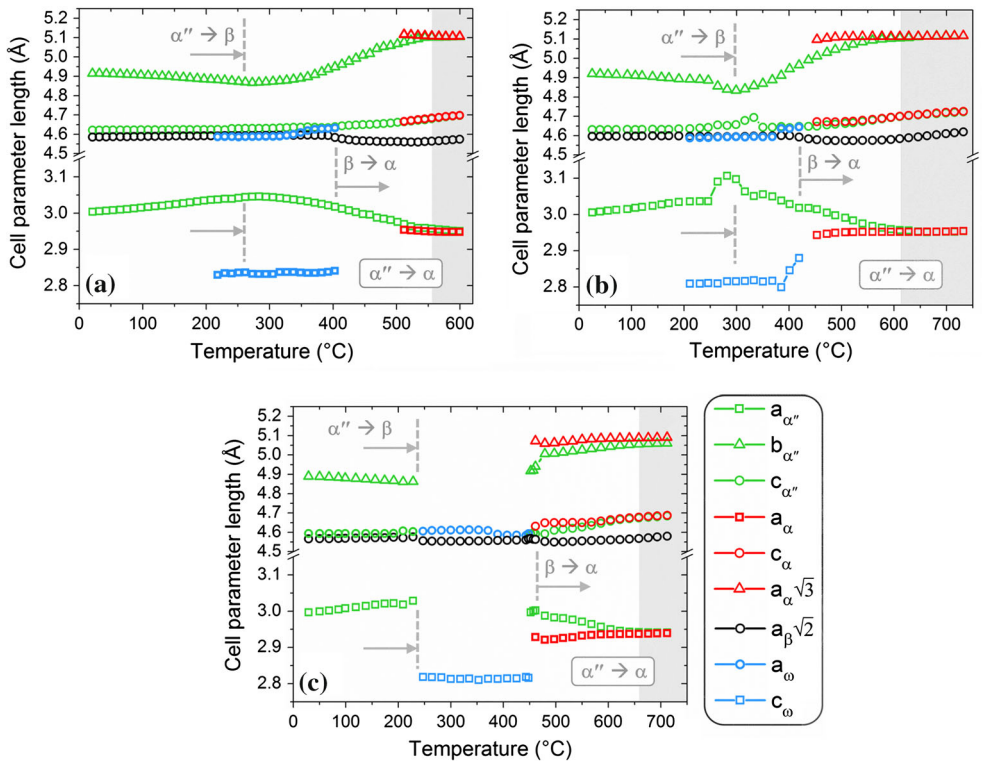

Fig. 11 Evolution of the cell parameters and of the crystallographic relationships between phases as a function of temperature during continuous heating: **a** 5 °C min^{-1}, **b** 20 °C min^{-1}, and **c** 50 °C min^{-1}

and β. This indicates that the athermal α″ → β transformation is controlled by lattice strains between these phases [6]. In the initial microstructure the three principal strains between α″ and β generated by the β → α″ transformation during quenching can be calculated as presented in [43]:

$$\epsilon_1 = \left(a_{\alpha''} - a_{\beta}\right)/a_{\beta} \quad (1)$$

$$\epsilon_2 = \left(b_{\alpha''} - \sqrt{2}a_{\beta}\right)/\sqrt{2}a_{\beta} \quad (2)$$

$$\epsilon_3 = \left(c_{\alpha''} - \sqrt{2}a_{\beta}\right)/\sqrt{2}a_{\beta} \quad (3)$$

Slight variations are obtained at RT considering all initial states: $\varepsilon_1 = -(7.1–7.5)$ %, $\varepsilon_2 = +(7.0–7.1)$ %, $\varepsilon_3 = +(0.6–0.8)$ %. These values are close to those presented for this alloy in similar conditions [6] and for a quenched β-metastable Ti–25Nb wt% alloy [47]. On the other hand, at the end of the athermal α″ → β reversion (dashed grey lines in Fig. 11) $\varepsilon_1 \sim -6.3$ %, $\varepsilon_2 \sim 6$ %, $\varepsilon_3 \sim 0.8$ % and $\varepsilon_1 \sim -4.7$ %, $\varepsilon_2 \sim 5.2$ %, $\varepsilon_3 \sim 1.4$ % for the 5 and 20 °C min^{-1} conditions, respectively, reveal a relaxation of ε_1 and ε_2 (a slight increase of ε_3 is also observed for 20 °C min^{-1}). The evolution of strain magnitudes as the heating rate increases presents similar values to those observed in Ti–Nb alloys by increasing the solute content from ~25 to 32 wt% [47].

A continuous increase of the *y*-coordinate was obtained during heating until a maximum value is reached at the end of the athermal α″ → β reversion. These maximums are 0.194 and 0.198 for the 5 and 20 °C min^{-1} conditions, respectively, and, therefore, tend to be closer to the ones required to generate a bcc structure ($y = 1/4$).

Table 4 summarizes the temperature spans of the phase transformations shown in Fig. 10 for each heating rate, and the corresponding temperature ranges obtained for the DSC peaks (Fig. 2). It must be pointed out that the direction of the reaction (exo- or endothermic) indicated in Table 4 only refers to the dominating process and does not exclude the possibility that an overlapping of several reactions takes place simultaneously. The α″ → β reversion starts in the range of 170–200 °C and finishes between 260 and 315 °C. These values are close to the ones reported in [6] for the same alloy. The difference in the starting temperature and the temperature ranges during which the phase transformation takes place may be due to the different initial strain conditions ε_1, ε_2, and ε_3 generated during water quenching of the samples.

Formation of ω

The formation of the ω phase starts simultaneously with the athermal α″ → β reversion for all heating rates (Fig. 10). This leads to an overlapping of an endothermal (α″ → β) and an exothermal (ω formation) phase transformation in the DSC signal that results in the differences between the finish temperatures of the α″ → β transformation obtained by DSC and HEXRD (peak 1 in Table 4). For the β → ω transformation, both methods present similar temperature spans which increase with heating rate. Figure 10 shows that ω reaches maximum volume fractions of 22, 5, and 80 vol% for the 5,

Table 4 Phase transformations suggested for the DSC reaction peaks and the quantitative HEXRD phase analysis for the 5, 20 and 50 °C min^{-1} heating rates

Heating rate (°C min^{-1})	DSC			HEXRD	
	Peak	Dominating process	Temperature range (°C)	Suggested phase transformations	Temperature range (°C)
5	1	Endothermic	185–220	$\alpha'' \rightarrow \beta$	200–260
20			180–233	$\alpha'' \rightarrow \beta$	170–315
50			195–248	$\alpha'' \rightarrow \beta$	175–265
5	2	Exothermic	220–308	$\beta \rightarrow \omega$; $\beta \rightarrow \alpha''_{lean}$	218–305
20			233–335	$\beta \rightarrow \omega$	230–333
50			248–364	$\beta \rightarrow \omega$; $\alpha'' \rightarrow \omega$	247–370
5	3	Endothermic	308–380	$\omega \rightarrow \beta$; $\beta \rightarrow \alpha''_{lean}$	305–400
20			335–416	$\beta \rightarrow \alpha''_{lean}$; $\omega \rightarrow \alpha''_{iso}$	333–420
50			364–454	$\omega \rightarrow \beta$	370–450
5	4	Exothermic	380–394	$\omega \rightarrow \alpha''_{iso}$	400–415
			415–435	$\beta \rightarrow \alpha$	415–425
20			416–450	$\beta \rightarrow \alpha$	420–472
50			454–480	$\omega \rightarrow \alpha''_{iso}$; $\beta \rightarrow \alpha$	450–497
5	5	Endothermic	435–526	$\alpha''_{lean/iso} \rightarrow \beta$	425–522
20			450–550	$\alpha''_{lean/iso} \rightarrow \beta$	472–540
50			480–592	$\alpha''_{iso} \rightarrow \beta$	497–586
5	6	Exothermic	526–570	$\alpha''_{lean/iso} \rightarrow \alpha$	522–555
20			550–610	$\alpha''_{lean/iso} \rightarrow \alpha$	540–610
50			592–657	$\alpha''_{iso} \rightarrow \alpha$	586–658
5	7	Endothermic	570–814	$\alpha \rightarrow \beta$	*
20			610–815	$\alpha \rightarrow \beta$	610–812
50			657–815	$\alpha \rightarrow \beta$	658–818

* Experiment stopped at 600 °C

20, and 50 °C min^{-1} heating rates, respectively. The considerably large ω volume fraction obtained for 50 °C min^{-1} is comparable with the ones reported (80–90 vol%) for other metastable β titanium alloys with similar content of β stabilizers (Ti–23Nb, Ti–10V, Ti–11Mo, Ti–8Mn, and Ti–6.8Mo–4.5Fe–1.5Al wt%) [36, 46, 48, 49].

The lower maximum ω volume fraction observed comparing 5 and 20 °C min^{-1}, and the subsequent increase comparing 20 and 50 °C min^{-1}, can be understood taking into account that two different mechanisms, depending on the heating rate, are responsible for the precipitation of ω. Thus, at 5 and 20 °C min^{-1} ω precipitates by diffusion at ~200 °C (Fig. 10a, b) at solute depleted regions of β [30, 50]. Diffusion-driven element partitioning in which alloying elements are rejected from ω particles is responsible for further growing of this phase as it has been shown experimentally in other β-metastable alloys [9, 51]. The connection between ω and β is corroborated in Fig. 11a, b by the crystallographic relationship between ω and β [46], i.e., $a_\omega = a_\beta\sqrt{2}$, for the 5 and 20 °C min^{-1} at the onset of ω precipitation, indicating that ω grows from β crystals. On the other hand, at 50 °C min^{-1} heating rate (Fig. 11c) the a_ω cell parameter starts with the last values obtained for $c_{\alpha''}$ before the athermal $\alpha'' \rightarrow \beta$ reversion. However, the ω reflections start to be resolvable by diffraction after the $\alpha'' \rightarrow \beta$ reversion (Fig. 8b). This suggests that ω forms at former α″ sites for 50 °C min^{-1}. A similar correlation was also observed in pure titanium deformed under high pressures for a γ phase with the same orthorhombic symmetry as α″ [52, 53]. Further evidences of the formation of ω from α″ are reported in [35, 54, 55] for quenched metastable β titanium alloys. Therefore, the formation of ω at 50 °C min^{-1} may be induced during the last stages of the athermal $\alpha'' \rightarrow \beta$ reversion by the complete and sudden reshearing of lattice strains shown experimentally in other metastable β alloys [9, 51]. Furthermore, the α″ phase is retained during heating for lower heating rates as described below, which may prevent the formation of high volume fraction of ω.

Stabilization of α″

The volume fraction of α″ for the 5 °C min^{-1} condition slowly increases as the temperature increases above the end of the athermal $\alpha'' \rightarrow \beta$ reversion (~260 °C, see Table 4) up to ~400 °C (Fig. 10a). On the other hand, for the

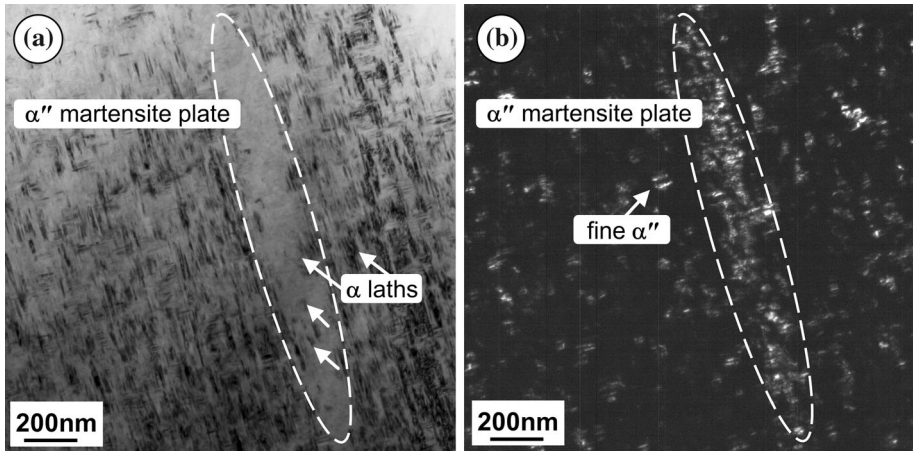

Fig. 12 TEM of the 20 °C min^{-1} condition heated up to 540 °C and subsequently water quenched: **a** bright field image where an α″ martensite plate surrounded by a non-uniform distribution of fine α laths in the metastable β matrix can be observed, and **b** dark field image using the $(1\bar{1}\bar{1})$ α″ reflection showing fine α″ in the metastable β matrix

20 °C min^{-1} condition the increase of the volume fraction of α″ is steeper until the same content (~45 vol%) as for 5 °C min^{-1} is achieved at 420 °C (Fig. 10b). These changes are directly related to the evolution of the cell parameters of α″ (Fig. 11a, b). Here, the 20 °C min^{-1} condition presents a steeper increase and decrease of the $b_{\alpha''}$ and $a_{\alpha''}$ cell parameters, respectively, in comparison with 5 °C min^{-1}. At 400 °C, $b_{\alpha''}$ and $a_{\alpha''}$ coincide at both heating rates. The changes in the cell parameters are an indication of diffusion-driven element partitioning between phases and may be related to a transfer of β-stabilizer atoms (Fe and V) from α″ into β as it has been suggested for alloys with similar $[Mo]_{eq}$ concentrations [6, 56]. For this reason the phase observed within this temperature range is called α''_{lean} hereafter. Therefore, the larger increase in the volume fraction of α''_{lean} observed in the 20 °C min^{-1} condition up to 400 °C is a diffusive process. Simultaneously, the remaining β phase is chemically stabilized. As a result, the diffusionless α″ to β reversion caused by thermal stresses is partly suppressed for lower heating rates due to element partitioning. α''_{lean} phase is retained for lower heating rates, which reduces the maximum attained volume fraction of ω phase.

In the same temperature region as described above, the volume fraction of ω reaches a maximum and subsequently decreases for all heating rates. At 5 °C min^{-1}, this decrease follows practically the same trend as the increase in β (Fig. 10a) suggesting an ω → β transformation. The same trend is observed for 50 °C min^{-1} (Fig. 10c). This transformation is not evident for the 20 °C min^{-1} owing to the low concentration of ω and the previously explained β-stabilization. The changes for the 50 °C min^{-1} condition are also evidenced by a decrease of a_{ω} at ~370 °C (Fig. 11c). Furthermore, as the temperature increases, a_{ω} shifts to the position of $c_{\alpha''}$ in the ranges 340–380 °C, 370–400 °C, and 443–448 °C for 5, 20, and 50 °C min^{-1}, respectively (Fig. 11a) to c). The same correlation of cell parameters was described in "Formation of ω" section and in [52, 53]. This, together with the continuous shift of {002}ω reflections to a position close to that of {130}α″ (see Online Resources 1, 2, and 3) also points to the formation of α″ from ω. A prior work [35] suggested that band-like products of ω transform into α″ within martensite plates during holding at ~450 °C for a Ti–8Mo wt% alloy. Furthermore, formation of α″ during isothermal decomposition of the β-metastable phase has been reported at moderate temperatures (420–600 °C) for several alloys (Ti-17 [12], Ti-5553 [57], VT-22, and TIMETAL-LCB [8] with $[Mo]_{eq}$ = ~9, 12, 11, 18 wt%, respectively). This product has been referred to as isothermal α″ since its formation was observed during heat treatments at constant temperature [8, 12, 57, 58]. The same nomenclature is used here (α''_{iso}), but it must be taken into account that this serves only to distinguish between two different formation mechanisms of this orthorhombic phase: α''_{lean} forms from β, while α''_{iso} forms from ω. It is important to note that the *y*-coordinate of α''_{iso} (as determined at 50 °C min^{-1}) is slightly different (0.181) from the one obtained by the combination of α''_{iso} and α''_{lean} (5 and 20 °C min^{-1}) suggesting compositional variations between them.

The transformations explained in this section correlate with the endothermic and exothermic peaks 3 and 4 of the DSC as shown in Table 4. Due to the higher magnitude of the β → α''_{lean} transformation compared to the ω → α''_{iso} transformation in the 20 °C min^{-1} condition, the overlapping of both processes is observed as a single endothermic peak in the DSC curve.

Formation of α

Transformation from the β phase

Reflections close to those expected for α are visible for the 50 °C min^{-1} condition from ~425 °C (Fig. 8).

Furthermore, evidences of α reflections are marked by arrows in Fig. 9b, c for the 20 and 50 °C min^{-1} conditions, respectively. Also, Figs. 10 and 11 show that all heating rates undergo a decrease in the volume fraction of β and in the β cell parameter above ~390, ~400, and ~450 °C for the 5, 20, and 50 °C min^{-1} conditions, respectively. The presence of α at 400 °C has been reported during isothermal aging of Ti–10V–2Fe–3Al [59, 60]. Figure 2 and Table 4 show that the β → α transformation is reflected in the exothermic reaction number 4. At 5 °C min^{-1} it takes place as a single reaction between 415 and 435 °C, at 20 °C min^{-1} occurs between 416 and 450 °C, while at 50 °C min^{-1} overlaps with the ω → α''_{iso} transformation (454–480 °C) as it has also been suggested for a Ti-LCB metastable β alloy [14]. At higher temperatures, an increase of the β content of ~10 vol% is observed for all conditions suggesting that an additional $\alpha''_{lean/iso} \rightarrow \beta$ transformation takes place. The temperature ranges of this transformation fit with the endothermic peak 5 of the DSC (Table 4).

Evolution of α″

Figure 11 shows a progressive evolution of $b_{\alpha''}$, $c_{\alpha''}$, and $a_{\alpha''}$ towards $a_\alpha\sqrt{3}$, c_α and a_α, respectively, until they coincide above temperatures between 555 and 660 °C. This transformation is associated with the exothermic peak number 6 of the DSC (Fig. 2; Table 4). This indicates a gradual transformation of the orthorhombic $\alpha''_{lean/iso}$ into α. The formation of α from α″ has been proposed in [61], where homogeneous α precipitates were observed by TEM inside the stacking faults of martensitic α″ plates for quenched samples of a TC21 alloy aged at 500 °C. On the other hand, α was observed between α''_{iso} for quenched samples of TI-METAL-LCB aged at 538 °C [8]. Moreover, the $\alpha''_{lean} \rightarrow \alpha$ transformation was also suggested in the basis of dilatometry tests for the current alloy [6]. Figure 11 shows a direct evidence of this phase transformation. Figure 12a shows a TEM bright field image of an α″ martensite plate surrounded by a non-uniform distribution of fine α laths within the metastable β matrix for a 20 °C min^{-1} sample quenched from 540 °C. Moreover, α laths marked by arrows have formed within the martensite plate. The dark field TEM image in Fig. 12b shows that particles of α″ (bright regions) are also found dispersed in the metastable β matrix. At this temperature α″ already presents a symmetry close to hcp (Fig. 11b) and, therefore, these particles may correspond to particles undergoing the α″ → α transformation. As a consequence, the formation of α from α″ can occur by two different paths:

(1) Formation of α from the α″ martensite plates, which corresponds to $\alpha''_{lean} \rightarrow \alpha$ transformation.

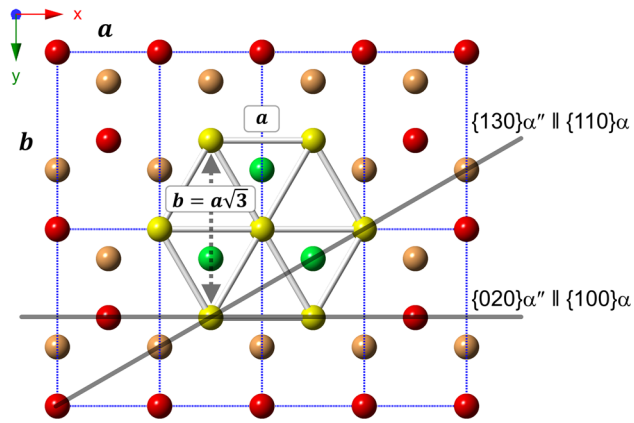

Fig. 13 Representation of the lattice correspondence observed between the α″ and α phases. The atoms in the basal planes of α and α″ are indicated by *yellow* and *red spheres*, respectively. The atoms in the consecutive central plane of the α and α″ lattices are depicted by *green* and *orange spheres*, respectively (Color figure online)

(2) Formation of α from α''_{iso} particles distributed within the metastable β matrix previously formed from the ω → α''_{iso} phase transformation.

The lattice correspondence between α″ and α can be established from the shift of α″ reflections to the positions of α, as shown in Fig. 7, and the correspondence between the evolution of the cell parameters shown in Fig. 11. These relationships are established as follows: {130}α″ ∥ {110}α and {020}α″ ∥ {100}α. The hcp and orthorhombic structures are shown together in Fig. 13 as a projection along the *c* axis (a 3D animation is provided in Online Resource 4).

Dissolution of α

The last endothermic peak of the DSC (number 7) corresponds to the transformation of α into β (Fig. 2; Table 4). A peak shift to higher temperatures can be observed as a function of the heating rate. This process finishes at temperatures close to the equilibrium β-transus temperature (800 °C) [20].

Conclusions

The phase transformation kinetics of the β quenched Ti–10V–2Fe–3Al alloy has been studied by in situ HEXRD and DSC as a function of heating rate. The following conclusions can be drawn from the investigations:

- A fast athermal α″ → β reversion is observed at ~200 °C for all heating rates (5, 20, and 50 °C min^{-1}). The magnitude of this athermal α″ → β reversion increases with the heating rate

leading to a complete transformation of α'' into β for the 50 °C min^{-1} condition.

- Two different origins for the formation of ω are identified depending on the heating rate: at 5 and 20 °C min^{-1} ω grows from β crystals by a diffusion controlled mechanism, while at 50 °C min^{-1} ω forms from the orthorhombic α'' phase. The latter may be induced during the last stages of the $\alpha'' \rightarrow \beta$ reversion by the complete and sudden reshearing of lattice strains.
- Two different mechanisms of formation of α'' are observed at temperatures above the end of the $\alpha'' \rightarrow \beta$ reversion: on the one hand, α''_{lean} grows to stabilize the excess of β formed during the martensite reversion (5 and 20 °C min^{-1}), while at higher temperatures α''_{iso} forms from ω as reflected by the corresponding evolution of the cell parameters.
- At moderate temperatures (420–650 °C) α forms through three different paths:

  (a) Formation of α from the α'' martensite plates, which corresponds to $\alpha''_{lean} \rightarrow \alpha$ transformation.
  (b) Formation of α from α''_{iso} particles distributed within the metastable β matrix previously formed from the $\omega \rightarrow \alpha''_{iso}$ phase transformation.
  (c) Formation of α from the β phase ($\beta \rightarrow \alpha$).

- In situ HEXRD has been applied to follow univocally the evolution of the single Bragg reflections of each phase allowing a complete determination of the phase transformation sequence in the Ti–10V–2Fe–3Al metastable β alloy as a function of heating rate.

Acknowledgements The authors acknowledge the COMET-Program of the Austrian Research Promotion Agency (FFG) and the Province of Upper Austria (LOÖ), Grant No. 820492 for financial support. The European Synchrotron Radiation Facility (ESRF) and the Deutsches Elektronen-Synchrotron (DESY) are acknowledged for the provision of synchrotron radiation facilities in the framework of the MA1268 and I-20100329 EC proposals, respectively. The University Service for Transmission Electron Microscopy (USTEM) of the Vienna University of Technology is acknowledged for the provision of the transmission electronic microscope. Böhler Schmiedetechnik GmbH & Co KG is also acknowledged for the provision materials. The authors would like to thank Dr. A. Rhys Williams for proof-reading the manuscript.

References

1. Banerjee D, Williams JC (2013) Perspectives on titanium science and technology. Acta Mater 61:844–879
2. Boyer RR, Briggs RD (2005) The use of titanium alloys in the aerospace industry. J Mater Eng Perform 14:681–685
3. Maeshima T, Nishida M (2004) Shape memory and mechanical properties of biomedical Ti–Sc–Mo alloys. Mater Trans 45:1101–1105
4. Duerig TW, Williams JC (1984) Microstructure and properties of beta titanium alloys. In: Boyer RR, Rosenberg HW (eds) Beta titanium alloys in the 1980's. The Metallurgical Society of AIME, Atlanta, pp 16–69
5. Miyazaki S, Sachdeva RL (2009) Shape memory effect and superelasticity in Ti–Ni alloys. In: Yoneyama T, Miyazaki S (eds) Shape memory alloys for biomedical applications. Woodhead, Cambridge, pp 3–18
6. Duerig TW, Albrecht J, Richter D, Fischer P (1982) Formation and reversion of stress induced martensite in Ti–10V–2Fe–3Al. Acta Metall 30:2161–2172
7. Ohmori Y, Ogo T, Nakai K, Kobayashi S (2001) Effects of ω-phase precipitation on $\beta \rightarrow \alpha$, α'' transformations in a metastable β titanium alloy. Mater Sci Eng A 312:182–188
8. Ivasishin OM, Markovsky PE, Semiatin SL, Ward CH (2005) Aging of coarse- and fine-grained β titanium alloys. Mater Sci Eng A 405:296–305
9. Nag S, Banerjee R, Srinivasan R, Hwang JY, Harper M, Fraser HL (2009) ω-Assisted nucleation and growth of α precipitates in the Ti–5Al–5Mo–5V–3Cr–0.5Fe β titanium alloy. Acta Mater 57:2136–2147
10. Bein S, Béchet J (1996) Phase transformation kinetics and mechanisms in titanium alloys Ti-6.2.4.6, β-CEZ and Ti-10.2.3. J Phys IV 6:99–108
11. Malinov S, Sha W, Markovsky P (2003) Experimental study and computer modeling of the $\beta \rightarrow \alpha+\beta$ phase transformation in β21s alloy at isothermal conditions. J Alloys Compd 348:110–118
12. Bruneseaux F, Geandier G, Gautier E, Appolaire B, Dehmas M, Boulet P (2007) In situ characterization of the transformation sequences of Ti17 alloy by high energy X-ray diffraction: Influence of the thermal path. In: Niinomi M, Akiyama S, Hagiwara M, Ikeda M, Maruyama K (eds) Ti-2007 science and technology. The Japan Institute of Metals, Sendai, pp 563–566
13. Contrepois Q, Carton M, Lecomte-Beckers J (2011) Characterization of the β phase decomposition in Ti–5Al–5Mo–5V–3Cr at slow heating rates. Open J Met 1:1–11
14. Carton M, Jacques P, Clément N, Lecomte-Beckers J (2007) Study of transformations and microstructural modifications in Ti-LCB and Ti-555 alloys using differential scanning calorimetry. In: Niinomi M, Akiyama S, Hagiwara M, Ikeda M, Maruyama K (eds) Ti-2007 science and technology. The Japan Institute of Metals, Sendai, pp 491–494
15. Liss KD, Bartels A, Schreyer A, Clemens H (2003) High-energy X-rays: a tool for advanced bulk investigations in materials science and physics. Texture Microstruct 35:219–252
16. Aeby-Gautier E, Bruneseaux F, Teixeira J, Appolaire B, Geandier G, Denis S (2007) Microstructural formation in Ti alloys: in-situ characterization of phase transformation kinetics. JOM 59:54–58
17. Jones NG, Dashwood RJ, Jackson M, Dye D (2009) β phase decomposition in Ti–5Al–5Mo–5V–3Cr. Acta Mater 57:3830–3839
18. Wollmann M, Kiese J, Wagner L (2011) Properties and applications of titanium alloys in transport. In: Zhou L, Chang H, Lu Y, Xu D (eds) Ti-2011. Science Press Beijing, Beijing, pp 837–844
19. Eylon D, Vassel A, Combres Y, Boyer RR, Bania PJ, Schutz RW (1994) Issues in the development of beta titanium alloys. JOM 46:14–15
20. Boyer R, Welsch G, Collings EW (1994) Material properties handbook: titanium alloys, 4th edn. ASM International, Ohio
21. Lin W, Dalmazzone D, Fürst W, Delahaye A, Fournaison L, Clain P (2013) Acurate DSC measurement of the phase transition temperature in the TBPB–water system. J Chem Thermodyn 61:132–137
22. Pompe G, Schulze U, Hu J, Pionteck J, Höhne GWH (1999) Separation of glass transition and melting polyethylene/poly (butyl-methacrylate-co-methyl-methacrylate) interpenetrating

polymer networks in TMDSC and DSC curves. Thermochim Acta 337:179–186
23. ID15 - High Energy Scattering Beamline, ESRF (1999). http://www.esrf.eu/UsersAndScience/Experiments/StructMaterials/ID15. Accessed 09 July 2014
24. P07 - The High Energy Materials Science Beamline, DESY (2010). http://photon-science.desy.de/facilities/petra_iii/beamlines/p07_high_energy_materials_science/index_eng.html. Accessed 09 July 2014
25. Staron P, Fischer T, Lippmann T, Stark A, Daneshpour S, Schnubel D, Uhlmann E, Gerstenberger R, Camin B, Reimers W, Eidenberger E, Clemens H, Huber N, Schreyer A (2011) In situ experiments with synchrotron high-energy X-rays and neutrons. Adv Eng Mater 13:658–663
26. Hammersley A, Svensson SO, Thompson A (1994) Calibration and correction of spatial distortions in 2D detector systems. Nucl Instrum Methods Phys Res A 346:312–321
27. Abramoff MD, Magalhães PJ, Ram SJ (2004) Image processing with imageJ. Biophoton Int 11:36–41
28. Lutterotti L, Matthies S, Wenk HR, Schultz AJ, Richardson J (1997) Combined texture and structure analysis of deformed limestone from time-of-flight neutron diffraction spectra. J Appl Phys 81:594–600
29. Cai MH, Lee CY, Kang S, Lee YK (2011) Fine-grained structure fabricated by strain-induced martensite and its reverse transformations in a metastable β titanium alloy. Scripta Mater 64:1098–1101
30. Banerjee S, Mukhopadhyay P (2007) Phase transformations: examples from titanium and zirconium alloys, 1st edn. Elsevier, Oxford
31. Willams JC, Fontaine D, Paton NE (1973) The ω-phase as an example of an unusual shear transformation. Metall Trans 4:2701–2708
32. Sass SL (1972) The structure and decomposition of Zr and Ti B.C.C. solid solutions. J Less Common Met 28:157–173
33. Li SJ, Cui TC, Hao YL, Yang R (2008) Fatigue properties of a metastable β-type titanium alloy with reversible phase transformation. Acta Biomater 4:305–317
34. Dutta J, Ananthakrishna G, Banerjee S (2012) On the athermal nature of the β to ω transformation. Acta Mater 60:556–564
35. Mantani Y, Takemoto Y, Hida M, Sakakibara A, Tajima M (2004) Phase transformation of a α″ martensite structure by aging in Ti-8 mass%Mo alloy. Mater Trans 45:1629–1634
36. Popov AA, Illarionov AG, Grib SV, Elkina AO (2011) Formation conditions of omega phase in the titanium alloys after quenching. In: Zhou L, Chang H, Lu Y, Xu D (eds) Ti-2011. Science Press Beijing, Beijing, pp 694–697
37. Bönisch M, Calin M, Waitz T, Panigrahi A, Zehetbauer M, Gebert A, Skrotzki W, Eckert J (2013) Thermal stability and phase transformations of martensitic Ti–Nb alloys. Sci Technol Adv Mater 14:1–9
38. Liss KD, Stark A, Bartels A, Clemens H, Buslaps T, Phelan D, Yeoh LA (2008) Directional atomic rearrangements during transformations between the α- and γ-phases in titanium aluminides. Adv Eng Mater 10:389–392
39. Ramsteiner IB, Shchyglo O, Mezger M, Udyansky A, Bugaev V, Schöder S, Reichert H, Dosch H (2008) Omega-like diffuse X-ray scattering in Ti–V caused by static lattice distortions. Acta Mater 56:1298–1305
40. Settefrati A, Dehmas M, Geandier G, Denand B, Aeby-Gautier E, Appolaire B, Khelifati G, Delfosse J (2011) Precipitation sequences in beta metastable phase of Ti-5553 alloy during ageing. In: Zhou L, Chang H, Lu Y, Xu D (eds) Ti-2011. Science Press Beijing, Beijing, pp 468–472
41. Basak CB, Neogy S, Srivastava D, Dey GK, Banerjee S (2011) Disordered bcc γ-phase to δ-phase transformation in Zr-rich U-Zr alloy. Philos Mag 91:3290–3306
42. Banerjee D, Muraleedharan K, Strudel JL (1998) Substructure in titanium alloy martensite. Philos Mag A 77:299–323
43. Obbard EG, Hao YL, Talling RJ, Li SJ, Zhang YW, Dye D, Yang R (2011) The effect of oxygen on α″ martensite and superelasticity in Ti–24Nb–4Zr–8Sn. Acta Mater 59:112–125
44. Banumathy S, Mandal RK, Singh AK (2009) Structure of orthorhombic martensitic phase in binary Ti–Nb alloys. J Appl Phys 106:093518.1–093518.6
45. Brown ARG, Clark D, Eastabrook J, Jepson KS (1964) The titanium–niobium system. Nature 201:914–915
46. Aurelio G, Fernández-Guillermet A, Cuello GJ, Campo J (2002) Metastable phases in the Ti–V system: part I. Neutron diffraction study and assessment of structural properties. Metall Mater Trans A 33:1307–1317
47. Kim HY, Ikehara Y, Kim JI, Hosoda H, Miyazaki S (2006) Martensitic transformation, shape memory effect and superelasticity of Ti–Nb binary alloys. Acta Mater 54:2419–2429
48. Williams JC, Hickman BS, Marcus HL (1971) The effect of omega phase on the mechanical properties of titanium alloys. Metall Trans 2:1913–1919
49. Šmilauerová J, Janeček M, Harcuba P, Stráský J (2013) Aging study of TIMETAL LCB titanium alloy. Proc. Met.. http://www.metal2014.com/files/proceedings/12/reports/1536.pdf. Accessed 09 July 2014
50. Hickman BS (1969) The formation of omega phase in titanium and zirconium alloys: a review. J Mater Sci 4:554–563. doi:10.1007/BF00550217
51. Devaraj A, Nag S, Srinivasan R, Williams REA, Banerjee S, Banerjee R, Fraser HL (2012) Experimental evidence of concurrent compositional and structural instabilities leading to ω precipitation in titanium–molybdenum alloys. Acta Mater 60:596–609
52. Akahama Y, Kawamura H, Bihan TL (2001) New δ (distorted-bcc) titanium to 220 GPa. Phys Rev Lett 87:275503.1–275503.4
53. Vohra YK, Spencer PT (2001) Novel gamma-phase of titanium metal at megabar pressures. Phys Rev Lett 86:3068–3071
54. Duerig TW, Middleton RM, Terlinde GT, Williams JC (1980) Stress assisted transformation in Ti–10V–2Fe–3Al. In: Kimura H, Izuma O (eds) Titanium '80 science and technology. Metallurgical Society of AIME, Kyoto, pp 1503–1508
55. Davis R, Flower HM, West DRF (1979) Martensitic transformations in Ti–Mo alloys. J Mater Sci 14:712–722. doi:10.1007/BF00772735
56. Bagariatskii IA, Nosova GI, Tagunova TV (1958) Factors in the formation of metastable phases in titanium-base alloys. Sov Phys Dokl 3:1014–1018
57. Settefrati A, Aeby-Gautier E, Appolaire B, Dehmas M, Geandier G, Khelifati G (2013) Low temperature transformation in the β-metastable Ti-5553 alloy. Mater Sci Forum 738–739: 97–102
58. Malinov S, Sha W, Guo Z, Tang CC, Long AE (2002) Synchrotron X-ray diffraction study of the phase transformations in titanium alloys. Mater Charact 48:279–295
59. Duerig TW, Terlinde GT, Williams JC (1980) Phase transformations and tensile properties of Ti–10V–2Fe–3Al. Metall Trans A 11:1987–1998
60. Ohmori Y, Natsui H, Nakai K, Ohtsubo H (1998) Effects of ω phase formation on decomposition of α″/β duplex phase structure in a metastable β Ti alloy. Mater Trans JIM 39:40–48
61. Tang B, Kou HC, Wang YH, Zhu ZS, Zhang FS, Li JS (2012) Kinetics of orthorhombic martensite decomposition in TC21 alloy under isothermal conditions. J Mater Sci 47:521–529. doi:10.1007/s10853-011-5829-5

Journal of Alloys and Compounds 626 (2015) 330–339

Contents lists available at ScienceDirect

Journal of Alloys and Compounds

journal homepage: www.elsevier.com/locate/jalcom

Role of element partitioning on the α–β phase transformation kinetics of a bi-modal Ti–6Al–6V–2Sn alloy during continuous heating

Pere Barriobero-Vila [a,*], Guillermo Requena [a], Thomas Buslaps [b], Matthias Alfeld [c], Ulrike Boesenberg [c]

[a] Institute of Materials Science and Technology, Vienna University of Technology, Karlsplatz 13/308, A-1040 Vienna, Austria
[b] ID15, European Synchrotron Radiation Facility, Rue J. Horowitz, F-38042 Grenoble, France
[c] Deutsches Elektronen-Synchrotron (DESY), Notkestrasse 85, D-22607 Hamburg, Germany

ARTICLE INFO

Article history:
Received 27 July 2014
Received in revised form 18 November 2014
Accepted 19 November 2014
Available online 6 December 2014

Keywords:
Titanium alloys
High-energy X-ray diffraction
Micro X-ray fluorescence
Phase transformation kinetics
Element partitioning

ABSTRACT

The role of element partitioning on the phase transformation kinetics of a bi-modal α + β Ti–6Al–6V–2Sn alloy is studied experimentally as a function of heating rate combining quantitative phase analysis with elemental analysis. The evolution of phase volume fractions and lattice parameters is investigated by in situ high energy synchrotron X-ray diffraction and conventional metallographic analysis. Synchrotron micro X-ray fluorescence and energy dispersive X-ray spectroscopy are applied to trace microstructural distribution of alloying elements during heating. The linear increase of the lattice parameters observed for all conditions at the beginning of the heating is associated to lattice thermal expansion. Thereafter, at intermediate temperatures, the alloy undergoes a β to α transformation for low heating rates. Element partitioning results in an enrichment of α and β by their respective stabilizing elements and a consequent nonlinear variation of the lattice parameters. As the temperature increases, α transforms into β up to the β-transus temperature. Microstructural evidences of the role of V during phase transformation are presented. Moreover, nonlinear variations of the β lattice parameter are related to the role of alloying elements on the different stages of element partitioning. The analysis of phase transformation kinetics combining laboratory and synchrotron-based techniques provides an advance in the current knowledge of the phase transformation kinetics of the Ti–6Al–6V–2Sn alloy that can help to develop new theoretical models and, consequently, knowledge-based thermal treatment optimization.

1. Introduction

α + β titanium alloys are used mainly in a wide range of components for the aerospace industry due to their high specific strength, fatigue resistance and excellent corrosion resistance [1–5]. Despite the high cost of these alloys, their properties have also promoted their use in a variety of applications in other fields such as automotive, energy, power generation, biomedical and sport industries [3–5]. Pioneering initiatives have been presented to reduce component costs derived from alloy manufacturing [6–9]. The mechanical properties of α + β alloys are highly affected by microstructural characteristics, which can be controlled by thermal and thermomechanical treatments [1–3]. Therefore, a correct understanding of the α → β phase transformation kinetics is required for optimization of the functional design of these alloys.

Significant efforts have been focused on the development of modelling tools for microstructure prediction to improve alloy design, lead-time and cost savings [10–13]. These tools require reliable experimental data for validation. Although some advances have been achieved, e.g. [14,15], thermodynamic analyses are still mostly confined to phase equilibria, where the role of kinetic variables (e.g. heating rate) is not considered. Consequently, the diffusion processes that control the α → β phase transformation kinetics during thermal treatment have been generally explained in the basis of theoretical equilibrium concentrations of alloying elements between phases, e.g. [16–19]. However, these investigations do not provide a complete understanding of critical aspects like the influence of element partitioning on the phase transformation kinetics as well as on the evolution of the lattice structure of phases. Nowadays, continuous and univocal studies of phase transformation kinetics can be carried out in situ by high energy synchrotron X-ray diffraction (HEXRD) [20,21]. This bulk technique allows the determination of the evolution of phases during heat treatment with a time resolution down to ~1 s [20]. The benefits of in situ HEXRD for the study of the phase transformation kinetics

* Corresponding author. Tel.: +43 6803240923.
E-mail addresses: pere.vila@tuwien.ac.at (P. Barriobero-Vila), guillermo.requena@tuwien.ac.at (G. Requena), buslaps@esrf.fr (T. Buslaps), matthias.alfeld@desy.de (M. Alfeld), ulrike.boesenberg@desy.de (U. Boesenberg).

http://dx.doi.org/10.1016/j.jallcom.2014.11.176
0925-8388/

in titanium alloys have been reported in several occasions [16,18,21]. Moreover, local compositional variations not detectable by common electron-beam methods can be traced by sensitive synchrotron micro X-ray fluorescence (μ-XRF) [22–24].

The α + β Ti–6Al–6V–2Sn alloy (Ti-662) presents higher strength, weight saving, fracture toughness and stress corrosion resistance than Ti–6Al–4V at temperatures up to 315 °C [1,5,25]. To the best knowledge of the authors, only few works analysed the phase transformations involved in the Ti-662 alloy [25,26], while no one offers a continuous description of the α → β transformation. In the present study HEXRD and μ-XRF are combined with conventional metallographic analysis (MA) and energy dispersive X-ray spectroscopy (EDX) to study the role of element partitioning on the phase transformation kinetics of a bi-modal Ti-662 alloy as a function of heating rate. The evolution of phase volume fractions and lattice parameters is analysed in terms of element diffusion from room temperature (RT) to the β-field. The results show that the combination of these techniques provides a deeper understanding of phase transformation kinetics as well as substantial experimental data that will serve for the development of theoretical models.

2. Experimental

2.1. Material

The nominal composition of the investigated α + β titanium alloy Ti-662 is given in Table 1 [27]. The β-transus temperature, T_β, is ~945 °C [25]. The alloy was received as a commercially produced ingot of 77 mm diameter with a bi-modal microstructure. This microstructure represents the initial condition for further investigations and was obtained as follows: after casting the ingot was subjected to cogging (deformation just below the β-transus), annealing for 0.5–1 h at 885 °C with subsequent water quenching, and aging at 540 °C for 4–8 h followed by air cooling [28].

2.2. Study of phase transformation kinetics

MA and in situ HEXRD were applied to determine the phase transformation kinetics of the Ti-662 alloy. The evolution of phase volume fractions and lattice parameters were determined during continuous heating at 5, 20 and 100 K/min from RT up to 1000 °C.

2.2.1. Metallographic analysis

Frozen microstructures of the Ti-662 alloy were obtained for MA every 50 °C during heating. For this, samples of 4 × 4 × 10 mm^3 were heated up and quenched with helium upon reaching each temperature. The heat treatments were performed in vacuum atmosphere using a Bähr 805A/D dilatometer with an induction coil furnace. Thereafter, the samples were subjected to grinding and polishing using a TegraPol machine and were observed in a FEI Quanta 200 field emission gun scanning electron microscope (FEG-SEM) operated in backscattered electron mode (BSE) at 20 kV. The software ImageJ [29] was employed to segment the α and β phases in the BSE images and determine their respective area fractions. Six BSE images were analysed for each temperature. The segmentation of the 32 bit images was carried out by global grey value threshold. For this, the α and β phases were separated defining a constant cut-off grey value for each SEM micrograph. Pixels with a grey value higher than the cut-off were assigned to β, while pixels with a grey value lower than the cut-off were assigned to α. Finally, the primary and secondary α morphologies were separated by size and circularity restrictions using the tool "Analyze Particles" of the software ImageJ [29]. Moreover, it is important to note that manual segmentation is partially required to obtain a satisfactory correlation with the BSE images.

2.2.2. In situ high energy synchrotron X-ray diffraction

In situ HEXRD was carried out at the ID15B beamline of the ESRF (European Synchrotron Radiation Facility, Grenoble) [30]. Experimental parameters are summarized in Table 2. Samples of 4 × 4 × 20 mm^3 were heated up in a dynamic argon atmosphere by means of a radiant furnace [21]. The samples were kept fixed during acquisition and the temperature was controlled by a spot-welded thermocouple located next to the position of the incoming beam. Image sequences of complete Debye–Scherrer rings from the bulk of the samples were recorded in transmission mode using an image-plate detector (see Table 2). Instrumental parameters of the diffraction setup were obtained using LaB_6 powder standard. Quantitative phase analysis of the diffraction patterns, such as the evolution of phase volume fractions and lattice parameters, was carried out by the Rietveld method as implemented in the software Maud [31].

2.3. Microstructural tracking of alloying elements

μ-XRF and EDX were used to trace microstructural distribution of alloying elements at characteristic temperatures during continuous heating of the Ti-662 alloy at 5 and 100 K/min from RT up to 1000 °C. Samples with frozen microstructures were prepared as explained in Section 2.2.1. In addition to the initial state, the conditions investigated are summarized in Table 3.

2.3.1. Synchrotron micro X-ray fluorescence

μ-XRF was carried out at the Hard X-ray microprobe beamline P06 of the synchrotron source PETRA III, DESY (Deutsches Elektronen-Synchrotron, Hamburg, Germany) [32]. Experimental parameters of the setup are summarized in Table 2. Specimens with a thickness of 10 μm and a size of 4 × 4 mm^2 were obtained from the samples for metallographic analysis described in Section 2.2.1. The specimens were prepared by grinding and polishing in a Multiprep machine and were mounted on Si_3N_4 frames. They were then scanned at RT in air atmosphere using a step size of 500 nm to obtain elemental maps of Ti, V, Fe and Cu in regions of 100 × 100 μm^2. A monochromatic X-ray beam with an energy of 11.5 keV was focused by mirror optics in Kirkpatrick–Baez geometry to a spot size of 0.5 × 0.5 μm^2. The samples were aligned using an in-line optical microscope. The emitted fluorescence radiation was recorded under a take-off angle of ~5° by means of a Vortex EM SD detector. The primary radiation was only partially absorbed by the sample, but due to self-absorption effects the elemental distribution images are dominated by the surface layer. The relevant depth, contributing 80% of the recorded fluorescence intensity, is given in Table 4. It was calculated based on the fundamental parameter approach using parameters from [33]. Data analysis and mapping assembling of fluorescence spectra was carried out using the software PyMca [34]. The limits of detection under the given experimental conditions were

Table 3
Temperatures selected during continuous heating with 5 and 100 K/min at which frozen microstructures were obtained for EDX and μ-XRF experiments.

Heating rate (K/min)	Temperature (°C)	
	EDX	μ-XRF
5	400, 530	530
	740, 940	940
100	400, 590	590
	780, 940	940

Table 1
Composition of the Ti–6Al–6V–2Sn alloy [27].

Element	Al	V	Sn	Cu	Fe	O	C	N	H	Ti	$[Mo]_{eq}$
wt.%	6	6	2	0.75	0.35–1	0.20	0.05	0.04	0.015	Balance	~4
at.%	10.20	5.40	0.77	0.54	0.28–0.82	0.57	0.20	0.13	0.70	Balance	~5.7

Table 2
Experimental parameters used during HEXRD and μ-XRF experiments.

Beamline	Technique	Energy (keV)	Wavelength (Å)	Slit-aperture/spot size (μm^2)	Acquisition time (s)	Read-out time (s)	Detector
ID15B- ESRF	HEXRD	87	0.142	300 × 300	2	1	Pixium
P06-PetraIII	μ-XRF	11.5	1.078	0.5 × 0.5	0.2	–	Vortex EM SD

Table 4
Relevant depth contributing 80% of the recorded fluorescence intensity for different elements.

Fluorescence line	Line energy (keV)	Relevant depth (μm)
Ti–Kα	4.51	2.1
Ti–Kβ	4.93	2.7
V–Kα	4.95	2.7
V–Kβ	5.43	0.57
Fe–Kα	6.40	0.87
Cu–Kα	8.91	2.0

estimated per pixel and 0.2 s dwell time from the sum spectrum of a complete scan and the known composition of the bulk sample. They were found to be approximately 1900, 900, 220 and 190 ppm for Ti, V, Fe and Cu, respectively.

The α and β phases were segmented in μ-XRF maps for selected heat treatment conditions to visualize elemental distribution in each phase. The segmentation procedure was analogous to the one described in Section 2.2.1 and it was carried out selecting a cut-off grey value that resulted in the closest reproduction of the SEM micrograph of the studied region.

2.3.2. Energy dispersive X-ray spectroscopy

EDX was carried out in a FEI Quanta 200 FEG-SEM operated at 20 kV using the software EDAX Genesis Spectrum. Quantitative elemental maps of Ti, Al and V were obtained from spectra recorded with an acquisition time of 1.1 s and limited to a bulk information of $\sim 1 \times 1 \times 1.5\ \mu m^3$ in regions of $125 \times 100\ \mu m^2$. The EDX spectra were quantified using the software EDAX Genesis Spectrum which considers ZAF corrections for evaluation [35]. Mean element concentrations in primary α grains in the scanned regions were obtained by segmentation of the quantitative EDX maps using a procedure analogous to the one described in Section 2.3.1.

3. Results

3.1. Initial microstructure

Fig. 1 shows the initial microstructure of the Ti-662 alloy. It presents a bi-modal microstructure composed by primary α grains and secondary α lamellae (dark grey) distributed in a β matrix (light grey). The primary α grains present equiaxed morphology with a mean diameter of ~10 μm. On the other hand, secondary α is distributed as colonies of lamellae embedded in the β matrix between primary α grains. The inset in Fig. 1 shows that the α lamellae have lengths of up to ~5 μm. Fig. 2 shows an example of the segmentation of primary α (Fig. 2b) and secondary α (Fig. 2c) for the initial condition of the alloy (Fig. 2a). The primary α grains are readily segmented, while some small secondary α lamellae are lost during segmentation. The initial area fraction of primary α, secondary α and β obtained by MA is 73 ± 2.5%, 2 ± 0.5% and 25 ± 3%, respectively. This is in agreement with the volume fractions of 74 and 26 vol.% obtained for α and β, respectively, according to the equilibrium phase diagram [4].

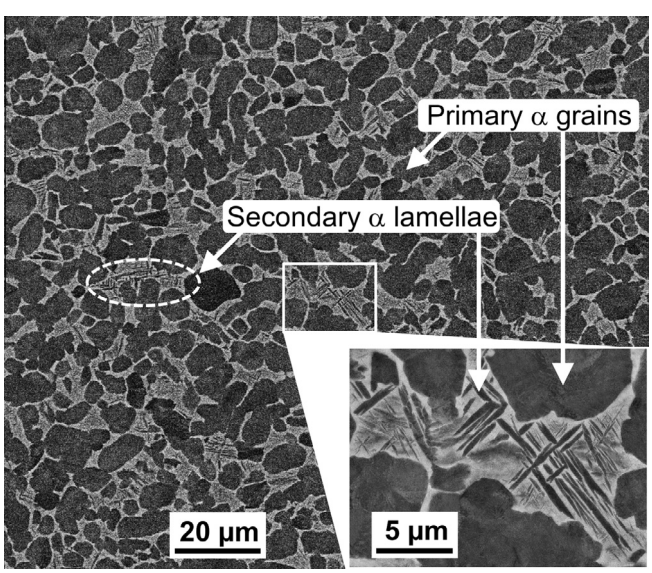

Fig. 1. BSE image of the initial microstructure of the Ti-662 alloy: equiaxed primary α grains and secondary α lamellae (dark grey) are found distributed in a β matrix (light grey).

3.2. Influence of heating rate on phase transformation kinetics

3.2.1. In situ high energy synchrotron X-ray diffraction

Fig. 3 presents the evolution of the volume fractions of α and β as a function of temperature during continuous heating at 5 K/min (Fig. 3a) and 100 K/min (Fig. 3b) obtained by Rietveld analysis ($R_w \leqslant 8\%$). No apparent peak broadening of the HEXRD spectra was observed during heating. The results for 20 K/min lie between those for 5 and 100 K/min and are not shown to improve legibility (see Online file 1 of Supplementary data). At the beginning of the heating (~300–430 °C) all conditions present ~85 and ~15 vol.% of α and β, respectively. As the temperature increases, between ~430 and 530 °C the α volume fraction suffers a slight increase of ~3 vol.% for 5 K/min (Fig. 3a), while 100 K/min does not present any changes up to ~590 °C (Fig. 3b). In addition, between ~500 and 560 °C the 20 K/min condition shows an increase of ~1 vol.% in the volume fraction of α. Thereafter, all conditions undergo a continuous α → β transformation up to temperatures close to T_β (~945 °C).

Fig. 4(a) and (b) show the evolution of lattice parameter variations as a function of temperature during continuous heating at 5 and 100 K/min, respectively. At low temperatures (~300–400 °C) all parameters increase practically with the same linear tendency. In this way, the linear coefficients of thermal expansion (CTE) were determined in this temperature range and are presented in Table 5 for the different heating rates investigated.

During heating with 5 K/min a_β shows a local minimum (decrease of ~0.1%) between ~430 and 530 °C (Fig. 4a). No detachment from linearity is observed for a_α and c_α in this temperature range. Thereafter, a_β undergoes a steep increase up to ~1.9% at ~950 °C. Furthermore, c_α presents a nonlinear increase up to ~1.2% (~0.6% over a_α) at $T > 760$ °C. A linear growth of the lattice parameters can be observed for 100 K/min up to ~590 °C (Fig. 4b). At this temperature a_β detaches from linearity exhibiting a steeper expansion up to ~1.8% at ~950 °C. Meanwhile, c_α presents a slightly higher expansion than a_α up to ~880 °C and then undergoes a steeper increase up to ~1.0% (~0.2% higher than for a_α).

Fig. 4(c) shows the evolution of a_β variations as a function of temperature during heating at 5, 20 and 100 K/min. The magnitude of the drop at the local minimum and subsequent increase of a_β (described for Fig. 4(a) and (b)) decreases and shifts to higher temperatures with increasing heating rate. The 5 and 100 K/min curves present a difference of about 0.2% at the local minimum (~530 °C).

3.2.2. Metallographic analysis

Fig. 5(a) and (b) show the evolution of the area fractions of α, primary α, secondary α and β obtained by MA as a function of temperature during heating at 5 and 100 K/min, respectively. Initially, α amounts 75 ± 3% (73 ± 2.5% and 2 ± 0.5% for primary α and secondary α, respectively) and β 25 ± 3%. It is feasible to compare the results obtained by MA with those obtained by HEXRD if a homogeneous distribution of phases is assumed. The evolution of the frozen microstructures quantified by MA reproduces very well the HEXRD results (Fig. 3). There is a difference of about 5–10 vol.% in the initial volume fraction of phases, which may be due to the insufficient segmentation of small secondary α lamellae during MA (compare insert in Fig. 1 with Fig. 2). No changes are observed during heating up to ~650 and 700 °C for 5 and 100 K/min, respectively, where the α → β transformation starts. Thereafter, the volume fractions of secondary and primary α decrease

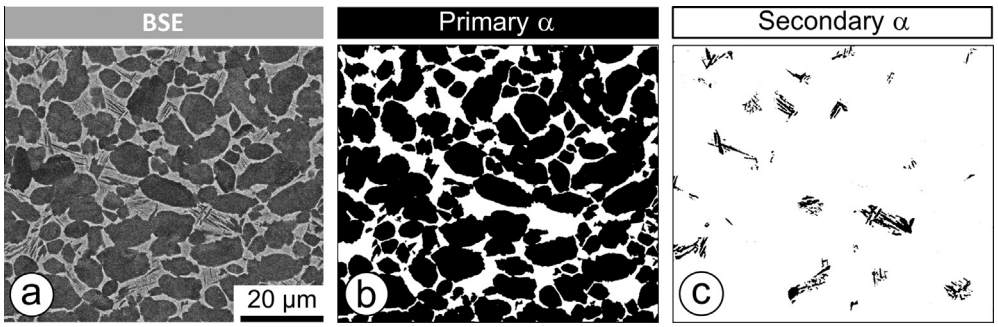

Fig. 2. Segmentation of α for the initial microstructure of the Ti-662 alloy: (a) BSE image, while (b) and (c) show the corresponding segmentations of primary α (black) and β (white), and secondary α (black).

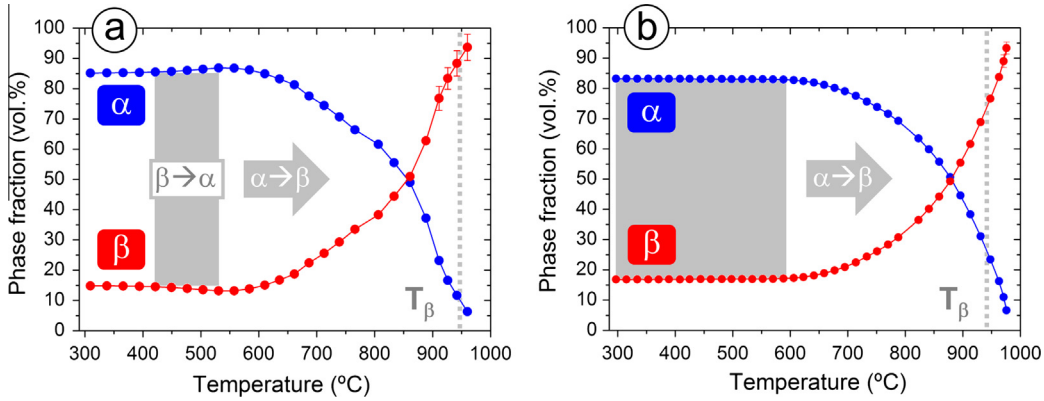

Fig. 3. Evolution of the volume fractions of α and β obtained by Rietveld analysis as a function of temperature during continuous heating at (a) 5 K/min and (b) 100 K/min.

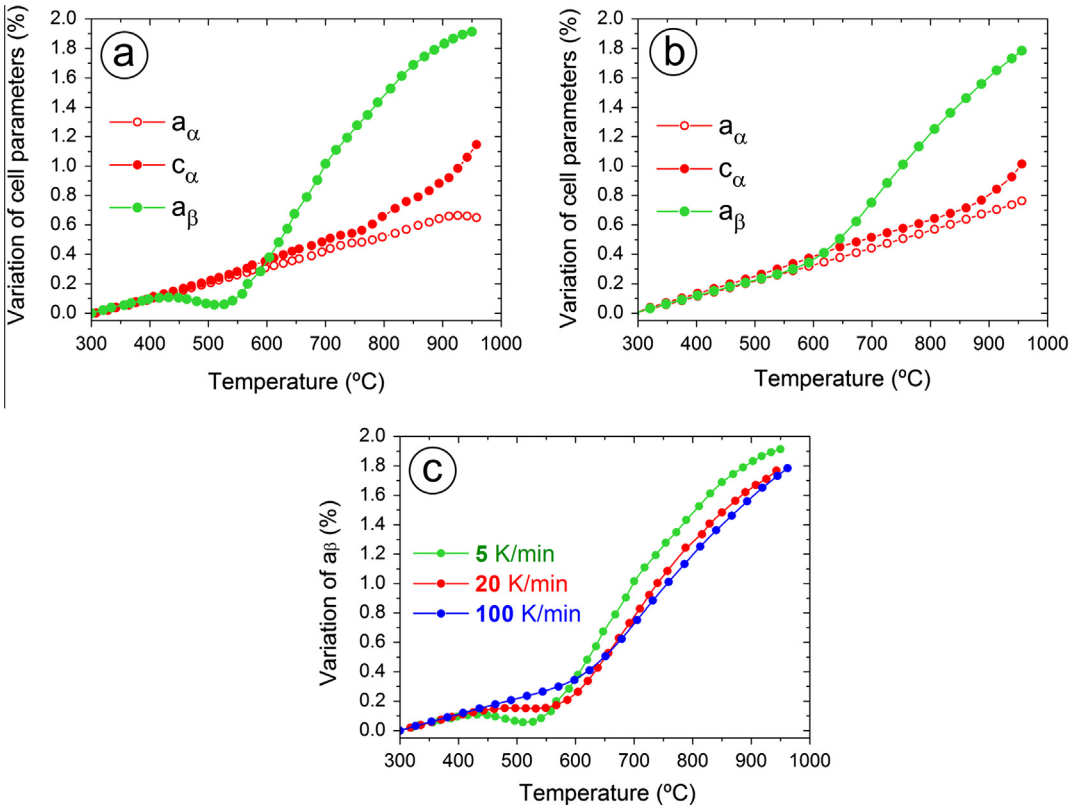

Fig. 4. Evolution of lattice parameter variations as a function of temperature during heating at (a) 5 K/min and (b) 100 K/min. (c) Evolution of a_β variation as a function of temperature during heating at 5, 20 and 100 K/min.

Table 5
Linear coefficients of thermal expansion for the lattice parameters of α and β between 300 and 400 °C.

Linear coefficients of thermal expansion (K^{-1})			
Lattice parameter	Heating rate (K/min)		
	5	20	100
a_β	9.6×10^{-6}	1.0×10^{-5}	1.0×10^{-5}
a_α	1.0×10^{-5}	1.0×10^{-5}	1.0×10^{-5}
c_α	1.1×10^{-5}	1.2×10^{-5}	1.2×10^{-5}

continuously for both heating rates. The secondary α lamellae dissolve completely between 800 and 850 °C as it was confirmed by observing the micrographs, while the volume fraction of primary α decreases continuously up to temperatures close to T_β.

3.3. Element partitioning during continuous heating

Fig. 6 shows the evolution of the mean concentration (at.%) of Ti, Al and V in primary α obtained by EDX of frozen microstructures continuously heated at 5 and 100 K/min. It must be pointed out that the quantification in Fig. 6 considers the concentration obtained in each pixel of the EDX map after segmentation of primary α grains (see Section 2.3.2). Each point in Fig. 6 was then calculated as the mean value of the individual concentration of all analysed pixels. As a consequence, the sum of the concentration of elements at a given temperature is not necessarily 100 at.%. At RT, primary α presents 77 ± 1.8, 15 ± 1.5 and 2.5 ± 0.9 at.% of Ti, Al and V, respectively. These concentrations remain practically constant up to 400 °C. The 5 K/min condition at 530 °C (temperature at which the local minimum is observed for a_β in Fig. 4a) presents a Ti concentration increase of 8.4 ± 1.4 at.%. A minor increment in the concentration of Al may take place, although the difference is not significant due to relatively large error bars. At $T > 530$ °C, the concentration of Ti in primary α continuously decreases down to 78 ± 1 at.% at 940 °C. On the other hand, the 100 K/min condition does not exhibit variations in the concentrations of Al, Ti and V up to 780 °C. Thereafter, the mean concentrations of Ti and Al at 940 °C decrease down to 75 ± 1 and 11.7 ± 0.8 at.%, respectively.

Fig. 7(a) shows the initial microstructure of the Ti-662 alloy, while the corresponding V maps obtained by μ-XRF and EDX are shown in Fig. 7(b) and (c), respectively. The scale in μ-XRF maps is normalized with respect to the average fluorescence intensity. Although both methods present a β matrix richer in V (by ~6.5 at.% with respect to primary α grains according to point analysis carried out by EDX), μ-XRF presents higher spatial and elemental resolution. Unfortunately, the spatial resolution is not

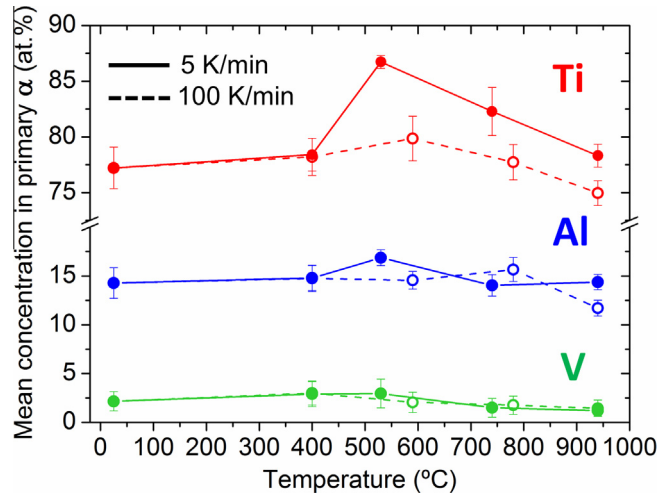

Fig. 6. Evolution of the mean concentration of Ti, Al and V in primary α obtained by EDX of frozen microstructures continuously heated at 5 and 100 K/min.

sufficient for resolving the fine secondary α lamellae (*thickness of the lamellae* < 1 μm). On the other hand, Fig. 7(d) shows the frozen microstructure of the Ti-662 alloy heated up to 530 °C with 5 K/min, while Fig. 7(e) and (f) present its corresponding V maps obtained by μ-XRF and EDX. This temperature corresponds to the temperature at which a local minimum is observed for a_β in Fig. 4(a). μ-XRF shows an increment of V in the β matrix (red regions) for this condition. A similar concentration increase was obtained for other β stabilizers, namely Cu and Fe (see Online file 2 of Supplementary data). In contrast to this, the EDX maps do not show any changes, revealing the advantage of μ-XRF to study local compositional changes of V, Fe and Cu in the Ti-662 alloy.

Fig. 8(a) presents the map of V in primary α obtained by μ-XRF for the initial microstructure (RT), while Fig. 8(b) and (c) present the equivalent maps for the frozen microstructures heated up to 530 °C and 590 °C with 5 and 100 K/min, respectively. 530 °C corresponds to the temperature at which the local minimum is observed for the evolution of a_β at 5 K/min (Fig. 4a). Similarly, 590 °C is the temperature at which a_β starts growing nonlinearly at 100 K/min (Fig. 4b). After heating up to 530 °C with 5 K/min, primary α grains become poorer (dark blue) in V (comparing Fig. 8(a) and (b)). Moreover, an increase in the concentration of Ti in the primary α grains (increase of μ-XRF intensity) was qualitatively observed at this condition. On the other hand, after heating up to 590 °C with 100 K/min (Fig. 8c), the primary α grains show a majority of regions with V concentrations similar to the 25 °C condition (green). The concentration of V at the grain boundaries

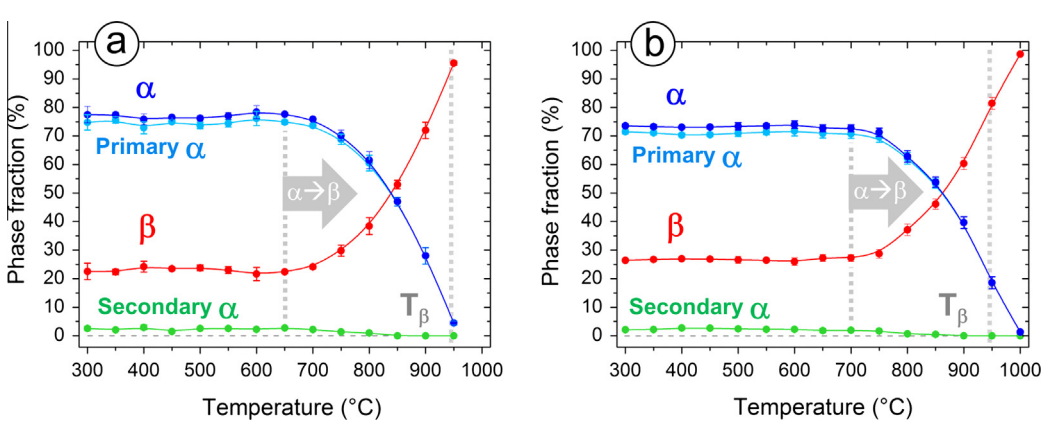

Fig. 5. Evolution of the area fractions of α, primary α, secondary α and β obtained by metallographic analysis as a function of temperature during continuous heating at (a) 5 K/min and (b) 100 K/min.

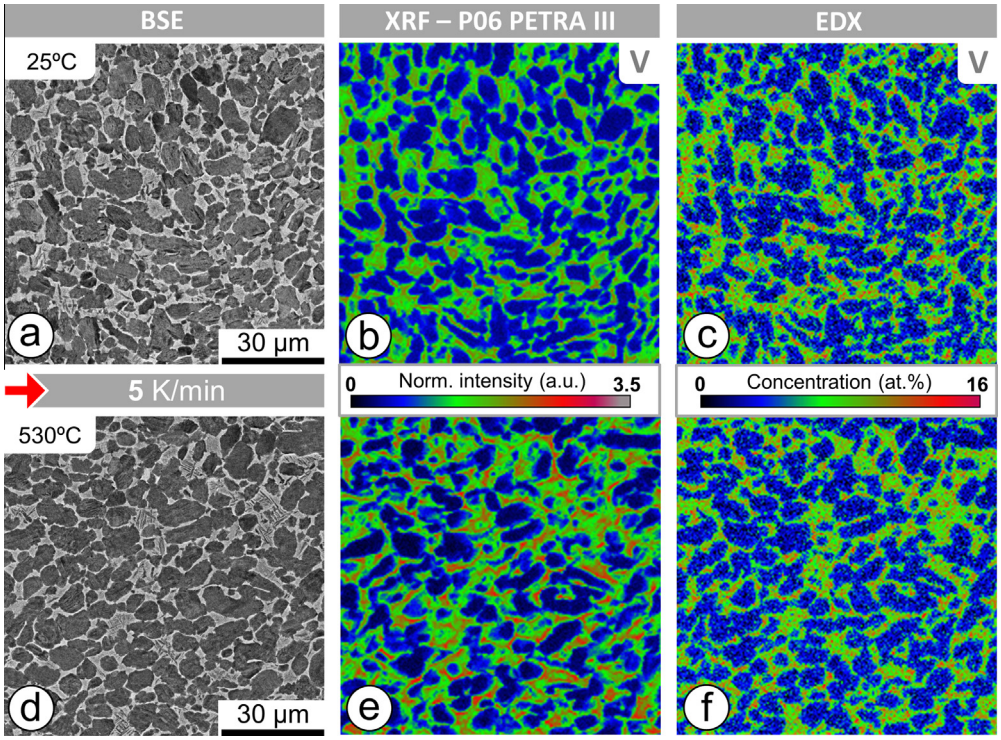

Fig. 7. BSE images of (a) initial microstructure and (d) microstructure frozen after continuous heating up to 530 °C with 5 K/min. Corresponding V maps: (b and e) µ-XRF and (c and f) EDX.

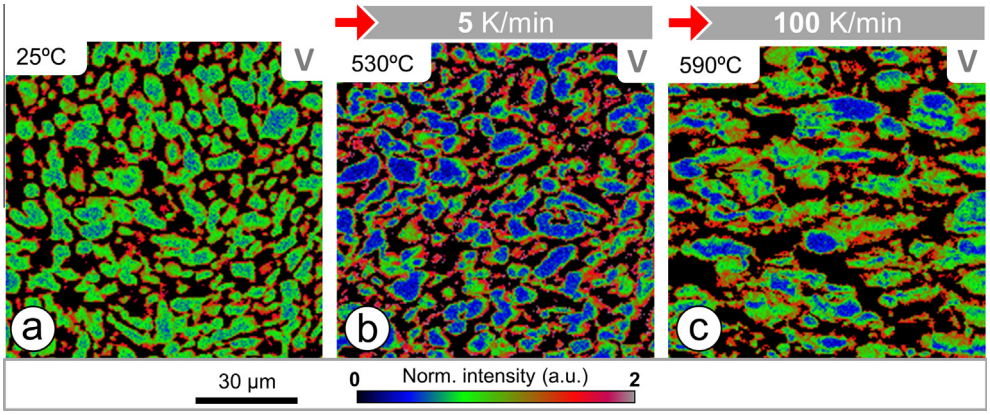

Fig. 8. Distribution of V in primary α obtained by µ-XRF for (a) the initial and frozen microstructures of the Ti-662 alloy heated up to (b) 530 °C with 5 K/min and (c) 590 °C with 100 K/min.

(orange–red regions) may be affected by contributions from deeper layers below the sample's surface, owing to the higher probability of probing more than one phase in a single spot. Therefore, these regions are not considered here.

Fig. 9(a) shows the frozen microstructure of the Ti-662 alloy heated up to 940 °C with 5 K/min, while Fig. 9(b) and (c) show the corresponding V maps obtained by µ-XRF and EDX, respectively. This condition presents few and small primary α grains poor in V (blue in Fig. 9b), dispersed in a β matrix (red[1] in Fig. 9b) with a high V concentration but inhomogeneous distribution: V concentration increases gradually with increasing distance from α grains (Fig. 9b). Some regions in Fig. 9(b) (indicated by arrows) with significantly low concentrations of V cannot be correlated with the primary α grains in the FEG-SEM micrograph (Fig. 9a). This is a consequence of the contributions from parts of the sample below the surface, excited by the deeper penetrating synchrotron beam (relevant depth ~3 µm for the V–K_α line, see Table 4) that reveals α grains below the surface imaged by FEG-SEM. On the contrary, EDX does not present significant heterogeneities of V in β (Fig. 9c). Fig. 9(d)–(f) show the respective distributions of Fe, Cu and Ti. Similar to V, Fe and Cu present poor and rich concentrations in primary α and β, respectively, while Ti presents slightly higher concentrations in α. These elements seem more homogeneously distributed in β than V (Fig. 9(d)–(f)).

4. Discussion

4.1. Thermal expansion

CTE around $1.0 \times 10^{-5}\,K^{-1}$ were obtained from all lattice parameters during the first stage of heating: from RT up to ~400,

[1] For interpretation of color in Fig. 9, the reader is referred to the web version of this article.

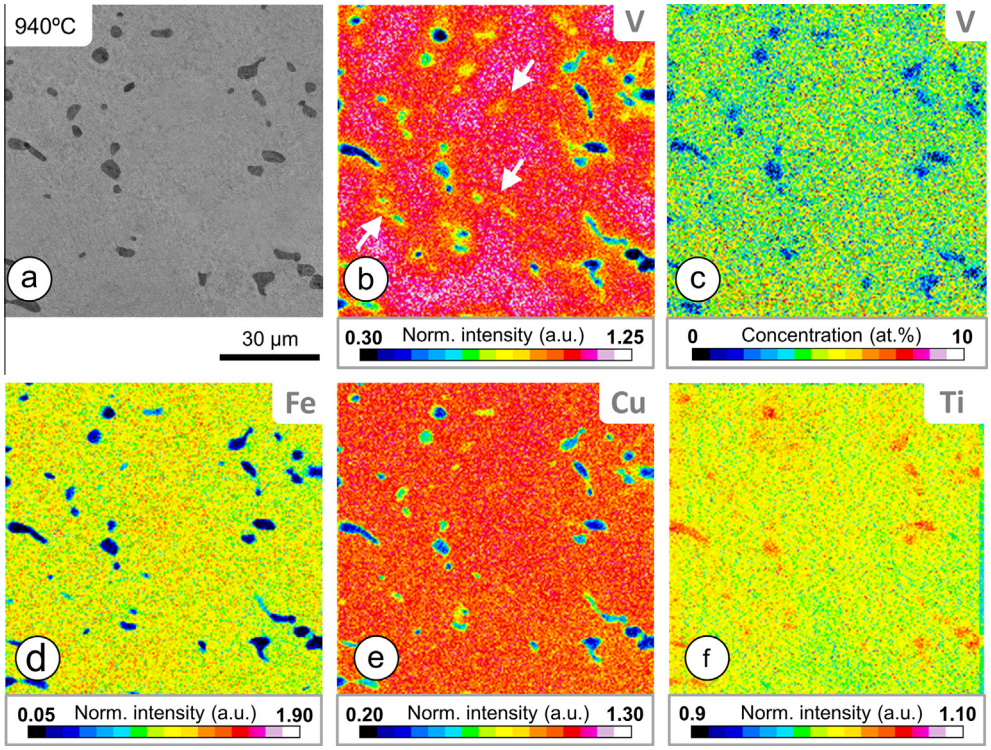

Fig. 9. (a) BSE image of the frozen microstructure of the Ti-662 alloy heated continuously up to 940 °C with 5 K/min, and its corresponding V maps obtained by (b) μ-XRF and (c) EDX. Additional maps of (d) Fe, (e) Cu and (f) Ti obtained by μ-XRF for the current microstructure.

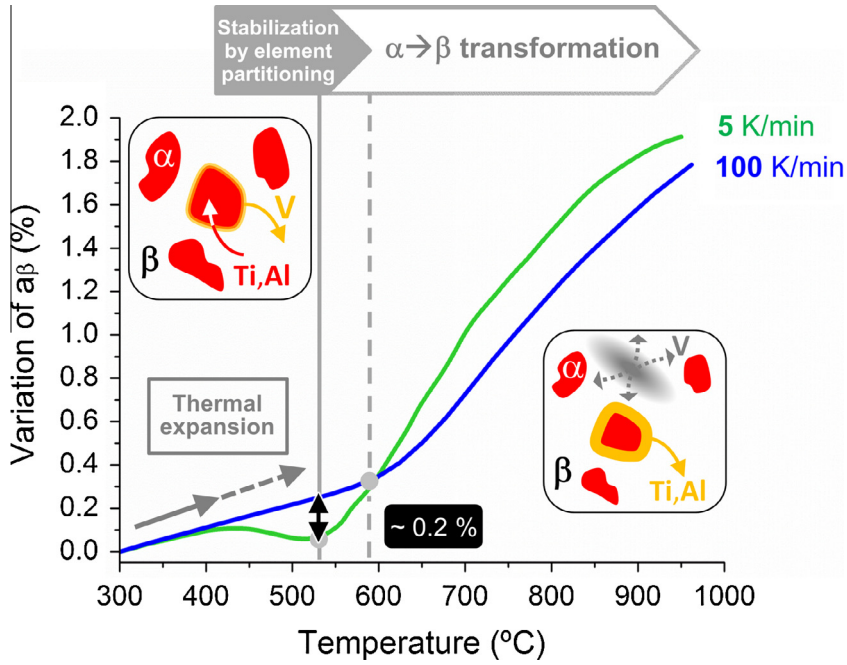

Fig. 10. The different transformation stages identified during heating are illustrated with its kinetically related processes during the evolution of a_β variations as a function of temperature during heating at 5 and 100 K/min.

450 and ~590 °C for 5, 20 and 100 K/min, respectively (Fig. 4). These values are very close to the CTE presented for the studied alloy between RT and 100 °C (9.0×10^{-6} K^{-1}) [25], and similar to those reported for a_β and a_α during heating of the analogous Ti–6Al–4V alloy between RT and 400 °C (9.2×10^{-6} and 9.7×10^{-6} K^{-1}, respectively) [16]. This, together with the fact that no changes are observed in phase volume fractions (Fig. 3) or mean element concentrations in primary α (Fig. 6), indicates that this initial stage is controlled by thermal expansion. This effect is illustrated in the low temperature region of Fig. 10 for the variation of a_β as a function of temperature during heating at 5 and 100 K/min.

4.2. Stabilization by element partitioning

A simultaneous increase of ~3 vol.% of α and decrease of ~0.1% of a_β were observed between ~430 and 530 °C (Figs. 3(a) and 4(a)) during heating at 5 K/min. The slight increase of α volume fraction can be correlated with the one obtained at ~450 °C by calculations based on the equilibrium phase diagram of the analogous Ti–6Al–4V alloy [17]. Furthermore, the local minimum of a_β decreases with increasing heating rate (Fig. 4c), and it is practically negligible for the 100 K/min condition, indicating a diffusion-controlled process. At 530 °C and 5 K/min, primary α experiences an increase of 8.4 ± 1.4 and 2 ± 1.2 at.% in the concentration of Ti and Al (Fig. 6) with respect to 400 °C, while an increase in the concentration of V (Fig. 7e), Cu and Fe is observed in β. This indicates that element partitioning occurs between ~430 and 530 °C for the 5 K/min condition: α and β are enriched by their respective element stabilizers. The changes in the volume fraction of α and in the cell parameter a_β occur close to the initial aging temperature of the alloy, i.e. 540 °C (see Section 2.1). The element partitioning that takes place in this temperature range induces the formation of fine and homogeneously distributed secondary α lamellae with positive influence on mechanical properties [3,4]. The initial aging step at 540 °C was sufficiently long (4–8 h) to achieve thermodynamic equilibrium. Equilibrium conditions are lost during the relatively fast subsequent air cooling. When the alloy is slowly reheated (as it is the case for 5 K/min) the microstructure tends to reach again thermodynamic equilibrium conditions once diffusion is activated at $T > 430$ °C.

The microstructure heated up to 530 °C at 5 K/min displays lower concentrations of V in the primary α grains than at RT (Fig. 8b). This points to an exchange of V atoms between α and β. Furthermore, the slight increase in α volume fraction mentioned above (Fig. 3a) indicates the occurrence of a β → α transformation for the 5 and 20 K/min conditions already at this temperature. This transformation is mainly controlled by diffusion of V from α to β [36]. Since the diffusivity of V in β is lower than in α, the α grain boundaries are first enriched with atoms of this element which gradually diffuse into β [36,37].

The increase of Ti concentration in primary α observed qualitatively (μ-XRF) and quantitatively (Fig. 6) during the β → α transformation for the 5 K/min condition implicates a loss of Ti in β. This, together with the fact that Ti has the largest atomic radius among the alloying elements (1.76 Å compared to 1.71, 1.56, 1.45, 1.45, 1.18, 0.67, 0.53 and 0.48 Å for V, Fe, Sn, Cu, Al, C, H and O respectively [38]) explains the local minimum exhibited by a_β at ~530 °C (Fig. 4a). At this stage of the heating the volume fraction of β is significantly lower than that of α: ~15 and ~85 vol.% were obtained by in situ HEXRD for β and α, respectively. The HEXRD results give an average size of the lattice parameters within the gauge volume investigated. Therefore, small compositional variations will be less clearly reflected the larger the volume fraction of the phase. This means that the significant differences between the volume fractions of α and β make the β phase more susceptible to the compositional changes occurring during element partitioning. A similar drop in a_β was observed during continuous heating of a Ti–6Al–4V alloy with an initial volume fraction of β of 12 vol.% [16]. Three hypotheses were suggested to explain this effect: diffusion of V into β, relaxation of thermal stresses and formation of ω phase. Also, the decrease of a_β by increasing the content of V has been experimentally reported in previous investigations of the α + β Ti–6Al–4V alloy [39]. The results presented in the current work indicate that the first hypothesis in [16] plays a decisive role: diffusion of V into β is accompanied by diffusion of Ti into α. Then, β is enriched by V and since the atomic radius of V is smaller than that of Ti, the lattice parameter a_β decreases. In agreement with the present results, the decay of a_β observed during isothermal treatment of a β metastable Ti-17 alloy was attributed to the decrease of Ti in β based on thermodynamic calculations [18].

Contrarily to 5 K/min, the fast 100 K/min condition shows a linear increase of a_β and constant phase volume fractions up to ~590 °C (see Figs. 3(b) and 4(b)). This condition does not exhibit variations in the mean element concentration in primary α up to 780 °C (Fig. 6). Moreover, the μ-XRF map of the microstructure frozen at this temperature shows regions within primary α grains with V concentration similar to the RT condition and higher than for 5 K/min (Fig. 8). This indicates a lower stabilization degree of α than for 5 K/min and, therefore, less element partitioning for 100 K/min. The reason for this is that there is not enough time for diffusion and consequent element partitioning up to 590 °C when diffusion becomes sufficiently fast.

Fig. 10 emphasizes the difference of expansion of a_β by ~0.2% between 5 and 100 K/min during the element partition between ~430 and 530 °C. This difference is a consequence of the loss of Ti suffered by β during heating at 5 K/min between 430 and 530 °C, and indicates a higher effect of element partitioning for this condition. This is illustrated schematically in the left insert of Fig. 10.

4.3. Kinetics of the α → β phase transformation

The onset temperatures for the α → β transformation obtained by in situ HEXRD are lower than the ones presented by MA. For 5 K/min these temperatures are ~530 and 650 °C, while for 100 K/min are ~590 and 700 °C for HEXRD and MA, respectively. The 20 K/min condition, which was only investigated by HEXRD, shows an onset of the α → β transformation at ~560 °C. Both methods present a shift of the transformation to higher temperatures with increasing heating rate, illustrating the diffusion character of this process. The difference between methods may be attributed to the dissolution of the small (and thin) secondary α lamellae that could not be detected by MA (see Section 3.1). After dissolution of secondary α lamellae (~800 °C) the results of both methods are comparable (see Figs. 3 and 5). Secondary α lamellae and primary α grains transform into β until all secondary α lamellae are dissolved (~800 °C). The transformation of primary α grains into β continues up to T_β (Fig. 5).

Fig. 10 shows that the onset of the α → β transformation determined by HEXRD coincides with the steep increase in a_β for both heating rates (~530 and 590 °C for 5 and 100 K/min, respectively). It is argued that the increase of the lattice parameter a_β is caused by the increase of Ti concentration in β. This happens by two

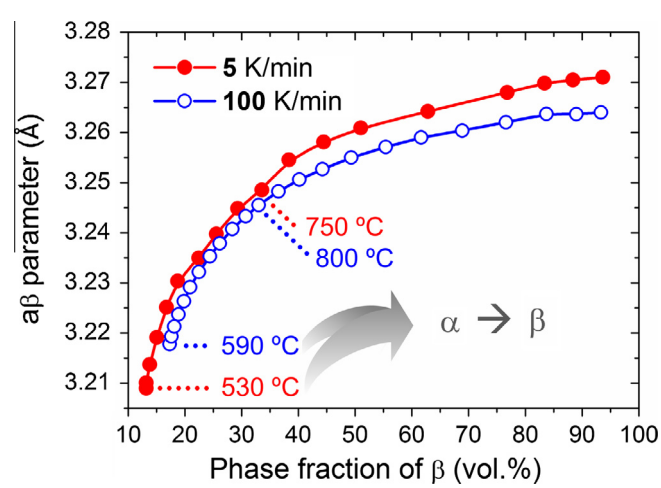

Fig. 11. Evolution of a_β during the α → β transformation as a function of the volume fraction of β for 5 and 100 K/min.

different processes [17]. First, Ti diffuses from α to β as shown in Fig. 6 due to the lower equilibrium concentration of Ti in primary α at these temperatures. Second, the volume fraction of β increases and the Ti-rich α phase transforms into β. The V atoms redistribute as the amount of β becomes larger and the overall vanadium concentration decreases in favour of Ti. The inhomogeneous distribution of V during the α → β transformation, with V concentration increasing gradually with increasing distance from α grains, can be seen in Fig. 9(b) for the 5 K/min condition at 940 °C. These two effects, namely the diffusion of Ti from α to β and the redistribution of V within β are responsible for the steep increase of a_β observed in Fig. 10. Diffusion of Al from α into β has also been determined by thermodynamic calculations as a component of element partitioning during the α → β transformation [17]. The insert on the right of Fig. 10 illustrates schematically the effects identified during the α → β transformation. Although not resolved by the techniques applied in the current work, the diffusion of Al has been included to give a more complete picture.

The shift of the variation of a_β to higher temperatures with increasing heating rate is certainly related to the longer diffusion times available for 5 K/min. However, other effects may also be playing a role as it can be inferred from Fig. 11. Here, a_β is plotted as a function of the volume fraction of β for the 5 and 100 K/min conditions during the α → β transformation. The a_β values practically coincide up to a β volume fraction of ~33 vol.% indicating that the shift observed in Fig. 10 is due to kinetic effects up to a temperature of ~750 and 800 °C for 5 and 100 K/min, respectively. For higher temperatures and higher β volume fractions, a_β is larger for 5 than for 100 K/min. This may be due to compositional differences in β for the different heating rates. A similar dependence of a_β with cooling rate was reported in [18] for a Ti-17 alloy.

The nonlinear increase of c_α at $T > \sim760$ and 880 °C for 5 and 100 K/min, respectively (Fig. 4(a) and (b)), has been attributed to O enrichment according to thermodynamic calculations under equilibrium conditions in a Ti-17 alloy (Ti–5Al–4Mo–4Cr–2Zr–2Sn with 1200 ppm of O) [18]. Unfortunately, the evolution of this element could not be revealed by the experimental techniques used in the present work. However, the diffusional nature of this process can be inferred by its displacement to higher temperatures as the heating rate increases (Fig. 4(a) and (b)). Furthermore, the different expansions observed for a_α and c_α during transformation may be related to the anisotropic diffusivity in α along the *c* and *a* axis [40,41].

5. Conclusions

The role of element partitioning on phase transformation kinetics of the α + β Ti–6Al–6V–2Sn alloy with initial bi-modal microstructure has been studied experimentally as a function of heating rate. The investigations were carried out combining quantitative phase analysis using in situ high energy synchrotron X-ray diffraction and metallography with elemental analysis by synchrotron micro X-ray fluorescence and energy dispersive X-ray spectroscopy. The following conclusions can be drawn from the results obtained:

- The lattice parameters of α and β present similar linear coefficients of thermal expansion from RT up to ~400, 450 and 590 °C for heating rates of 5, 20 and 100 K/min, respectively. No compositional and volume fraction variations of phases are observed in these temperature ranges. This indicates that the increase in the lattice parameters is controlled by thermal expansion during the initial period of heating.
- A simultaneous increase in the volume fraction of α and decrease of the lattice parameter a_β takes place at intermediate temperatures, i.e. 430–530 °C and 500–560 °C at 5 and 20 K/min, respectively. This is a consequence of element partitioning between phases: α and β are enriched by their respective alloying element stabilizers (Al for α, and V, Cu, Fe for β), while Ti atoms diffuse from β to α. Within this temperature range β is susceptible to more pronounced compositional changes owing to its low volume fraction. Since the atomic radius of Ti is larger than that of the other alloying elements, the loss of Ti in β results in the local minimum exhibited by a_β in this temperature range.
- Two different processes are observed simultaneously up to ~800 °C during the α → β transformation: secondary α lamellae and primary α grains transform into β until all secondary α lamellae are dissolved. Thereafter, the transformation of primary α grains into β continues up to temperatures close to the β-transus temperature.
  The lattice parameter a_β undergoes a steep increase during the α → β transformation. The onset of both processes show a shift to higher temperatures with increasing heating rate owing to the different diffusion times/rates at each condition. This kinetic effect can be confirmed up to 750 and 800 °C (volume fraction of β ~33 vol.%) for 5 and 100 K/min, respectively, where a_β presents similar expansion in both cases. Thereafter, a_β is larger for 5 K/min indicating that other effects, such as compositional differences, may also play a role in this temperature range during the α → β transformation.
- Synchrotron micro X-ray fluorescence and energy dispersive X-ray spectroscopy were applied to trace the evolution of alloying elements during continuous heating of the Ti-662 alloy. The results show that EDX analysis can be used to obtain mean concentration of elements in each phase, while the high spatial resolution and elemental sensitivity achieved by micro X-ray fluorescence allowed analysing local concentration variations.

Acknowledgements

The authors acknowledge the COMET-Program of the Austrian Research Promotion Agency (FFG) and the Province of Upper Austria (LOÖ), Grant No. 820492 for financial support.

The European Synchrotron Radiation Facility (ESRF) and the Deutsches Elektronen-Synchrotron (DESY) are acknowledged for the provision of synchrotron radiation facilities in the framework of the proposals MA1268 and I-20130323 EC, respectively. The research leading to these results has received funding from the European Community's Seventh Framework Programme (FP7/2007-2013) under grant agreement n° 312284.

The University Service for Transmission Electron Microscopy (USTEM) of the Vienna University of Technology is acknowledged for the provision of the FEG-SEM microscope.

F. Warchomicka from TU-Graz is acknowledged for the support during preparation and execution of the diffraction tests. D. Canelo from TU-Wien is also acknowledged for the collaboration during the synchrotron experiments.

The authors would like to thank Ellie Bennett for proof-reading the manuscript.

Appendix A. Supplementary material

Supplementary data associated with this article can be found, in the online version, at http://dx.doi.org/10.1016/j.jallcom.2014.11.176.

References

[1] R.R. Boyer, An overview on the use of titanium in the aerospace industry, Mater. Sci. Eng. A 213 (1996) 103–114.

[2] D. Banerjee, J.C. Williams, Perspectives on titanium science and technology, Acta Mater. 61 (2013) 844–879.
[3] G. Lütjering, J.C. Williams, Titanium, second ed., Springer, Berlin, 2007.
[4] C. Leyens, M. Peters, Titanium and Titanium Alloys, first ed., Wiley-VCH, Weinheim, 2003.
[5] M. Wollmann, J. Kiese, L. Wagner, Properties and applications of titanium alloys in transport, in: L. Zhou, H. Chang, Y. Lu, D. Xu (Eds.), Ti-2011, Science Press Beijing, Beijing, 2011, pp. 837–844.
[6] R. Martin, D. Evans, Reducing costs in aircraft: the metals affordability initiative consortium, JOM 52 (2000) 24–28.
[7] F.H. Froes, H. Friedrich, J. Kiese, D. Bergoint, Titanium in the family automobile: the cost challenge, JOM 56 (2004) 40–44.
[8] A.D. Hartman, S.J. Gerdemann, J.S. Hansen, Producing lower-cost titanium for automotive applications, JOM 50 (1998) 16–19.
[9] B.E. Hurless, F.H. Froes, Lowering the cost of titanium, Amptiac 6 (2002) 3–9.
[10] R.R. Boyer, D.U. Furrer, The potential advantages of microstructure modeling of titanium to the aerospace industry, in: S. Ghosh, J.M. Castro, J.K. Lee (Eds.), Numiform 2004, AIP Conference proceedings, New York, 2004, pp. 1694–1699.
[11] S. Malinov, W. Sha, Modeling thermodynamics, kinetics, and phase transformation morphology while heat treating titanium alloys, JOM 57 (2005) 42–45.
[12] S.L. Semiatin, S.L. Knisley, P.N. Fagin, F. Zhang, D.R. Barker, Microstructure evolution during alpha-beta heat treatment of Ti–6Al–4V, Metall. Mater. Trans. A 34 (2003) 2377–2386.
[13] A. Krumphals, C. Poletti, F. Warchomicka, M. Stockinger, C. Sommitsch, Modeling of two-phase grain structure in the titanium alloy Ti–6Al–4V using cellular automata, Int. J. Mult. Comp. Eng. 12 (2014) 23–31.
[14] S. Malinov, W. Sha, The neutral network modeling of titanium alloy phase transformation and mechanical properties, JOM 57 (2005) 54–57.
[15] S.M.C. Van Bohemen, M. Van der Laars, J. Sietsma, S. Van der Zwaag, Modelling of the $\beta \rightarrow \alpha + \beta$ transformation in a metastable β Ti alloy based on the growth kinetics and the morphology of the α plates, Int. J. Mater. Res. 98 (2007) 476–484.
[16] J.W. Elmer, T.A. Palmer, S.S. Babu, E.D. Specht, In situ observations of lattice expansion and transformation rates of α and β phases in Ti–6Al–4V, Mater. Sci. Eng. A 391 (2005) 104–113.
[17] J.W. Elmer, T.A. Palmer, S.S. Babu, T. Debroy, Phase transformation dynamics during welding of Ti–6Al–4V, J. Appl. Phys. 95 (2004) 8327–8339.
[18] F. Bruneseaux, E. Aeby-Gautier, G. Geandier, J.C. Teixeira, B. Appolaire, P. Weisbecker, A. Mauro, In situ characterizations of phase transformation kinetics in the Ti17 titanium alloy by electrical resistivity and high temperature synchrotron X-ray diffraction, Mater. Sci. Eng. A 476 (2008) 60–68.
[19] S. Malinov, W. Sha, P. Markovsky, Experimental study and computer modelling of the $\beta \rightarrow \alpha + \beta$ phase transformation in β 21s alloy at isothermal conditions, J. Alloys Comp. 348 (2003) 110–118.
[20] K.D. Liss, A. Bartels, A. Schreyer, H. Clemens, High-energy X-rays: a tool for advanced bulk investigations in material science and physics, Texture Microstruct. 35 (2003) 219–252.
[21] P. Barriobero-Vila, G. Requena, F. Warchomicka, A. Stark, N. Schell, T. Buslaps, Phase transformation kinetics during continuous heating of a β-quenched Ti–10V–2Fe–3Al alloy, J. Mater. Sci. (2014). <http://link.springer.com/article/10.1007/s10853-014-8701-6>.
[22] F. Adams, B. Vekemans, G. Silversmit, B.D. Samber, L. Vincze, Microscopic X-ray fluorescence analysis with synchrotron radiation, in: A. Vértes, S. Nagy, Z. Klencsár, R.G. Lovas, F. Rösch (Eds.), Handbook of Nuclear Chemistry, Springer, Dordrecht, 2011, pp. 1737–1760.
[23] W. Seifert, O.F. Vyvenko, T. Arguirov, A. Erko, M. Kitter, C. Rudorf, M. Salome, M. Trushin, I. Zizak, Synchrotron microscopy and spectroscopy for analysis of crystal defects in silicon, Phys. Status Solidi C 6 (2009) 765–771.
[24] D.I. Kaplan, D.B. Hunter, P.M. Bertsch, S. Bajt, D.C. Adriano, Application of synchrotron X-ray fluorescence spectroscopy and energy dispersive X-ray analysis to identify contaminant metals on groundwater colloids, Environ. Sci. Technol. 28 (1994) 1186–1189.
[25] R.R. Boyer, G. Welsch, E.W. Collings, Material Properties Handbook: Titanium Alloys, fourth ed., ASM International, Ohio, 1994.
[26] H. Fujii, Continuous cooling transformation characteristics of $\alpha + \beta$ titanium alloys, Nippon Steel Tech. Rep. 62 (1994) 74–79.
[27] M. Donachie, Titanium, a Technical Guide, second ed., ASM International, Ohio, 2000.
[28] C. Poletti, Hot deformation and properties of PRTi alloys, Ph.D. Thesis, Vienna University of Technology, 2005.
[29] M.D. Abramoff, P.J. Magalhães, S.J. Ram, Image processing with Imagej, Biophoton. Int. 11 (2004) 36–42.
[30] ID15 – High Energy Scattering Beamline, ESRF, (accessed 18.10.2014), <http://www.esrf.eu/UsersAndScience/Experiments/StructMaterials/ID15>.
[31] L. Lutterotti, S. Matthies, H.R. Wenk, A.J. Schultz, J. Richardson, Combined texture and structure analysis of deformed limestone from time-of-flight neutron diffraction spectra, J. Appl. Phys. 81 (1997) 594–600.
[32] C.G. Schroer, P. Boye, J.M. Feldkamp, J. Patommel, D. Samberg, A. Schropp, A. Schwab, S. Stephan, G. Falkenberg, G. Wellenreuther, N. Reimers, Hard X-ray nanoprobe at beamline P06 at Petra III, Nucl. Instrum. Methods Phys. Res. Sect. A 616 (2010) 93–97.
[33] T. Schoonjans, A. Brunetti, B. Golosio, M. Sanchez del Rio, V.A. Solé, C. Ferrero, L. Vincze, The xraylib library for X-ray-matter interactions. Recent developments, Spectrochim. Acta Part B 66 (2011) 776–784.
[34] V.A. Solé, E. Papillon, M. Cotte, P. Walter, J. Susini, A multiplatform code for the analysis of energy-dispersive X-ray fluorescence spectra, Spectrochim. Acta Part B 62 (2007) 63–68.
[35] Software Genesis Spectrum, (accessed 18.10.2014), <http://www.mic.ucla.edu/materials/materials_handouts/EDS%20PDF%20files/GenEDS_spectrum_users_manual.pdf>.
[36] W. Sha, S. Malinov, Fine element method: morphology of β to α phase transformation, in: W. Sha, S. Malinov (Eds.), Titanium Alloys: Modelling of Microstructure, Properties and Applications, Woodhead Publishing, Cambridge, 2009, pp. 203–235.
[37] S.L. Semiatin, T.M. Brown, T.A. Goff, P.N. Fagin, D.R. Barker, R.E. Turner, J.M. Murry, J.D. Miller, F. Zhang, Diffusion coefficients for modeling the heat treatment of Ti–6Al–4V, Metall. Mater. Trans. A 35 (2004) 3015–3018.
[38] E. Clementi, D.L. Raimondi, W.P. Reinhardt, Atomic screening constants from SCF functions. II. Atoms with 37–86 electrons, J. Chem. Phys. 47 (1967) 1300–1307.
[39] R. Castro, L. Séraphin, Metallography and structure of TiAl6V4, Mem. Scientifique Rev. Metall. 63 (1966) 1025–1055.
[40] R.A. Perez, H. Nakajima, F. Dyment, Diffusion in α-Ti and Zr, Mater. Trans. JIM 44 (2003) 2–13.
[41] Y. Mishin, C. Herzig, Diffusion in the Ti–Al system, Acta Mater. 48 (2000) 589–623.

Acta Materialia 95 (2015) 90–101

Contents lists available at ScienceDirect

Acta Materialia

journal homepage: www.elsevier.com/locate/actamat

Influence of phase transformation kinetics on the formation of α in a β-quenched Ti–5Al–5Mo–5V–3Cr–1Zr alloy

Pere Barriobero-Vila [a,*], Guillermo Requena [b,c], Sabine Schwarz [d], Fernando Warchomicka [e], Thomas Buslaps [f]

[a] Institute of Materials Science and Technology, Vienna University of Technology, Karlsplatz 13/308, A-1040 Vienna, Austria
[b] Institute of Materials Science, German Aerospace Center (DLR), Linder Höhe, D-51147 Cologne, Germany
[c] Metallic Structures and Materials Systems for Aerospace Engineering, Institute of Metal Forming, RWTH Aachen University, Intzestraße 10, D-52062 Aachen, Germany
[d] University Service Centre for Transmission Electron Microscopy (USTEM), Vienna University of Technology, Wiedner Hauptstrasse 8-10/052, A-1040 Vienna, Austria
[e] Institute of Materials Science and Welding, Graz University of Technology, Kopernikusgasse 24, A-8010 Graz, Austria
[f] ID15, European Synchrotron Radiation Facility, Rue J. Horowitz, F-38042 Grenoble, France

ARTICLE INFO

Article history:
Received 3 March 2015
Revised 3 May 2015
Accepted 4 May 2015

Keywords:
Titanium alloys
High-energy X-ray diffraction
Phase transformation kinetics
Metastable phases
Spinodal decomposition

ABSTRACT

The effect of phase transformation kinetics on the formation of α in the β-quenched Ti–5Al–5Mo–5V–3Cr–1Zr metastable β titanium alloy is investigated as a function of heating rate by means of in situ high energy synchrotron X-ray diffraction complemented by metallographic analysis. Quantitative phase analysis based on the Rietveld method provides the continuous evolution of phase volume fractions and lattice parameters, revealing variations in the phase transformation sequence with increasing heating rate. The initial microstructure consists in a matrix of equiaxed metastable β grains with ω_{ath} particles located along dislocation lines as well as within domains associated with spinodal decomposition of β. During the first stage of slow heating diffusion-driven formation of the metastable phases ω and α''_{iso} takes place with further decomposition of β. This effect contributes to the formation of ω and is observed as a symmetric pattern of parallel domains that reflect compositional modulations in the matrix. Evidences of the role of dislocations during phase transformation are presented. Furthermore, the results show that the stable α phase forms via two different paths: (a) slow heating rates provide homogeneous distribution of fine α plates formed through the evolution of ω, while (b) fast heating rates suppress this mechanism and promote the formation of α only from β grain boundaries.

1. Introduction

Titanium-based alloys exhibit higher specific strength than other structural alloys within a broad range of service temperatures and present excellent corrosion resistance up to about 500 °C [1–3]. These properties concisely explain the wide number of applications of these alloys in the aerospace industry [4–6]. Their use is also of interest in the land transportation sector in order to comply with new performance and environmental targets such as the reduction of CO_2 emissions [3,7–9]. Metastable β titanium alloys offer higher strength levels and lower processing temperatures than α + β alloys [1,10]. Their structural properties are essentially defined by a homogeneous distribution of α/β interfaces associated with the presence of fine α precipitates embedded in a β matrix [1,10,11]. The characteristics of the α phase, i.e. its morphology, volume fraction, size and distribution, are strongly influenced by the phase transformation kinetics during thermal treatments [12–15]. Although important insights regarding the formation of α in metastable β titanium alloys have been reported, most studies are focused on isothermal ageing (e.g. [11,16–18]), while the effect of kinetic variables (e.g. heating rate) has received less attention. Achievements in this regard play certainly a role in the advance of modelling tools for microstructure prediction, which are still mainly based on thermodynamic analyses confined to phase equilibria. These tools require reliable experimental data for validation. Therefore, a correct understanding of the phase transformation kinetics is required for the optimization of functional alloy design and the development of theoretical models that lead to improvements of lead-time and cost savings [2,19,20]. Nowadays, continuous and univocal studies of phase transformation kinetics can be carried out in situ by high energy synchrotron

* Corresponding author. Tel.: +43 6803240923.
E-mail addresses: pere.vila@tuwien.ac.at (P. Barriobero-Vila), guillermo.requena@dlr.de (G. Requena), schwarz@ustem.tuwien.ac.at (S. Schwarz), fernando.warchomicka@tugraz.at (F. Warchomicka), buslaps@esrf.fr (T. Buslaps).

http://dx.doi.org/10.1016/j.actamat.2015.05.008
1359-6454/

X-ray diffraction (HEXRD) [21,22]. This bulk technique permits the determination of the evolution of phases during heat treatment with a time resolution down to ~1 s [22].

The Ti–5Al–5Mo–5V–3Cr–1Zr (Ti-55531) metastable β titanium alloy corresponds to a variant of the analogous Ti–5Al–5Mo–5V–3Cr alloy which is based on the VT-22 alloy [5,11]. The development of Ti-55531 represents mechanical performance improvement and weight saving for parts previously made of Ti–10V–2Fe–3Al: the alloy offers higher strength levels by applying simplified processing paths [4,5]. The applications comprise aircraft components mainly located in the airframe and in the landing gear [5,6,11]. To the best knowledge of the authors just few works analysed heat treating of the Ti-55531 alloy [23,24], while no one evaluates the formation of α during heating of the β solution treated microstructure.

In the present work the phase transformation kinetics of the β-quenched Ti-55531 alloy is determined continuously as a function of the heating rate by means of in situ HEXRD. The investigations are complemented with metallographic analysis to evaluate the phase transformation mechanisms occurring at different heating stages. The evolution of phases is analysed in terms of volume fraction and the crystallographic relationships between their lattice structures during linear heating from room temperature (RT) to the β-field.

2. Experimental

2.1. Material

The composition of the investigated metastable β titanium alloy Ti–5Al–5Mo–5V–3Cr–1Zr (Ti-55531) is given in Table 1. The β-transus temperature, T_β, is 803 °C [24]. Samples of $20 \times 20 \times 20\ mm^3$ were cut from the as-received ingot and subjected to an isothermal heat treatment at 900 °C (β-field) for 20 min in dynamic argon 4.6 atmosphere and quenched in RT water. This water-quenched condition corresponds to the initial condition for the further investigations.

2.2. Microstructural characterization

Besides the initial condition, frozen microstructures of the Ti-55531 alloy were obtained by helium quenching of samples heated linearly at 5 K/min up to 400 and 550 °C, 20 K/min up to 650 °C, and 100 K/min up to 785 °C using the methodology explained elsewhere [25]. No holding time prior to helium quenching was applied upon reaching each temperature. Metallographic examinations of these microstructures were performed to be correlated with the transformation kinetics of phases revealed by in situ HEXRD and bring understanding in the mechanisms of phase transformation.

Specimens were prepared for light optical microscopy (LOM) and scanning electron microscopy (SEM) by grinding and polishing using a TegraPol machine. The samples for LOM were immersed for 20 s in a Kroll's reagent solution (2% HF + 4% HNO_3 + 94% H_2O) at RT to reveal the microstructural constituents. LOM was carried out using a Zeiss Axioplan optical microscope, while SEM using a FEI Quanta 200 field emission gun scanning electron microscope (FEG-SEM) operated in backscattered electron mode (BSE) at 20 kV. The grain size was determined by LOM using the ASTM standard E 1382-91 as implemented in the software Axio Vision 4.8.2.

Thin-foil specimens were prepared for transmission electron microscopy (TEM) by dimpling followed by ion milling using a Gatan precision ion polishing system (PIPS) device employed at 4 kV. The samples were examined with a Tecnai F20 microscope operated at 200 kV.

2.3. Study of phase transformation kinetics

In situ HEXRD was applied to determine the phase transformation kinetics of the Ti-55531 alloy. The evolution of phase volume fractions and lattice parameters was determined during continuous heating at 5, 20 and 100 K/min from RT up to 900 °C.

2.3.1. In situ high energy synchrotron X-ray diffraction

In situ HEXRD was carried out at the ID15B beamline of the ESRF (European Synchrotron Radiation Facility, Grenoble) [26]. The experimental parameters are summarized in Table 2. Samples of $4 \times 4 \times 20\ mm^3$ were heated up in a dynamic argon 4.6 atmosphere by means of a radiant furnace [14,21] and were kept fixed during acquisition. The temperature was controlled by a spot-welded thermocouple located next to the position of the incoming beam. Image sequences of complete Debye–Scherrer rings from the bulk of the samples were recorded in transmission mode (*thickness* = 4 mm) using an image-plate detector (see Table 2). Qualitative and quantitative analyses of the diffraction patterns were carried out as described elsewhere [21].

3. Results

3.1. Initial microstructure

Fig. 1(a) shows the initial microstructure of the Ti-55531 alloy. It presents a matrix of metastable β grains of approximately equiaxed morphology with a mean diameter of 100 ± 50 μm. Fig. 1(b) and (c) present TEM bright field images of two regions located in the interior of β grains. Fig. 1(b) shows dispersed dislocation lines along [2 0 0] β, probably generated during the quenching process. Fig. 1(c) shows a region in which periodic domains aligned across [2 0 0] β are associated with composition modulations of spinodal decomposition of β [18,27]. A nominal period of 11 ± 2 nm is obtained by considering the distance between peak intensities of domains (see inset in Fig. 1(c)). Analogous microstructures that reflect the spinodal decomposition mechanism for β were obtained upon quenching Cu–Ti alloys and after cooling a Ti–6Al–4V alloy produced by hot isostatic pressing

Table 1
Composition of the Ti–5Al–5Mo–5V–3Cr–1Zr alloy [24].

Element	Al	V	Mo	Cr	Zr	Fe	O	N	C	Ti	$[Mo]_{eq}$
wt.%	5.51	5.04	5.01	2.85	1.125	0.32	0.0655	0.0085	0.0045	Balance	~ 13

Table 2
Experimental parameters used during the in situ HEXRD experiments.

Beamline	Energy (keV)	Wavelength (nm)	Slit-aperture/spot size (μm^2)	Acquisition time (s)	Read-out time (s)	Detector
ID15B-ESRF	87	0.0142	300 × 300	2	1	Image Plate Pixium

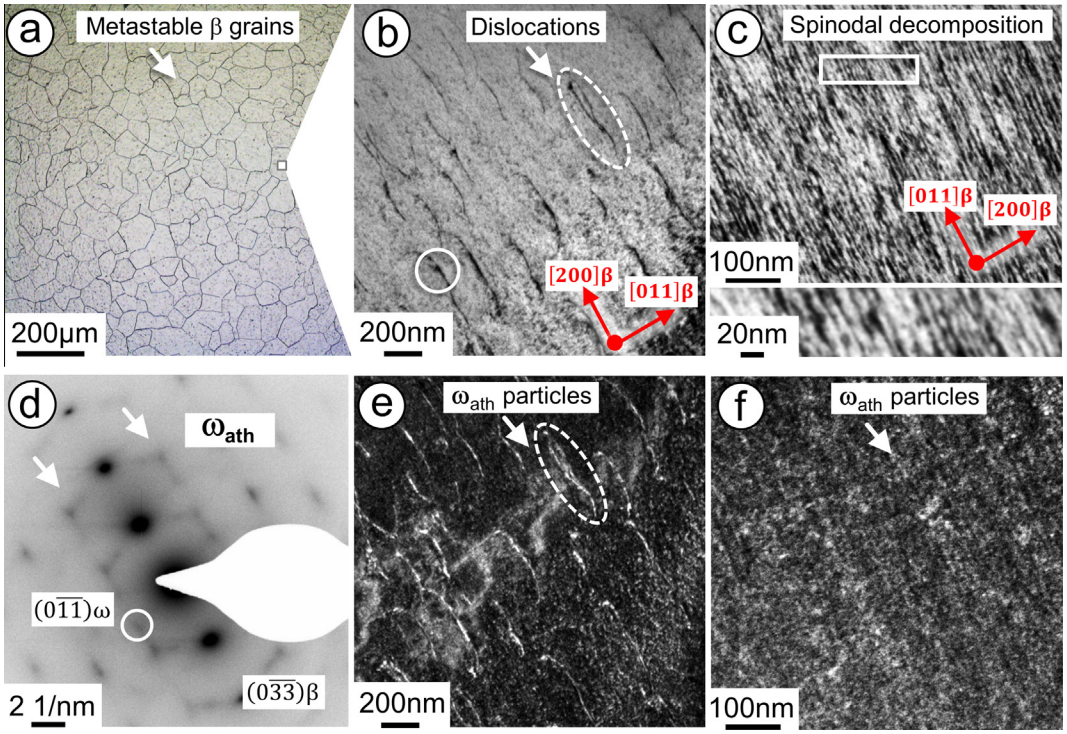

Fig. 1. (a) LOM image of the initial water-quenched microstructure of the Ti-55531 alloy formed by a matrix of metastable β grains of approximately equiaxed morphology. TEM bright field images: (b) dislocations dispersed in the matrix, (c) periodic aligned domains associated with spinodal decomposition of β. (d) Electron diffraction pattern of the $[0\bar{1}1]$ β zone axis from the encircled region in (b). (e), (f) TEM dark field images using $(0\bar{1}\bar{1})$ and $(1\bar{2}\bar{2})$ reflections of ω.

[28,29]. Fig. 1(d) shows the electron diffraction pattern obtained from the encircled region in Fig. 1(b). Here, the presence of the athermal ω phase (ω_{ath}) can be identified by relatively sharp spots (two of them are marked by arrows) that are partially connected by diffuse scattering between them [18,30]. A similar diffraction pattern was obtained for Fig. 1(c) (see Fig. 1 of supplementary material). Analogous electron diffraction patterns that denote the presence of ω_{ath} in titanium alloys were reported in previous studies [18,27,30–32]. Fig. 1(e) and (f) show the corresponding dark field images for Fig. 1(b) and (c) using the $(0\bar{1}\bar{1})$ and $(1\bar{2}\bar{2})$ reflections of ω, respectively. Fine ω_{ath} particles (~1–15 nm) can be observed decorating dislocation lines (Fig. 1(e)) as well as within domains of spinodal decomposition of β (Fig. 1(f)). Particle sizes of ω_{ath} between 2–10 nm have been reported for β-quenched metastable β alloys [33,34].

3.2. Influence of heating rate on phase transformations during continuous heating

Fig. 2(a) and (b) show quarters of characteristic diffraction patterns obtained by HEXRD that illustrate the evolution of Debye–Scherrer rings during continuous heating at 5 and 100 K/min, respectively. The sequence for 20 K/min is similar to 5 K/min and it is therefore not shown to improve legibility. The diffuse ring observed near the centre corresponds to the scattering of a quartz glass capsule used to keep the sample in inert gas atmosphere. At 25 °C, the spotty structure of the diffraction patterns reflects the relatively large grain size of the initial microstructure. At 475 °C, new Debye–Scherrer rings and straight streaks forming a cross-like shape [21] are observed for 5 K/min (see inset in Fig. 2(a)). Thereafter, this heating rate shows changes in the scattering angle of the Debye–Scherrer rings at 540 °C. At this

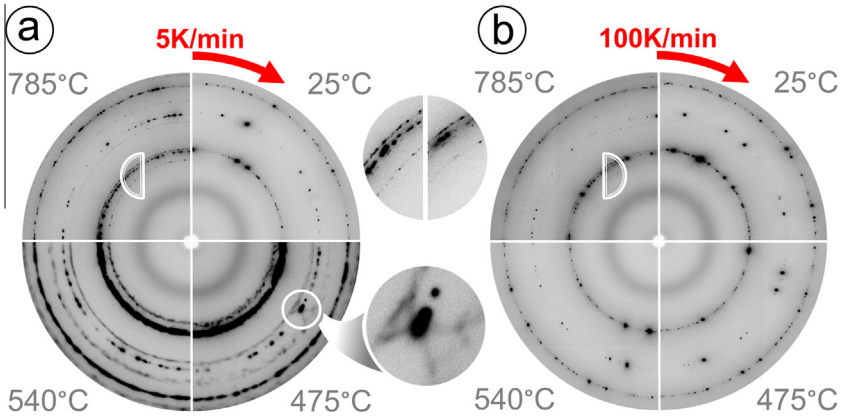

Fig. 2. Quarters of representative Debye–Scherrer rings obtained at 25, 475, 540 and 785 °C during continuous heating: (a) 5 K/min and (b) 100 K/min.

temperature, the sample heated with 100 K/min still shows the initial spotty structure. Finally, at 785 °C new weak reflections appear for both heating rates (see inset in Fig. 2).

Fig. 3(a) and (b) show the evolution of the integrated diffraction patterns as a function of temperature for a small 2-Theta range that represents qualitatively the complete HEXRD experiments for the 5 and 20 K/min heating rates, respectively. Due to the small 2-Theta range depicted, the ratio between peak intensities is not representative of the volume fraction of phases. The results for 100 K/min have been excluded to enhance readability and will be considered later. The data between RT–300 °C is omitted since no changes are observed in this temperature range. At ~300 °C the β phase is revealed without evidence of the ω_{ath} phase observed by TEM in the initial condition. This may be due to the overlapping of the highest intensity of the ω_{ath} reflections with the more extensive β-peaks, and the weak and broad ω_{ath} reflections resulting from the diffuse scattering of this phase associated with its lattice distortions [35]. The difficulty in identifying ω_{ath} in metastable β titanium alloys by X-ray diffraction has been reported by several authors (e.g. [11,21,36,37]). As the temperature increases, the intensity of the β reflection increases between ~350–400 °C and ~450–500 °C for 5 and 20 K/min, respectively. Thereafter, its decrease is accompanied by the emergence of low intensity α″ reflections between ~400–450 °C and ~500–550 °C for 5 and 20 K/min, respectively.

The fluctuations in the intensity of β are related to the presence of a thermally activated phase known as isothermal ω (referred to as ω in this work) (see e.g. [21,27,38]). This can be seen more clearly in Figs. 4 and 5, where colour-coded 2D plots corresponding to the evolution of several {hkl} reflections are presented for characteristic 2-Theta ranges during heating at 5 and 20 K/min, respectively. Reflections of ω lay next to the 2-Theta positions of β reflections. Fig. 4(b) shows that an isolated {002} ω refection becomes visible between ~350–400 °C for 5 K/min. Previous investigations reported the presence of ω between ~325–420 °C during heating of the analogous Ti–5Al–5Mo–5V–3Cr alloy [36,39]. Thereafter, α″ reflections become distinguishable between ~400–450 °C and ~500–550 °C during heating at 5 and 20 K/min, respectively. Furthermore, the {002} reflection of ω shifts to the position of {130} α″ slightly over 400 °C. The same effect was observed during continuous heating of a β-quenched Ti–10V–2Fe–3Al metastable β alloy [21]. As the temperature increases, α″ reflections move towards the position of α up to ~650 °C. No reflections associated with metastable phases such as ω or α″ can be observed during heating at 100 K/min (Fig. 6). In this case, the single β phase is revealed up to ~650 °C where α reflections appear.

The fact that the 2-Theta positions of β reflections {110} and {200} do not strictly coincide for each sample in the initial condition, i.e. slight variations <0.5° are observed (Figs. 4, 5 and 6), can

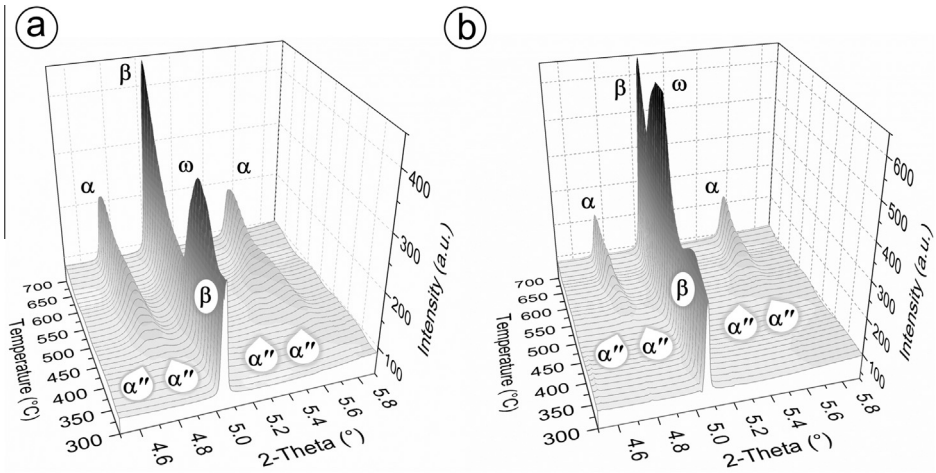

Fig. 3. Evolution of the diffraction patterns (limited to a small 2-Theta range) as a function of temperature during continuous heating: (a) 5 K/min and (b) 20 K/min.

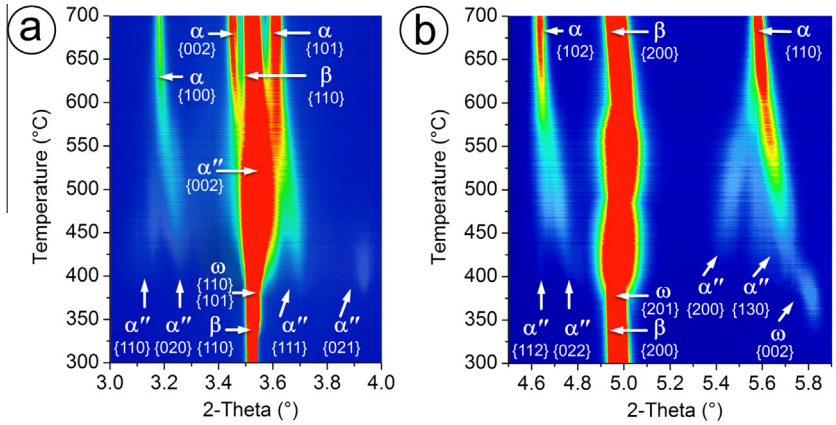

Fig. 4. Colour-coded 2D plots corresponding to the evolution of several {hkl} reflections during continuous heating at 5 K/min up to 700 °C for characteristic 2-Theta ranges: (a) 3–4° and (b) 4.5–5.9°.

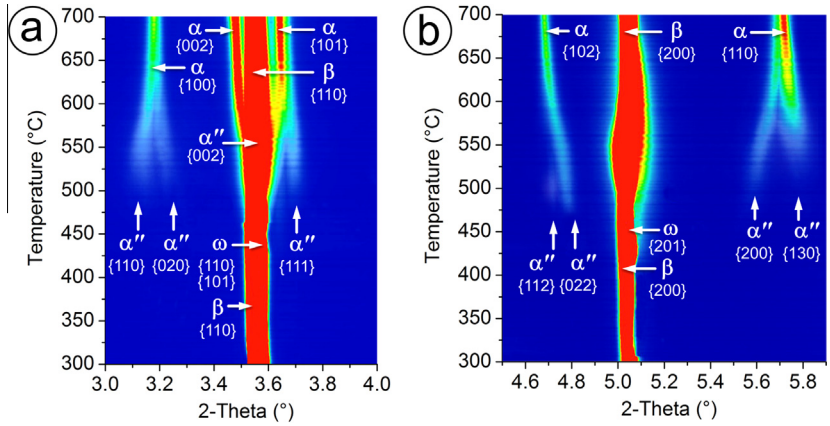

Fig. 5. Colour-coded 2D plots corresponding to the evolution of several {hkl} reflections during continuous heating at 20 K/min up to 700 °C for characteristic 2-Theta ranges: (a) 3–4° and (b) 4.5–5.9°.

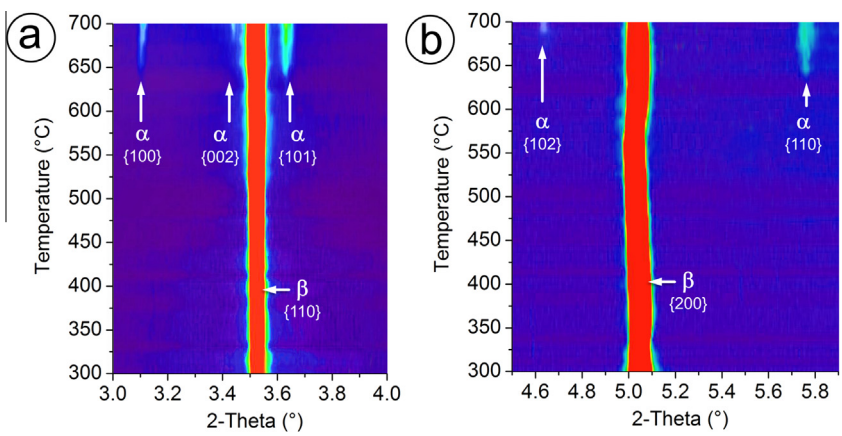

Fig. 6. Colour-coded 2D plots corresponding to the evolution of several {hkl} reflections during continuous heating at 100 K/min up to 700 °C for characteristic 2-Theta ranges: (a) 3–4° and (b) 4.5–5.9°.

be associated with variations in the average grain size of β. The relatively large scattering in the grain size distribution of the initial β-quenched microstructure (100 ± 50 μm) with respect to the investigated gauge volume contributes to the differences observed between samples in the initial condition. This also affects the width of β reflections and is reflected in the spotty structure of the Debye–Scherrer rings presented in Fig. 2. Moreover, slight 2-Theta variations may eventually occur due to an anisotropic retention of the metastable β phase produced by a non-uniform distribution of quenching strains between samples.

Fig. 7(a)–(c) show portions of the Debye–Scherrer rings converted into Cartesian coordinates at three characteristic temperatures for 5, 20 and 100 K/min, respectively. They represent a detail over a small azimuth range of the same {hkl} reflections presented in Figs. 4(b), 5(b) and 6(b) for 5, 20 and 100 K/min, respectively. At 25 °C, β is present in all conditions. At 400 °C and 5 K/min (Fig. 7(a)) {002} ω shifts towards the position of {130} α″ (see arrow). Clear α″ reflections become visible at 500 °C for 20 K/min (Fig. 7(b)). Moreover, diffuse streaking can be observed for both heating rates between the reflections {022} α″ and {200} α″ forming a cross with arms intersecting at the overlapping reflections {201} ω and {200} β. Then, at 450 and 550 °C the intensity of α″ reflections and the diffuse streaking increases for 5 and 20 K/min, respectively. Also, the reflections {112} α″–{022} α″ and {200} α″–{130} α″ become interconnected by diffuse streaking at these temperatures (Fig. 7(a) and (b)). Additional diffraction spots are visible for both conditions between {200} α″ and {130} α″ (indicated by circles). Fig. 7(c) shows that the α reflections {102} and {110} show up at 650 °C for 100 k/min. The evolutions presented in Fig. 7 can be visualized more clearly in the following video sequences included in the supplementary material: Fig7a.mp4, Fig7b.mp4 and Fig7c.mp4.

4. Discussion

The phase transformations observed by in situ high energy synchrotron X-ray diffraction were described qualitatively in the last section. Hereafter, these processes are studied by quantitative phase analysis using the Rietveld method as implemented in the software Maud ($R_w \leqslant 8\%$) [40]. This requires the knowledge of the crystallographic structure of the phases involved during the transformations, namely α, α″, ω and β, which are summarized in Table 3.

4.1. Formation of ω

Particles of ω_{ath} were observed by TEM decorating dislocation lines as well as within domains associated with spinodal decomposition of β in the initial water-quenched microstructure of the Ti-55531 alloy (Fig. 1). Thereafter, the presence of ω (isothermal ω) was detected during slow heating by in situ HEXRD: 5 and

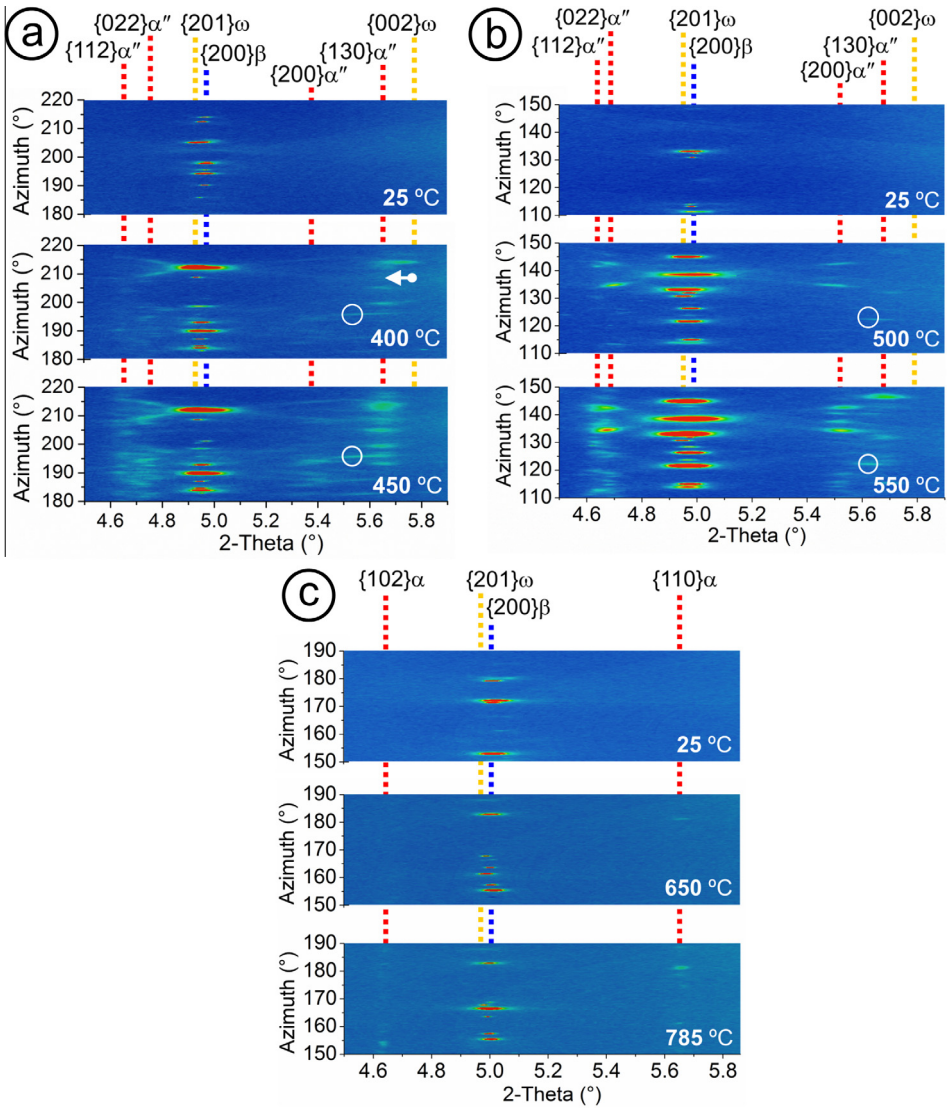

Fig. 7. Colour-coded 2D plots of selected portions of complete Debye–Scherrer rings converted into Cartesian coordinates. The evolution of the Bragg reflections is shown for three different temperatures: (a) 5 K/min, (b) 20 K/min and (c) 100 K/min.

Table 3
Crystallographic data from characteristic phases of Ti-based alloys identified in the HEXRD patterns and used for quantitative phase analysis.

Phase	Lattice system	Space group	Atomic positions	References
α″	Orthorhombic	*Cmcm*	(0, *y*, 1/4) (0, 1 − *y*, 3/4) (1/2, 1/2 + *y*, 1/4) (1/2, 1/2-*y*, 3/4) in this work *y* ~ 0.180 – 0.196	[76]
β	Cubic	$Im\bar{3}m$	(0, 0, 0) (1/2, 1/2, 1/2)	[18]
ω	Hexagonal	*P*6/*mmm*	(0, 0, 0) (1/3, 2/3, 1/3 + z_ω) (2/3, 1/3, 2/3- z_ω); z_ω = 1/6	[38]
α	Hexagonal	$P6_3/mmc$	(1/3, 2/3, 1/4) (2/3, 1/3, 3/4)	[18]

20 K/min present an intensity increase in the overlapping β/ω reflections between ~350–400 °C and ~450–500 °C (Fig. 3), respectively, while an isolated {002} reflection of ω emerges at the same time for 5 K/min (Fig. 4). This last effect is in agreement with the transformation mechanism of $\omega_{ath} \rightarrow \omega$. The formation of ω_{ath} particles occurs in solute lean regions of β due to the partial collapse of {111} β layers during fast cooling from the β-field [33]. Subsequent thermal treatment promotes the transformation of these ω_{ath} particles into ω by diffusion-driven rejection of alloying elements into β. This implies a complete collapse of the {111} β layers which leads to the formation of the {002} ω planes [27,33,41] observed in the present work for the 5 K/min condition (Fig. 4(b)). The fact that this transformation occurs to a larger extent as the heating rate decreases, points to the diffusive character of the transformation. This is also reflected in Fig. 8 where the evolution of phase volume fractions as a function of the temperature is presented for 5, 20 and 100 K/min. Fig. 8(a) and (b) show that ω reaches maximum volume fractions of ~25 and 10 vol.% at ~400 and 500 °C for 5 and 20 K/min, respectively.

Fig. 9(a) and (b) show TEM bright field images of the frozen microstructure of the Ti-55531 alloy obtained after heating at 5 K/min up to 400 °C. Arrays of dislocations (indicated by arrows)

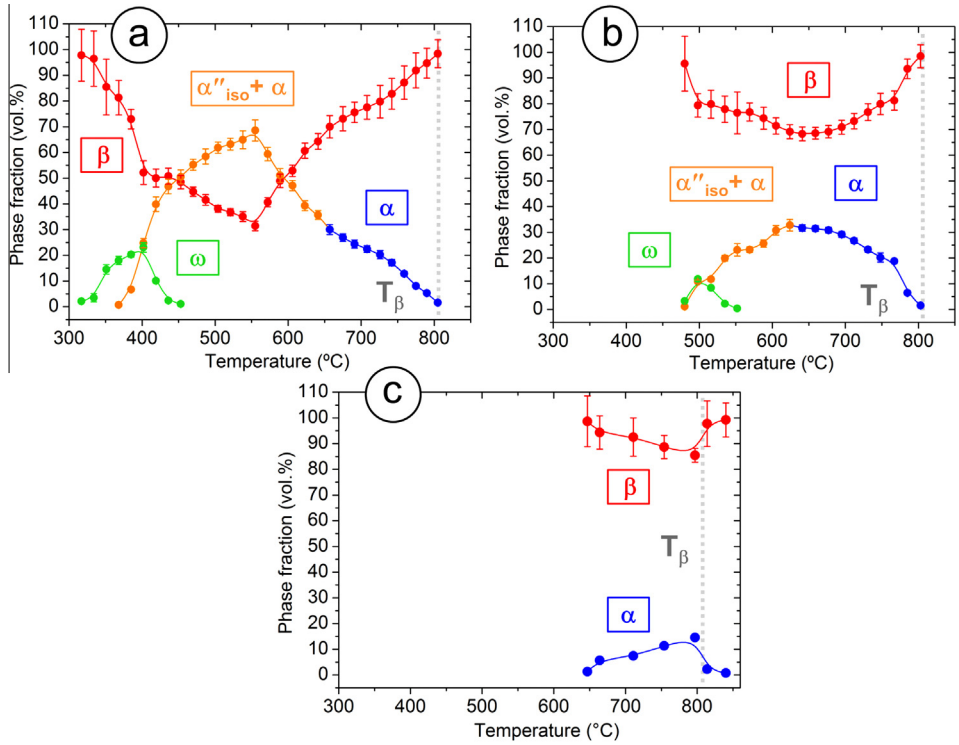

Fig. 8. Evolution of the phase volume fractions as a function of the temperature during continuous heating: (a) 5 K/min, (b) 20 K/min and (c) 100 K/min.

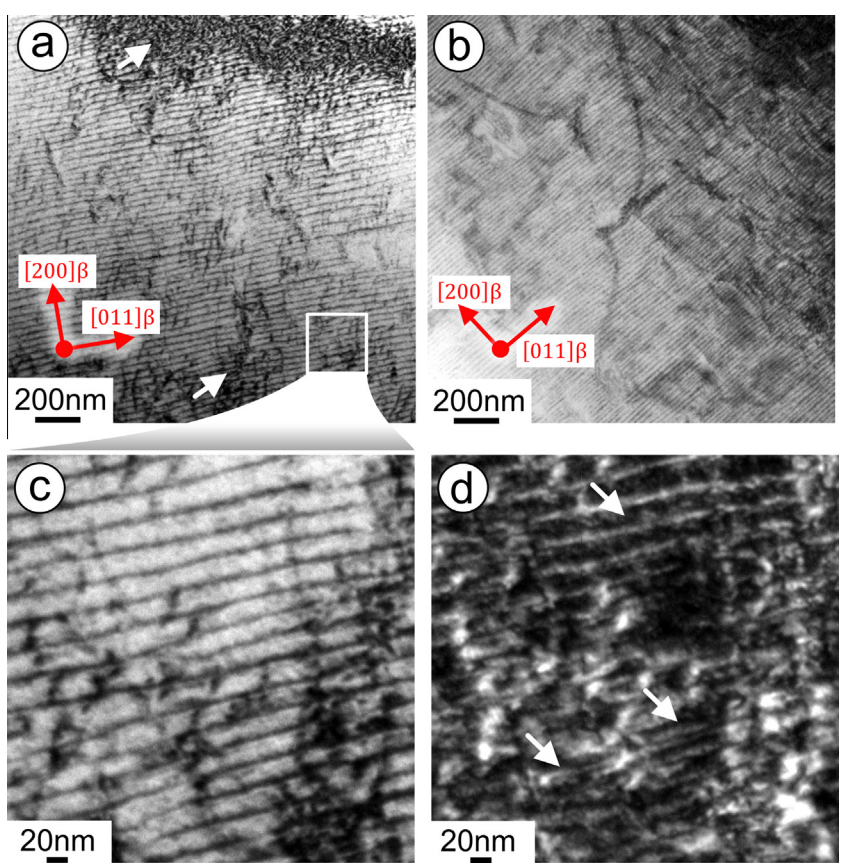

Fig. 9. TEM of the frozen microstructure of the Ti-55531 alloy heated with 5 K/min up to 400 °C. (a)–(b) Bright field images. (c) Detail of (a). (d) Dark field image of (c) using a $(\bar{1}00)$ reflection of ω.

can be observed within the β-matrix divided by a pattern of parallel domains across [200] β. This periodic contrast is associated with a spinodal decomposition of β, as mentioned for the initial microstructure (see Fig. 1 and Section 3.1) and addressed in Section 4.2.

Fig. 9(c) shows a detail of Fig. 9(a), while Fig. 9(d) shows the corresponding dark field image using the $(\bar{1}00)$ reflection of ω. Coarse (~20 nm) and finer (~1–5 nm) reflections of ω can be observed decorating dislocations and along the interfaces between domains associated with the spinodal decomposition of β (see arrows in Fig. 9(d)), respectively. Particle sizes between 10 and 100 nm have been reported for ω during isothermal ageing of metastable β titanium alloys [33,34,42]. The current results provide direct evidence of the influence of dislocations on the formation of ω after quenching (see Fig. 1 and Section 3.1) and during heating of the Ti-55531 alloy up to 400 °C (Fig. 9). The presence of ω_{ath} and ω particles along dislocations has been reported for Ti–24Nb–4Zr–7.6Sn and Ti–7.5Mn–0.5B alloys, respectively [32,43]. Furthermore, several studies have shown that the introduction of dislocations during the deformation of β-quenched microstructures containing ω_{ath} altered the regular formation of ω during subsequent ageing [44–47]. Also, a model that describes the formation of ω through a dislocation mechanism proposed for mechanically shocked tantalum [48,49] was used to explain the formation of ω_{ath} upon quenching of Ti–Nb and Ti–V alloys [50,51]. Since dislocations represent lattice distortions of the matrix, this could explain the lack of detection of ω_{ath} by means of in situ HEXRD [35].

4.2. Spinodal decomposition of β

Spinodal decomposition of the β matrix is observed for the initial water-quenched condition of the Ti-55531 alloy (Fig. 1) and after heating at 5 K/min up to 400 °C (Fig. 9). This effect leads to the formation of a composition-modulated structure across ⟨100⟩ β directions, which are elastically soft directions for bcc titanium and zirconium alloys [18,27]. In agreement with the present results, the spinodal decomposition mechanism was suggested to explain the homogeneous precipitation of fine α plates from the metastable β matrix of the analogous Ti–5Al–5Mo–5V–3Cr–0.5Fe, a Timetal 21S and Ti–V alloys [52–54]. These works state that the transformation is controlled by small compositional fluctuations in β, where lean and rich regions in solute evolve towards the equilibrium as the temperature increases. Similar observations were reported during spinodal decomposition of β in Ti–6Al–4V and Ti–35Nb–7Ta/7Zr–5Ta alloys [29,55,56]: two solid solutions, namely β′ and β that are poor and rich in β stabilizers, respectively, lead to domains of different compositions and lattice parameters. According to this, Figs. 1(c) and 9(a)–(c) show patterns of periodic and aligned domains of β′ and β across [200] β. This effect disappears at higher temperatures as revealed by microstructural observations performed with TEM (see Fig. 2 of supplementary material).

For the initial microstructure the spinodal decomposition of β is observed as discontinuous concentration fluctuations with a nominal period of 11 ± 2 nm (see Fig. 1(c) and its inset). However, after heating up to 400 °C with 5 K/min this effect presents continuous and symmetric periods of 26 ± 3 nm (Fig. 9(a)–(c)). A similar concentration wavelength (20 nm) was reported during spinodal decomposition of β in Zr–Al based alloys [18,27]. These differences indicate that further decomposition of β occurs during slow heating: element diffusion provokes the ordered arrangement of β′/β domains and their increase in amplitude, i.e. wavelength during transformation [28,57,58].

During spinodal decomposition the strain gradient generated at the interface between solute lean and solute rich regions can induce a high density of misfit dislocations [18,55,56]. This may explain the presence of dislocation arrays observed in Fig. 9 for the Ti-55531 alloy. Moreover, as the dislocation density increases, the transformation accelerates because atoms can easily diffuse through the stress field of dislocations during phase separation [59,60]. Thus, bigger particles can form near dislocation cores as observed for the Ti-55531 alloy (see Section 4.1 and Fig. 9(d)) and has been reported previously by simulations [60]. These aspects together with the observations presented in the current work (see Section 4.1, Figs. 1 and 9), suggest that spinodal decomposition of β contributes to the formation of ω [29]: the strains generated between β′ and β domains may induce the plane collapse required for the formation of ω_{ath}, and provide favourable sites for diffusion (such as dislocation cores and solute lean domains) that assist the ω_{ath} to ω transformation (see Section 4.1). The fact that fine layers of ω reflections are observed at both sides of the dark lines, i.e. the interfaces between domains (compare Fig. 9(c) and (d), and see arrows in Fig. 9(d)) supports this hypothesis. Since ω forms in solute depleted regions [30,33,41] and at the white areas of Fig. 9(d), these areas may represent the solute depleted domains of β′ for the Ti-55531 alloy.

Recent investigations with a TIMETAL LCB metastable β titanium alloy revealed that ω forms in the β matrix as an array of particles along ⟨100⟩ β directions [61], which coincide with those undergoing concentration modulations during spinodal decomposition. In agreement with this, it was reported in a previous study of a Ti–6Al–4V alloy that ω forms as parallel strings of particles during spinodal decomposition of β [29]. Furthermore, investigations with Zr–Al based alloys showed that cuboidal ω particles were formed between compositional fluctuations along ⟨100⟩ β during subsequent long-term ageing [18,27]. These findings together with the results presented in the current study support an influence of spinodal decomposition in the formation of ω as it was also suggested by other studies with titanium alloys [29,54,61].

4.3. Formation of α″

Figs. 4 and 5 show the emergence of reflections associated with α″ between ~400–450 °C and ~500–550 °C during heating at 5 and 20 K/min, respectively. The formation of this phase, usually termed α''_{iso} [21], has been reported at moderate temperatures (420–600 °C) during isothermal decomposition of the metastable β matrix of several alloys (Ti-17 [12], Ti-5553 [13], VT-22 and TIMETAL LCB [62] with $[Mo]_{eq}$ = ~9, 12, 11, 18 wt.% respectively).

Fig. 10(a) and (b) present the evolution of the lattice parameters as a function of the temperature for 5 and 20 K/min, respectively. A correspondence between the a_{ω} and $c_{\alpha''}$ parameters can be observed during the ranges ~400–450 °C and ~500–550 °C for 5 and 20 K/min, respectively. The same correlation was observed in previous works with a Ti–10V–2Fe–3Al alloy and commercially pure titanium [21,63,64]. This, together with the continuous shift of the {002} ω reflection to the position of {130} α″ observed slightly over 400 °C for 5 K/min (see Figs. 4(b), 7(a) and Fig7a.mp4), points to the formation of α''_{iso} from ω. The same transformation was suggested during continuous heating and ageing of the Ti–10V–2Fe–3Al and Ti–8Mo alloys, respectively [21,65].

Fig. 11(a) shows a TEM bright field image of the frozen microstructure of the Ti-55531 alloy after heating at 5 K/min up to 400 °C. It presents dislocation-like domains dispersed in the β matrix with a low angle grain boundary in the centre. Two processes occur at temperatures close to 400 °C: ω starts to dissolve while the volume fraction of α''_{iso} increases (Fig. 8(a)). Therefore, the fact that this region of the microstructure does not present any signs of ω, points to a more advanced transformation stage than the one observed in Fig. 9. The corresponding dark field image

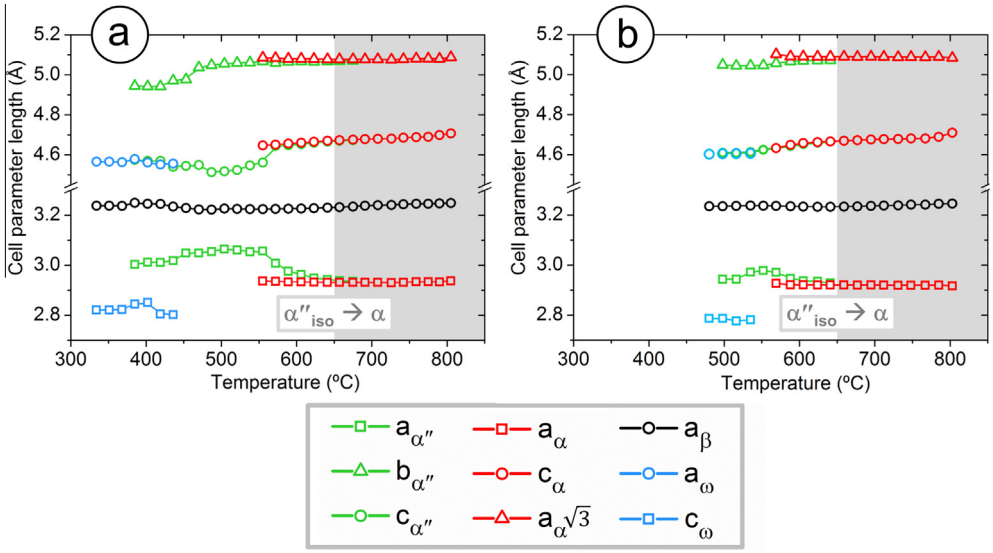

Fig. 10. Evolution of the lattice parameters and of crystallographic relationships between phases as a function of temperature during continuous heating: (a) 5 K/min and (b) 20 K/min.

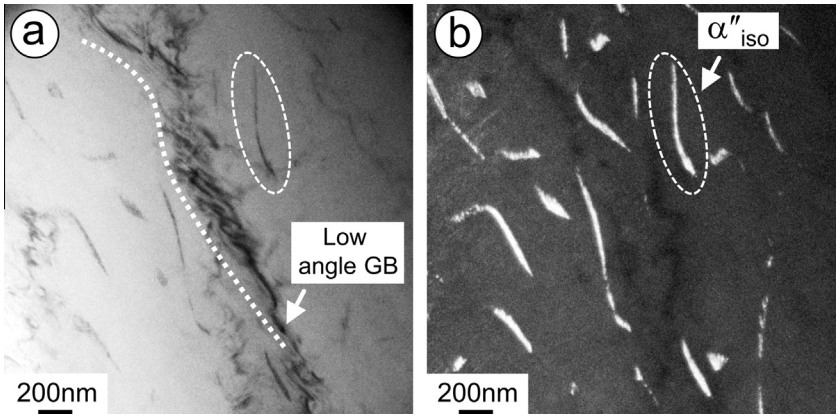

Fig. 11. TEM of the frozen microstructure of the Ti-55531 alloy heated with 5 K/min up to 400 °C. (a) Bright field image showing dislocation-like domains dispersed in the β matrix with a low angle β grain boundary in the centre. (b) Dark field image using a (1 1 2) reflection of α″.

(Fig. 11(b)) shows that the dislocation-like regions are highlighted by selecting the (1 1 2) reflection of α″. This, together with the correspondence between the reflections and lattice parameters of ω and α''_{iso} observed by in situ HEXRD suggests that α''_{iso} precipitates with the sequence *dislocation* (ω_{ath}) → ω → α''_{iso}.

Fig. 10(a) shows an increase of $b_{\alpha''}$ and $a_{\alpha''}$ between ~400–550 °C during heating at 5 K/min. A similar evolution of the lattice parameters is observed for 20 K/min between ~500–550 °C (Fig. 10(b)). In parallel to these variations, Rietveld analysis revealed an increase in the atomic *y*-coordinate of the crystal structure of α″ from 0.180 to 0.196 (see Table 3), denoting a continuous increase in the solute content of this phase [21,66]. These effects together with the fact that at this stage of the heating the volume fraction of α''_{iso} + α increases while that of β decreases (Fig. 8), suggest that growth of α''_{iso} occurs by the transfer of solute atoms from β to α''_{iso}. Thus, precipitation of α''_{iso} along former dislocation cores (see Fig. 11), i.e. ω phase (see Figs. 1 and 9), may take place by diffusion of solute elements [67]. These sites are favoured owing to distortion of the lattice, while the introduction of solute elements may eliminate the stress field and slip associated with dislocations [67,43]. This process tends to stabilize the β phase, and therefore, homogenize the domains resulting from spinodal decomposition. Experimental evidences of this precipitation mechanism have been reported for titanium and titanium based alloys [28,68–70].

The transformation mechanism of α''_{iso} is reflected in the diffuse scattering observed during the formation of this phase (see Figs. 2(a), 7(a) and (b) taken from the sequences Fig7a.mp4, Fig7b.mp4). This effect has been related to continuous distributions of lattice parameters [71,72] that, for the studied Ti-55531 alloy, may be induced by the strain modulations associated with dislocations and spinodal decomposition of β.

4.4. Formation of α

4.4.1. Formation from β

Reflections close to those expected for α are visible from ~400 and 500 °C during heating at 5 and 20 K/min, respectively (see circles in Fig. 7(a) and (b)). Accordingly, the presence of α has been reported at 400 °C during isothermal ageing of the analogous Ti–5Al–5Mo–5V–3Cr alloy [16,73,74].

Fig. 12(a)–(c) show BSE images of the frozen microstructure of the Ti-55531 alloy heated continuously with 5, 20 and 100 K/min up to 550, 650 and 785 °C, respectively. Complementary details

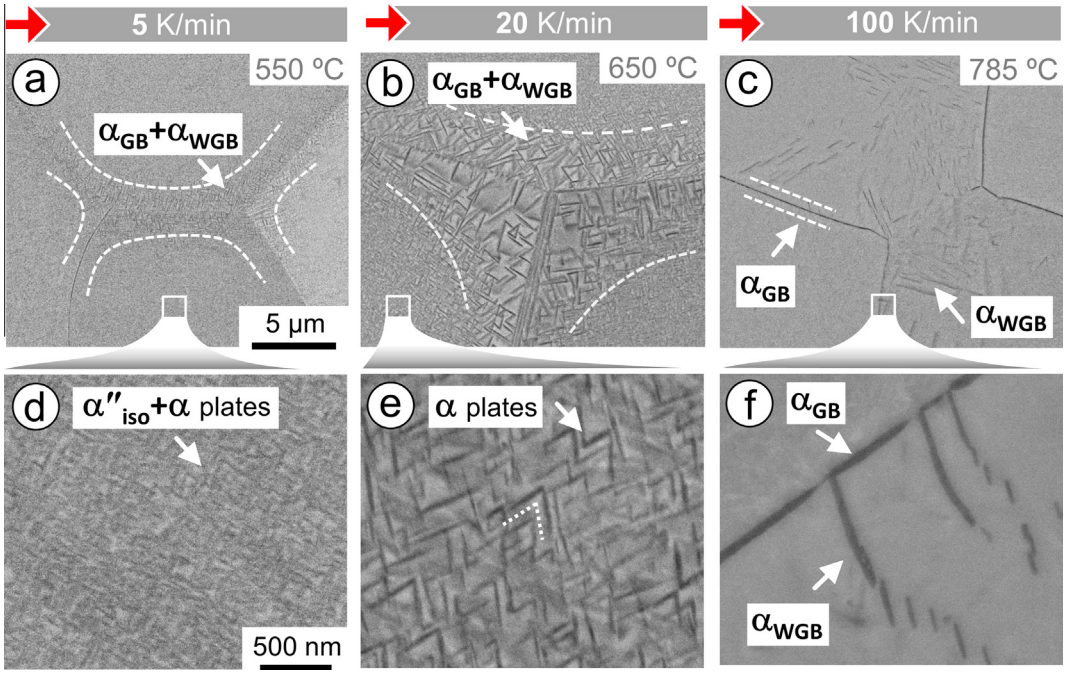

Fig. 12. BSE images of the frozen microstructures of the Ti-55531 alloy heated continuously with (a)–(d) 5 K/min (b)–(e) 20 K/min and (c)–(f) 100 K/min up to 550, 650 and 785 °C, respectively. (d)–(f) Show corresponding local microstructural details for these conditions.

of these frozen microstructures are shown in Fig. 12(d)–(f). According to Fig. 8 these temperatures correspond to the maximum volume fractions of $\alpha''_{iso} + \alpha$ and α for 5, 20 and 100 K/min, i.e. ~65, 30 and 15 vol.% respectively.

The transformation of α from β begins through the formation of α at the β grain boundaries (α_{GB}) and follows by the growth of Widmanstätten α colonies (α_{WGB}) from α_{GB}/β interfaces by depletion of β stabilizer elements (e.g. vanadium) [15,25,75]. The present results show that the direct formation of α via $\beta \rightarrow \alpha$ plays a more important role as the heating rate increases. This is the only transformation path for 100 K/min since the fast heating rate suppresses the formation of metastable phases (Fig. 6) and α forms exclusively as α_{GB} and α_{WGB} that can reach far into the β grains at $T > \sim 650$ °C (see Fig. 12(c) and (f)).

4.4.2. Formation from α''

Fig. 10(a) and (b) show a progressive evolution of $b_{\alpha''}$, $c_{\alpha''}$ and $a_{\alpha''}$ towards $a_\alpha\sqrt{3}$, c_α and a_α, respectively, until they coincide at temperatures above ~600–650 °C. Since the α hcp structure is obtained for $b/a = \sqrt{3}$ [21,76], this evolution indicates a gradual transformation of the orthorhombic α''_{iso} into α. Similarly, previous studies proposed a direct $\alpha'' \rightarrow \alpha$ transformation path during thermal treatment of the orthorhombic α'' martensite and α''_{iso} [21,77,78].

The higher concentration of β stabilizers in α''_{iso} with respect to α has been reported in previous investigations [62]. This suggests that, contrarily to the solute enrichment denoted during the formation of α''_{iso} (see Section 4.3), the $\alpha''_{iso} \rightarrow \alpha$ transformation is controlled by the transfer of β stabilizers from α''_{iso} to β. The compositional changes in α''_{iso} during this transformation may explain the non-equilibrium compositions presented by α at early precipitation stages of metastable β microstructures subjected to isothermal ageing (e.g. for the analogous Ti–5Al–5Mo–5V–3Cr–0.5Fe alloy) [17,52,54].

Fig. 12(d) and (e) show that the formation of α from α''_{iso} results in a fine and slightly coarser distribution of $\alpha''_{iso} + \alpha$ and α plates throughout the interior of β grains, for 5 and 20 K/min, respectively. Moreover, Fig. 12(e) clearly shows characteristic chevron-shaped α precipitates like the ones observed after ageing of the β solution treated microstructure of the analogous Ti–5Al–5Mo–5V–3Cr and Ti–5Al–5Mo–5V–3Cr–0.5Fe alloys [16,17,73].

Fig. 13(a) and (b) show the complete Debye–Scherrer rings converted into Cartesian coordinates obtained after heating at 5 and 100 K/min up to 650 and 785 °C, respectively. Fig. 13(a) shows that the {hkl} reflections of α and β are formed by an agglomeration of fine diffraction spots along their corresponding 2-Theta values. This reflects the homogeneous precipitation of α achieved via the $\alpha''_{iso} \rightarrow \alpha$ transformation path. Differently, Fig. 13(b) shows high intensity scarce spots of β with barely distinguishable α reflections that couple with the microstructure shown in Fig. 12(c) where a low volume fraction of α_{GB}/α_{WGB} is generated during the $\alpha \rightarrow \beta$ transformation.

4.5. Dissolution of α

Transformation of α into β starts at ~650 °C during heating at 5 and 20 K/min, while it shifts to ~785 °C during heating at 100 K/min (see Fig. 8). The process finishes at temperatures close to the equilibrium β-transus temperature (803 °C) [24].

5. Conclusions

The influence of phase transformation kinetics on the formation of α in the β-quenched Ti–5Al–5Mo–5V–3Cr–1Zr alloy has been studied by in situ high energy synchrotron X-ray diffraction and metallographic examinations as a function of heating rate. The following conclusions can be drawn from the investigations:

- Two different origins are identified for the formation of the ω phase in the β matrix: dislocations and β'/β domains resulting from spinodal decomposition of β. On the one hand, the strains associated with these sites induce the initial plane collapse required for the $\beta \rightarrow \omega_{ath}$ transformation observed for the initial condition of the alloy. On the other hand, the high diffusivity in

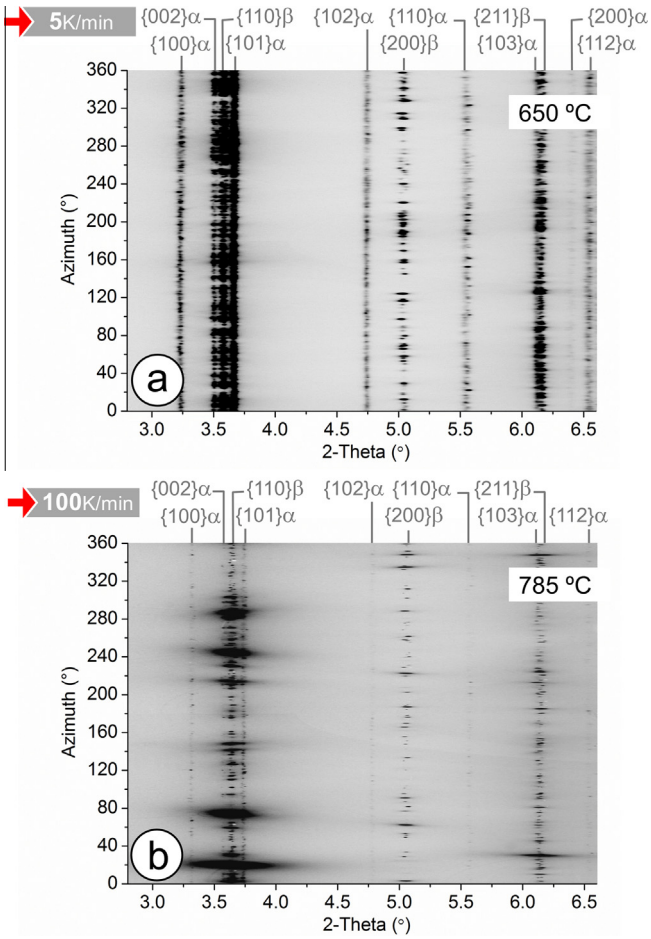

Fig. 13. Complete Debye–Scherrer rings converted into Cartesian coordinates for the heating experiments: (a) 5 K/min up to 650 °C, and (b) 100 K/min up to 785 °C.

these regions promotes the subsequent $\omega_{ath} \rightarrow \omega$ transformation observed by in situ HEXRD during slow heating up to ~350–500 °C.

- Spinodal decomposition of the metastable β matrix is observed for the initial water-quenched condition of the alloy and during subsequent slow heating up to 400 °C. Initially, this effect is characterized by an irregular distribution of discontinuous β′/β domains associated with composition fluctuations along [200] β. Thereafter, once diffusion is activated further decomposition results in a symmetric arrangement of continuous domains.
- Formation of the orthorhombic α''_{iso} phase from ω ($\omega \rightarrow \alpha''_{iso}$) is observed by in situ HEXRD during slow heating up to moderate temperatures (~400–550 °C). This phase precipitates in sites of former dislocations through the *dislocation* (ω_{ath}) → ω → α''_{iso} path and grows by the transfer of solute atoms from β to α''_{iso}.
- Formation of stable α phase occurs between ~600–650 °C through two different paths that lead to different distributions of this phase:

  a) The formation of α from β (β → α) begins by the growth of α at grain boundaries (α_{GB}) from where Widmanstätten α colonies (α_{WGB}) grow subsequently. The relevance of this transformation increases with the heating rate.
  b) Formation of α from α''_{iso} ($\alpha''_{iso} \rightarrow \alpha$) is revealed by the evolution of lattice parameters obtained by in situ HEXRD during slow heating. This transformation path leads to a homogenous formation of fine α plates within β grains.

Acknowledgements

The authors acknowledge the K-Project "Non-destructive testing and tomography Plus" supported by the COMET-Program of the Austrian Research Promotion Agency (FFG) and the provinces of Upper Austria (OÖ) and Styria (St).

The European Synchrotron Radiation Facility (ESRF) is acknowledged for the provision of synchrotron radiation facilities in the framework of the MA1268 proposal.

The University Service Centre for Transmission Electron Microscopy (USTEM) of the Vienna University of Technology (TU Wien) is acknowledged for the provision of TEM and FEG-SEM microscopes.

The authors would like to thank Prof. Peter Pongratz and Walid Hetaba from TU Wien for helpful discussions and collaboration during TEM experiments, respectively.

Appendix A. Supplementary data

Supplementary data associated with this article can be found, in the online version, at http://dx.doi.org/10.1016/j.actamat.2015.05.008.

References

[1] C. Leyens, M. Peters, Titanium and Titanium Alloys, first ed., Wiley-VCH, Weinheim, 2003.
[2] B.E. Hurless, F.H. Froes, Lowering the cost of titanium, Amptiac 6 (2002) 3–9.
[3] H. Clemens, S. Mayer, Design, processing, microstructure, properties, and applications of advanced intermetallic TiAl alloys, Adv. Eng. Mater. 15 (2013) 191–215.
[4] R.R. Boyer, R.D. Briggs, The use of β titanium alloys in the aerospace industry, J. Mater. Eng. Perform. 14 (2005) 681–685.
[5] S.L. Nyakana, J.C. Fanning, R.R. Boyer, Quick reference guide for β titanium alloys in the 00s, J. Mater. Eng. Perform. 14 (2005) 799–811.
[6] R.R. Boyer, Attributes, characteristics, and applications of titanium and its alloys, JOM 62 (2010) 21–24.
[7] A.K. Sachdev, K. Kulkarni, Z.Z. Fang, R. Yang, V. Girshov, Titanium for automotive applications: challenges and opportunities in materials and processing, JOM 64 (2012) 553–565.
[8] F.H. Froes, Current and emerging opportunities in titanium's expanding market, JOM 59 (2007) 27.
[9] Advisory Council for Aviation Research and Innovation in Europe, ACARE: Strategic research and innovation agenda, accessed 3 May 2015, <ftp://ftp.cordis.europa.eu/pub/technology-platforms/docs/sria-executive-summary.pdf>.
[10] G. Lütjering, J.C. Williams, Titanium, second ed., Springer, Berlin, 2007.
[11] N.G. Jones, R.J. Dashwood, M. Jackson, D. Dye, β phase decomposition in Ti–5Al–5Mo–5V–3Cr, Acta Mater. 57 (2009) 3830–3839.
[12] F. Bruneseaux, G. Geandier, E. Gautier, B. Appolaire, M. Dehmas, P. Boulet, In situ characterization of the transformation sequences of Ti17 alloy by high energy X-ray diffraction: influence of the thermal path, in: M. Niinomi, S. Akiyama, M. Hagiwara, M. Ikeda, K. Maruyama (Eds.), Ti-2007 Science and Technology, The Japan institute of metals, Sendai, 2007, pp. 563–566.
[13] A. Settefrati, E. Aeby-Gautier, B. Appolaire, M. Dehmas, G. Geandier, G. Khelifati, Low temperature transformation in the β-metastable Ti-5553 alloy, Mater. Sci. Forum 738–739 (2013) 97–102.
[14] E. Aeby, F. Gautier, J. Bruneseaux, B. Teixeira, G. Appolaire, S. Geandier Denis, Microstructural formation in Ti alloys: in-situ characterization of phase transformation kinetics, JOM 59 (2007) 54–58.
[15] M. Salib, J. Teixeira, L. Germain, E. Lamielle, N. Gey, E. Aeby-Gautier, Influence of transformation temperature on microtexture formation associated with α precipitation at β grain boundaries in a metastable titanium alloy, Acta Mater. 61 (2013) 3758–3768.
[16] A. Dehgan-Manshadi, R.J. Dippenaar, Development of α-phase morphologies during low temperature isothermal heat treatment of a Ti–5Al–5Mo–5V–3Cr alloy, Mater. Sci. Eng. A 528 (2011) 1833–1839.
[17] S. Nag, R. Banerjee, R. Srinivasan, J.Y. Hwang, M. Harper, H.L. Fraser, Ω-Assisted nucleation and growth of α precipitates in the Ti–5Al–5Mo–5V–3Cr–0.5Fe β titanium alloy, Acta Mater. 57 (2009) 2136–2147.
[18] S. Banerjee, P. Mukhopadhyay, Phase Transformations: Examples from Titanium and Zirconium Alloys, first ed., Elsevier, Oxford, 2007.
[19] R.R. Boyer, D.U. Furrer, The potential advantages of microstructure modeling of titanium to the aerospace industry, in: S. Ghosh, J.M. Castro, J.K. Lee (Eds.), Numiform 2004, AIP Conference proceedings, New York, 2004, pp. 1694–1699.
[20] M.G. Glavicic, D.U. Furrer, G. Shen, A Rolls-Royce corporation industrial perspective of titanium process modelling and optimization: current capabilities and future needs, J. Strain Anal. Eng. Des. 45 (2009) 329–335.

[21] P. Barriobero-Vila, G. Requena, F. Warchomicka, A. Stark, N. Schell, T. Buslaps, Phase transformation kinetics during continuous heating of a β-quenched Ti–10V–2Fe–3Al alloy, J. Mater. Sci. 50 (2015) 1412–1426.
[22] K.D. Liss, A. Bartels, A. Schreyer, H. Clemens, High-energy X-rays: a tool for advanced bulk investigations in material science and physics, Texture Microstruct. 35 (2003) 219–252.
[23] V.A. Bykov, T.V. Kulikova, L.B. Vedmid, A. Ya Fishman, K.Yu. Shunyaev, N.Tu. Tarenkova, Thermophysical properties of Ti–5Al–5V–5Mo–3Cr–1Zr titanium alloy, Phys. Met. Metallogr. 115 (2014) 705–709.
[24] M. Dikovits, C. Poletti, F. Warchomicka, Deformation mechanisms in the near-β titanium alloy Ti-55531, Metall. Mater. Trans. A 45 (2014) 1586–1596.
[25] P. Barriobero-Vila, G. Requena, T. Buslaps, M. Alfeld, U. Boesenberg, Role of element partitioning on the α–β phase transformation kinetics of a bi-modal Ti–6Al–6V–2Sn alloy during continuous heating, J. Alloy. Compd. 626 (2015) 330–339.
[26] ID15 – High Energy Scattering Beamline, ESRF, accessed 3 May 2015, <http://www.esrf.eu/UsersAndScience/Experiments/StructMaterials/ID15>.
[27] S. Banerjee, R. Tewari, G.K. Dey, Omega phase transformation morphologies and mechanisms, Int. J. Mater. Res. 97 (2006) 963–977.
[28] D.E. Laughlin, J.W. Cahn, Spinodal decomposition in age hardening copper–titanium alloys, Acta Metall. 23 (1975) 329–339.
[29] Z. Fan, A.P. Miodownik, TEM study of metastable β-phase decomposition in rapidly solidified Ti–6Al–4V alloy, J. Mater. Sci. 29 (1994) 6403–6412.
[30] J.C. Willams, D. Fontaine, N.E. Paton, The ω-phase as an example of an unusual shear transformation, Metall. Trans. 4 (1973) 2701–2708.
[31] S.L. Sass, The structure and decomposition of Zr and Ti B.C.C. solid solutions, J. Less-Common Met. 28 (1972) 157–173.
[32] S.J. Li, T.C. Cui, Y.L. Hao, R. Yang, Fatigue properties of a metastable β-type titanium alloy with reversible phase transformation, Acta Biomater. 4 (2008) 305–317.
[33] A. Devaraj, S. Nag, R. Srinivasan, R.E.A. Williams, S. Banerjee, R. Banerjee, H.L. Fraser, Experimental evidence of concurrent compositional and structural instabilities leading to ω precipitation in titanium-molybdenum alloys, Acta Mater. 60 (2012) 596–609.
[34] H.P. Ng, A. Devaraj, S. Nag, C.J. Bettles, M. Gibson, H.L. Fraser, B.C. Muddle, R. Banerjee, Phase separation and formation of omega phase in the beta matrix of a Ti–V–Cu alloy, Acta Mater. 59 (2011) 2981–2991.
[35] I.B. Ramsteiner, O. Shchyglo, M. Mezger, A. Udyansky, V. Bugaev, S. Schöder, H. Reichert, H. Dosch, Omega-like diffuse X-ray scattering in Ti–V caused by static lattice distortions, Acta Mater. 56 (2008) 1298–1305.
[36] A. Settefrati, M. Dehmas, G. Geandier, B. Denand, E. Aeby-Gautier, B. Appolaire, G. Khelifati, J. Delfosse, Precipitation sequences in beta metastable phase of Ti-5553 alloy during ageing, in: L. Zhou, H. Chang, Y. Lu, D. Xu (Eds.), Ti-2011, Science Press Beijing, Beijing, 2012, pp. 468–472.
[37] D. Qin, Y. Lu, K. Zhang, Q. Liu, L. Zhou, X-ray photoelectron spectroscopy characterization of the ω phase in water quenched Ti-5553 alloy, Mater. Charact. 73 (2012) 77–80.
[38] C.B. Basak, S. Neogy, D. Srivastava, G.K. Dey, S. Banerjee, Disordered bcc γ-phase to δ-phase transformation in Zr-rich U-Zr alloy, Philos. Mag. 91 (2011) 3290–3306.
[39] Q. Contrepois, M. Carton, J. Lacomte-Beckers, Characterization of the β phase decomposition in Ti–5Al–5Mo–5V–3Cr at slow heating rates, O. J. Metal. 1 (2011) 1–11.
[40] L. Lutterotti, S. Matthies, H.R. Wenk, A.J. Schultz, J. Richardson, Combined texture and structure analysis of deformed limestone from time-of-flight neutron diffraction spectra, J. Appl. Phys. 81 (1997) 594–600.
[41] B.S. Hickman, The formation of omega phase in titanium and zirconium alloys: a review, J. Mater. Sci. 4 (1969) 554–563.
[42] A. Devaraj, R.E.A. Williams, S. Nag, R. Srinivasan, H.L. Fraser, R. Banerjee, Three-dimensional morphology and composition of omega precipitates in a binary titanium–molybdenum alloy, Scr. Mater. 61 (2009) 701–704.
[43] Z. Fan, A.P. Miodownik, Microstructural evolution in rapidly solidified Ti–7.5 Mn–0.5 B alloy, Acta Mater. 44 (1996) 93–110.
[44] J. Coakley, V.A. Vorontsov, K.C. Littrell, R.K. Heenan, M. Ohnuma, N.G. Jones, D. Dye, Nanoprecipitation in a beta-titanium alloy, J. Alloy. Compd. 623 (2015) 146–156.
[45] Y. Fei, B. Tang, H. Kou, X. Wang, G. Shang, Z. Zhu, J. Li, L. Zhou, Phase transformation and microstructure evolution in hot rolled TB-13 alloy during continuous heating, in: L. Zhou, H. Chang, Y. Lu, D. Xu (Eds.), Ti-2011, Science Press Beijing, Beijing, 2012, pp. 552–555.
[46] S. Guo, Q. Meng, L. Hu, G. Liao, X. Zhao, H. Xu, Suppression of isothermal ω phase by dislocation tangle and grain boundaries in metastable β-type titanium alloys, J. Alloy Compd. 550 (2013) 35–38.
[47] S. Guo, B. Chen, Q. Meng, R. Zhao, X. Zhao, Peculiar aging response of near β Ti–25Nb–2Mo–4Sn alloy for biomedical applications, Prog. Nat. Sci. 23 (2013) 1–6.
[48] L.M. Hsiung, D.H. Lassila, Shock-induced deformation twinning and omega transformation in tantalum and tantalum-tungsten alloys, Acta Mater. 48 (2000) 4851–4865.
[49] L.L. Hsiung, Shock-induced phase transformation in tantalum, J. Phys. Condens. Matter 22 (2010) 1–6.
[50] A.A. Popov, A.G. Illarionov, S.V. Grib, O.A. Elkina, Formation conditions of omega phase in titanium alloys after quenching, in: L. Zhou, H. Chang, Y. Lu, D. Xu (Eds.), Ti-2011, Science Press Beijing, Beijing, 2012, pp. 694–697.
[51] A.G. Illarionov, A.A. Popov, S.V. Grib, A. Elkina, Special features of formation of omega-phase in titanium alloys due to hardening, Met. Sci. Heat Treat. 52 (2010) 493–498.
[52] S. Nag, Y. Zheng, R.E.A. Williams, A. Devaraj, A. Boyne, Y. Wang, P.C. Collins, G.B. Viswanathan, J.S. Tiley, B.C. Muddle, R. Banerjee, H.L. Fraser, Non-classical homogeneous precipitation mediated by compositional fluctuations in titanium alloys, Acta Mater. 60 (2012) 6247–6256.
[53] A. Boyne, D. Wang, R.P. Shi, Y. Zheng, A. Behera, S. Nag, J.S. Tiley, H.L. Fraser, R. Banerjee, Y. Wang, Pseudospinodal mechanism for fine α/β microstructures in β-Ti alloys, Acta Mater. 64 (2014) 188–197.
[54] M.K. Koul, J.F. Breddis, Phase transformations in beta isomorphous titanium alloys, Acta Metall. 18 (1970) 579–588.
[55] C.R.M. Afonso, P.L. Ferrandini, R. Caram, Hardening mechanism through phase separation of Beta Ti–35Nb–7Zr and Ti–35Nb–7Ta alloys, Mater. Res. Soc. Symp. Proc. 1487 (2012) 13–19.
[56] C.R.M. Afonso, P.L. Ferrandini, A.J. Ramirez, R. Caram, High resolution transmission electron microscopy study of the hardening mechanism through phase separation in a β-Ti–35Nb–7Zr–5Ta alloy for implant applications, Acta Biomater. 6 (2010) 1625–1629.
[57] M. Lambrigger, H.A. Calderon, G. Kostorz, Decomposition kinetics of Ni–11.8 at.%Ti at 853 K, Mater. Sci. Eng. A 158 (1992) 207–214.
[58] S. Sato, A. Hasegawa, S. Semboshi, K. Wagatsuma, Effect of dislocations on spinodal decomposition, precipitation, and age-hardening of Cu–Ti alloy, High Temp. Mater. Process 34 (2014) 123–130.
[59] F. Léonard, R.C. Desai, Spinodal decomposition and dislocation lines in thin films and bulk materials, Phys. Rev. B 58 (1998) 8277–8288.
[60] Y.S. Li, S.X. Li, T.Y. Zhang, Effect of dislocations on spinodal decomposition in Fe–Cr alloys, J. Nucl. Mater. 395 (2009) 120–130.
[61] J. Šmilauerová, P. Harcuba, J. Stráský, J. Stráská, M. Janeček, J. Pospíšil, R. Kužel, T. Brunátová, V. Holý, J. Ilavský, Ordered array of ω particles in β-Ti matrix studied by small-angle X-ray scattering, Acta Mater. 81 (2014) 71–82.
[62] O.M. Ivasishin, P.E. Markovsky, S.L. Semiatin, C.H. Ward, Aging of coarse- and fine-grained β titanium alloys, Mater. Sci. Eng. A 405 (2005) 296–305.
[63] Y. Akahama, H. Kawamura, T.L. Bihan, New δ (distorted-bcc) titanium to 220 GPa, Phys. Rev. Lett. 87 (2001) 275503.1–275503.4.
[64] Y.K. Vohra, P.T. Spencer, Novel gamma-phase of titanium metal at megabar pressures, Phys. Rev. Lett. 86 (2001) 3068–3071.
[65] Y. Mantani, Y. Takemoto, M. Hida, A. Sakakibara, M. Tajima, Phase transformation of a α″ martensite structure by aging in Ti–8 mass%Mo alloy, Mater. Trans. 45 (2004) 1629–1634.
[66] S. Banumathy, R.K. Mandal, A.K. Singh, Structure of orthorhombic martensitic phase in binary Ti–Nb alloys, J. Appl. Phys. 106 (2009) 093518.1–093518.6.
[67] D. Hull, D.J. Bacon, Introduction to Dislocations, fifth ed., Elsevier, Oxford, 2011.
[68] F. Appel, M. Oehring, R. Wagner, Novel design concepts for gamma-base titanium aluminide alloys, Intermetallics 8 (2000) 1283–1312.
[69] J. Zhang, L. Dong, Preferred precipitation of ordered α_2 phase at dislocations and boundaries in near-α titanium alloys, Mater. Sci. Eng. A 341 (2003) 229–235.
[70] A.V. Panin, M.S. Kazachenok, O.M. Kretova, O.B. Perevalova, Y.F. Ivanov, A.M. Lider, O.M. Stepanova, M.H. Kroening, The effect of electron beam treatment on hydrogen sorption ability of commercially pure titanium, Appl. Surf. Sci. 284 (2013) 750–756.
[71] K.D. Liss, A. Stark, A. Bartels, H. Clemens, T. Buslaps, D. Phelan, L.A. Yeoh, Directional atomic rearrangements during transformations between the α- and γ-phases in titanium aluminides, Adv. Eng. Mater. 10 (2008) 389–392.
[72] T.L. Cheng, F.D. Ma, J.E. Zhou, G. Jennings, Y. Ren, Y.M. Jin, Y.U. Wang, In situ three dimensional reciprocal-space mapping of diffuse scattering intensity distribution and data analysis for precursor phenomenon in shape-memory alloy, JOM 64 (2012) 167–173.
[73] N.G. Jones, R.J. Dashwood, M. Jackson, D. Dye, Development of chevron shape α precipitates in Ti–5Al–5Mo–5V–3Cr, Scr. Mater. 60 (2009) 571–573.
[74] D. Dye, F. Hu, N.G. Jones, Microstructure formation in alpha–beta titanium alloys, in: L. Zhou, H. Chang, Y. Lu, D. Xu (Eds.), Ti-2011, Science Press Beijing, Beijing, 2012, pp. 404–409.
[75] S. Malinov, W. Sha, Titanium Alloys: Modelling of Microstructure, Properties and Applications, Woodhead Publishing, Cambridge, 2009. pp. 203–236.
[76] E.G. Obbard, Y.L. Hao, R.J. Talling, S.J. Li, Y.W. Zhang, D. Dye, R. Yang, The effect of oxygen on α″ martensite and superelasticity in Ti–24Nb–4Zr–8Sn, Acta Mater. 59 (2011) 112–125.
[77] B. Tang, H.C. Kou, Y.H. Wang, Z.S. Zhu, F.S. Zhang, J.S. Li, Kinetics of orthorhombic martensite decomposition in TC21 alloy under isothermal conditions, J. Mater. Sci. 47 (2012) 521–529.
[78] T.W. Duerig, J. Albrecht, D. Richter, P. Fischer, Formation and reversion of stress induced martensite in Ti–10V–2Fe–3Al, Acta Metall. 30 (1982) 2161–2172.

Scientific Curriculum Vitae

Surname / First name	**Barriobero Vila, Pere**		
Address	Reindorfgasse 29, 1150 Vienna, Austria		
Telephone	Office: +43 (1) 58801 – 308 39	Private:	+43 680 3240923
E-mail	Office: pere.vila@tuwien.ac.at	Private:	pere.barriobero.vila@gmail.com
Place / Date of birth	Vic (Barcelona), 6th December 1985		

Nov. 2010 – Today 24th July 2015	**Graduate research assistant** Institute of Materials Science and Technology, Vienna University of Technology, Karlsplatz 13 / E308, 1040 Vienna, Austria
Sept. 2007 – Oct. 2010	**M.S. - Materials Science and Engineering** Polytechnic University of Catalonia (UPC), Barcelona
Mar. 2010 – Oct. 2010	Master's Thesis at the Vienna University of Technology within Erasmus programme
Sept. 2003 – June 2007	**B.S. - Mechanical Engineering** Autonomous University of Barcelona (UAB), Barcelona

Selected publications

P. Barriobero-Vila, G. Requena, F. Warchomicka, A. Stark, N.Schell, T. Buslaps
"Phase transformation kinetics during continuous heating of a β-quenched Ti-10V-2Fe-3Al alloy"
Journal of Materials Science (2015) Volume 50, Issue 3, pages 1412 – 1426
Robert W. Cahn Best Paper Prize 2015 *nomination*

P. Barriobero-Vila, G. Requena, T. Buslaps, M. Alfeld, U. Bösenberg
"Role of element partitioning on the α – β transformation kinetics of a bi-modal Ti-6Al-6V-2Sn alloy during continuous heating"
Journal of Alloys and Compounds (2015) Volume 626, pages 330 – 339

P. Barriobero-Vila, G. Requena, S. Schwarz, F. Warchomicka, T. Buslaps
"Influence of phase transformation kinetics on the formation of α in a β-quenched Ti-5Al-5Mo-5V-3Cr-1Zr alloy"
Acta Materialia (2015) Volume 95, pages 90 – 101

Selected talks

"Effect of element partitioning on the α – β phase transformation kinetics"
64th Annual conference on Applications of X-ray analysis, Denver, Colorado, United States of America
Awarded with the **Robert L. Snyder grant**

"Phase transformation kinetics of a metastable β titanium alloy"
Highlight Lecture in: LightMAT 2013 International Congress on Light Materials, Bremen, Germany

Languages

Catalan (mother tongue), German, English, Spanish